Doctoral Dissertation

Image Equations and Methodologies for Visualized Field Analysis

Hisashi Endo

Graduate School of Engineering,
Hosei Univerisity

March 2004

Acknowledgements

I would like to express my deepest gratitude to Professor Yoshifuru Saito, Hosei University, for directing this attractive research topic, providing satisfactory environment, and leading me to have a lot of valuable experiences. I am also thankful for his continuously warmhearted supports both in my public and my private life.

I greatly appreciate the technical advice as well as kindhearted personal care that I've been receiving from Professor Seiji Hayano, Hosei University. I also acknowledge his careful reading of this dissertation.

I gratefully acknowledge the stimulation and encouragement given by Professor Toshiyasu L. Kunii, Kanazawa Institute of Technology. I also acknowledge his careful reading of this dissertation and critical comments.

I would like to express my great gratitude to Professor Iliana Marinova, Technical University of Sofia in Bulgaria, for her warmhearted encouragement and help, both in my public and my private life. I also appreciate her comments and proofreading of this dissertation.

I am very grateful to Professor Hideo Saotome of Chiba University, Professor Tatsuya Doi of Ashikaga Institute of Technology, and Dr. Yoichi Midorikawa of Oita University for their discussion and lots of encouragement.

I am thankful to Professor Kiyoshi Horii, Shirayuri College, for his encouragement and giving me a lot of opportunities to know various fields in engineering. Sincere thanks are due to his staffs that I've collaborated as well. I appreciate the scientific information on wavelets, as well as visualization, and valuable discussion with Professor Hui Li of Yamagata University, Dr. Masahiro Takei of Nihon University, Ms. Chieko Kato of Oita Prefectural College of Arts and Culture, and Ms. Sawa Matsuyama of Computational Science Research Centre, Hosei University.

I also appreciate to be stimulated by Dr. Yoshikaza Ishii of NTT Advanced Technology Corporation to know how significant producing is in engineering. The technical supports in terms of computer programming and fruitful discussion with Mr. Yoshihiro Takasuka of International Institute of Universality are acknowledged.

I am very grateful to Dr. Chikara Kaido, Dr. Masahiro Fujikura, and Mr. Hisashi Mogi with Technical Development Bureau, Nippon Steel Corporation for their fruitful discussion and supporting my experiments in magnetism.

I am also very grateful to Dr. Shigeru Kanemoto, Mr. Katsumi Kubo, and Dr. Masatake Sakuma with Nuclear Engineering Laboratory, Toshiba Corporation for their fruitful discussion on image processing for visual testing and providing measurement devices.

I appreciate the encouragement, stimulations, and fruitful discussion received from the professors and colleagues concerned with the Japan Society of Applied Electromagnetics and Mechanics (JSAEM) as well as the technical society on magnetics with the Institute of Electrical Engineers of Japan (IEEJ).

I would like to convey my sincere thanks to Dr. Jun Zou of Qinghua University, Dr. Yaoqin Xie of Beijing University, Dr. Guoya Dong of Hebei University of Technology and Dr. Haiyan Tian of Chongqing University for their friendship and international collaboration.

I deeply appreciate the warmhearted encouragement of Professor Toshiyuki Takagi and the staffs concerning with his laboratory in Institute of Fluid Science, Tohoku University: Professor Tetsuya Uchimoto, Dr. Yun Luo, Officer Takeshi Sato, Secretary Noriko Suda, and so on. Moreover, I really appreciate the kindness and precious time with Professor Takagi's students. It is especially acknowledged that a lot of works in collaboration with Mr. Yoshiaki Nagaya was fruitful for me. Furthermore, I am very grateful to Dr. Haoyu Huang, International Institute of Universality, for useful conversation with him and inspiring me with his great experience and ideas in non-destructive evaluation.

The permanent friendship and kind supports of all present and former members of Professor Yoshifuru Saito's and Professor Seiji Hayano's laboratories in Hosei University are gratefully acknowledged.

Finally, I would like to express my great appreciation for the supports and comprehension of my invaluable family. I owe this study with success to them.

Graduate School of Engineering,
Hosei University

Hisashi ENDO

Abstract

This thesis formulates visualized field images by means of the classical field theory, and it is composed of two principal chapters.

The first describes theoretical background. A key idea of the formulation is that a pixel of a digital image is regarded as field potential in the classical physics. Scalar and vector potential fields represent monochrome and color images, respectively. Vector operations lead to governing equations of the images. Two types of image equations express any image: Poisson and Helmholtz types of partial differential equations are considered as governing equations of static and dynamic images, respectively. The image equations derive system of equations by discretizations using partial derivatives and fundamental solutions in electromagnetism. Solution strategies of the image equations are described. The image Poisson equation results in reproducing/arranging the static images from their own image source densities. The image Helmholtz equation generates the frames of dynamic images by means of equivalent characteristic values. Furthermore, modal analysis of the system of equations gives a novel idea for orthonormal transformation of the image data representation. It allows of multi-resolution analysis like that by wavelets.

The second presents several applications, taking up four kinds of field images visualized by video/CCD camera, magnetic sensor, scanning electron microscope (SEM), and infrared camera. At first, the image vector operations demonstrate sketch-like image generation and surface flaw classification. Second, the image Poisson equation is applied to visualized magnetic field data obtained by magnetic sensor in order to improve the spatial resolution. Third, the image Helmholtz equation makes it possible to visualize magnetic domain dynamics of a grain-oriented electrical steel through SEM observation. Finally, separation of the static and dynamic images from an infrared flow animation is accomplished by three-dimensional multi-resolution analysis utilizing the orthonormal transformation derived from the image equations.

Contents

List of Figures

List of Tables

CHAPTER 1

Introduction

1.1 Background

The evolution of hardware performing computation and visualization inspires this study to formulate *image*. Modern semiconductor technologies have given high speed and performance of personal computers (PC) with reasonable price. In the last decade, the hardware performance of PC has been jumped up: from 66 MHz to over 3 GHz in CPU speed; from 16 MByte to over 1 GByte in standard memory size [1, 2]. For development of the hardware, complicated phenomena in natural physics have been considered by means of the numerical solutions of integral and partial differential equations. This transfiguration enables us to analyze dynamics of three-dimensional vector fields although enormous memory installation and CPU resources are essentially required [3]. Thereby, computer-aided works are supporting the human-oriented manners to design products and predict their behaviors more efficiently [4].

On the other hand, the popularization of PC has stimulated to create a tremendous computer network community based on the *Internet*. The Internet enables us to send/receive/share binary coded data, characters, images, sounds, etc., bringing out a variety of the Web services. The advent of the downsized mobile tools as terminals like personal digital assistants (PDA) and mobile phones dramatically changes telecommunication scenes. Exchanging messages, photos, and movies is being done in daily life of anyone at anywhere. Computer network infrastructures spreading over the world provide environment which facilitates communicating directly and instantaneously among places with long distances as if it were borderless. The Internet has solutions to overcome *distance* as well as *time* in a quite efficient manner.

Whatever is performed, *image* is playing an important role in computer systems with graphical user interface (GUI). The numerical calculations of physical phenomena involves visualizing the results in order for us to grasp what is happened. The Web-based communication receives benefit from information given as photos and movies. Consequently, visualization and image handling techniques are invariably accompanied with modern computer usage.

Imaging on computer screens may be divided into two major categories. One is artificial illustration. The other is due to visualizing devices. The former one has been worked out by computer graphics (CG), for instance. CG has accomplished the frameworks to faithfully reflect objects and laid the foundations of *visualization* [5, 6]. Since CG makes it possible to reveal invisibles, then many simulation software packages employ CG techniques as their post-processing tools to display the simulated results with sophisticated illustrations [7, 8]. The latter one is carried out by cameras, microscopes, and so on. Various kinds of visualizing devices are available at the present time. For examples, X-ray, magnetic resonance imaging (MRI), etc., have been utilized in medical diagnosis as professional use. Digital video cameras employing charge-coupled device (CCD) come into wide use at relatively low cost. The visualizing devices are capable of imaging the physical phenomena according to their covering wavelengths, and then recording the images to PC as digitalized data. Needless to say, applying image processing techniques to the digitalized images assists us to clear up the visualized phenomena effectively. Moreover, the recent data storage technology gives environment to realize database systems constituting the digitalized images, expecting a kind of expert systems by computers.

On the assumption that the powerful computers and visualizing devices are available, the present study intends to develop the ultimate visualization methodologies that make it possible to extract the rules and laws from visualized physical systems. The rules and laws of the nature could be discovered by the knowledge, experiences, etc., of human wisdom, and finally they have been formulated, for example, with mathematical ways. This procedure is a typical inverse problem that finds the causes from effects. The visualizing devices also measure the effects/results due to the rules and laws of the nature. In order to extract them from data of the devices, the visualization methodologies should take the nature of physical system into account to derive the rules or laws. Thus, the present study investigates a model based on the classical field theory for visualization.

1.2 Strategy

The images obtained by the visualizing devices, so-called *visualized images*, are displayed as different types like static and dynamic (animation) images. In order to unify these various types of image in a most systematic manner, an approach based on the classical field theory is proposed.

The classical field theory is the most important counterpart establishing modern physics started with Newton mechanics, field problems such as theories of sound, light, and electromagnetism, resulting in solving for their field governing equations. It has exploited the vector and variational calculus, and led to modern quantum mechanics. The orthogonal functions representing the solution of the field equations have led to the systematic formulation of Hilbert space theory [9–11].

In much the same way as the formulation of modern physics, image processing, compressing, animating, etc., are carried out by means of the field theory. A key concept of the approach is that each of pixels representing digital images is regarded as a kind of potentials in vector fields. As is well known, the gradient of a scalar potential field yields a vector field. Further spatial derivative of the vector field, i.e., the divergence, translates the vector field into the scalar quantity called source density. Namely, the Laplacian operation of the scalar potential field gives the source density. In electromagnetism, this source density corresponds to electric charge density, while the scalar potential field corresponds to electric scalar potential field called voltage distribution. The voltage distribution can be exactly evaluated by solving for a partial differential (Poisson) equation having the electric charge density as an input electric field source [12, 13]. This nature is also held in case of the images. An original image can be generated from *image source density* which is derived from the Laplacian operation of the original image. Since the Laplacian operation is the second order partial derivatives with respect to the space, then the image source density conceals the constant and first differentiable terms of the original image. This means that the original image is compressed in terms of the image source density [14].

When the field theory is applied to an animating image, the image source density is simply assumed to be time-dependent data. However, animating targets on the image are not only artificial but also physical objects processed by the visualizing devices. In such cases, the animation must reflect the physical constraints. The approach based on the field theory is capable of expressing the physical movements. Instead of Poisson equation for the static images, Helmholtz type partial differential equations such as diffusion and wave equations becomes governing equations taking the initial conditions as well as medium parameters into account. For examples, the diffusion and

wave equations generate the spreading/shrinking and vibrating/repetitive animations, respectively. This is the same as those of the simulation technologies in computational engineering and physics [15, 16]. Therefore, the field theory unifies the animation and simulation technologies. Furthermore, discrete mathematical strategy to solve Poisson and Helmholtz equations yields system of equations. Modal analysis of the system of equations gives a general solution of the governing equations. In the other words, the expressible information on any images is represented in terms of the characteristic vectors based on Hilbert spatial theory.

When the field theory is applied to a color image, it reduces to solving for a vector Poisson or Helmholtz equation, while red, green, and blue (RGB) components, light's three primary colors, correspond to x-, y-, and z- components of a vector potential in Cartesian coordinate system, respectively. The governing equations in terms of RGB components can be solved independently under normal condition that computers treat the RGB components as independent data. And then synthesizing their solutions recovers the color image. Thus, the field theory processes the color images in much the same way as those of monochrome images.

To extract the rules and laws from the visualized images, an image model having commonly considerable ideas is essentially required. As abstracted above, images are represented by the systematic formulation of the classical field theory which is one of the succeeded approaches to generalize in the history of science. Numerical methods, such as finite difference, finite element, and discretized Green's function methods, implement practical differential and integral calculation for the scalar and vector potential fields representing the digital images with satisfactory high accuracy. Because of these strategies, the results of the extraction are referred by numerical values like images. Therefore, it is possible to work out the targets of the present study by using computers.

1.3 Outline

This thesis is composed of four chapters as follows: Chapter 1 introduces the present study and outlines this thesis; Chapter 2 gives the theoretical background; Chapter 3 shows several applications; and Chapter 4 concludes this thesis.

Chapter 2 consists of four sections, describing theoretical background to propose an image modeling for the visualized targets.

- Section 2.1 introduces *image vector operations* for the images in order to derive *image equations*. A key concept is that a pixel of a digital image is treated as a field potential. Scalar and vector potential fields represent monochrome and color images, respectively. Image vector operations, i.e., the gradient, divergence, and rotation, are introduced to derive the governing equations for the images. Poisson and Helmholtz types of partial differential equations are considered as the image equations of static and dynamic images, respectively. The image equations derive the system of equations from discretizations based on partial derivative and fundamental solutions in electromagnetism.

- Section 2.2 demonstrates strategies to solve the governing equation of static images, i.e., *image Poisson equation*. Finite differences, finite elements, and Green's function schemes are investigated. How to deal with the boundary conditions is also discussed. The image Poisson equation results in reproducing/arranging the static images from their own image source densities.

- Section 2.3 describes the governing equations for dynamic images. *Image Helmholtz equation* generates animation frames at arbitrary time by means of *equivalent characteristic values*. A series of frame images derives a set of the equivalent characteristic values from a general solution of the image Helmholtz equation, yielding the parameters representing dynamics of visualized systems.

- Section 2.4 proposes *modal-wavelet transform* as a novel orthonormal transformation for image data representation. Modal analysis of the discretized image governing equations leads to orthonormal bases that allow of multi-resolution analysis like that by the conventional discrete wavelets. It reveals that the bases are free from the problems on subject data length because of the modeling based on differential as well as integral forms of equations.

- Section 2.5 summarizes the chapter.

Chapter 3 demonstrates several applications of the approaches, consisting of five sections.

- Section 3.1 shows a couple of applications employing image vector operations. One is to generate sketch-like images. Calculating vector norm distribution of the image vectors derived by the gradient or rotation presents sketch-like images. The other is to classify shapes of surface flaws on the welded parts of structures. Orientation of the image vectors classifies into the line and circle types of flaws.

- Section 3.2 gives an application of the image Poisson equation for magnetic field imaging. A color image represents a magnetic vector field measured by magnetic sensor. The x-, y-, and z- components of the measured magnetic field are projected onto the red, green, and blue components of the color image, respectively. Solving a set of the image Poisson equations refines the spatial resolution of magnetic field.

- Section 3.3 deals with magnetic domain dynamics of a grain oriented electrical steel. A series of the magnetic domain images obtained by scanning electron microcopy (SEM) is applied the image Helmholtz equation to visualize iron loss distribution. Global and local magnetization curves, moreover the arbitrary condition of domain images can be generated from the solutions of image Helmholtz equation. It is described that the equivalent characteristic values obtained from a series of distinct SEM domain images are related to the parameters or functions of the conventional magnetization models.

- Section 3.4 demonstrates an application of the modal-wavelet transform. Three-dimensional multi-resolution analysis separates an infrared flow animation into the static and dynamic parts of the infrared animations. Comparison with the conventional wavelets is carried out.

Chapter 4 summaries the results given in each of the chapters and describes conclusions of the present dissertation.

CHAPTER 2

Image Modeling by the Classical Field Theory

2.1 Image Vector Operators

2.1.1 Concepts

In order to apply the classical field theory to develop an unified approach to the images, a pixel is assumed to be a kind of potentials to derive *image equations*. All images in digital computers are rectangular boxes filled with the discretized quantities in numerical values as square blocks. They are classified into monochrome and color images.

A monochrome image is assumed to be a two-dimensional array composing the numerical values like in Fig.2.1. In other words, a pixel of the monochrome image has one numerical value like an element in matrix of Fig.2.1(b) representing local brightness on computer screens. This leads that the monochrome image can be regarded as a two-dimensional scalar potential field U:

$$U = f(x, y), \tag{2.1}$$

where x and y denote positions in the horizontal and vertical directions on the field, respectively. The range of the pixel values treated in computers corresponds to the number of brightness levels depending on hardware. In order to satisfy the generality of approach, the normalized range, i.e., the range is in real number from 0 to 1 as shown in Fig.2.1(a), is considered in this study.

On the other hand, a color image consists of red, green, and blue (RGB) color components, i.e., light's three primary colors, as shown in Fig.2.2.

Namely, a set of three two-dimensional arrays, as in Fig.2.2(b), displays the color image. In other words, a pixel of the color image consists of three numerical values. This leads that the color image can be regarded as a vector potential field $\mathbf{A}$:

$$\mathbf{A} = A_R\mathbf{i} + A_G\mathbf{j} + A_B\mathbf{k}, \tag{2.2}$$

where A_R, A_G, and A_B represent the red, green, and blue components of color image, respectively. Moreover, $\mathbf{i}$, $\mathbf{j}$, and $\mathbf{k}$ denote the unit direction vectors corresponding to the x-, y-, and z- axes, respectively. Fig.2.2(c) illustrates the vector potential representation of Fig.2.2(a). In this case, the magnitude of a vector corresponds to brightness of the pixel, while it corresponds to the field intensity in physics. Each of the RGB components partly covers the same wavelength domain as that of the other components, however, computers treat them as independent data. Namely, the color image can be handled as a set of three monochrome images independently. Thus, the color image modeling by means of the field theory is essentially reduced into the similar operations to that of monochrome images.

The field theory started with potential representation yields vector operations, i.e., the gradient, divergence, and rotation. The gradient of a scalar field yields vector field $\mathbf{E}$. The divergence can be applied to vector field. Apply the divergence operation to the vector field $\mathbf{E}$, then the scalar quantity called source density is obtained. Moreover, the rotation can be applied to a vector field, curing around the orthogonal directions of the vector field. These vector operators carry out spatial derivatives in order to derive differential equations, as well as integral equations [17].

Since the plane of an image is filled with square blocks as pixels illustrated in Fig.2.3, then numerical approximation such as finite differences and finite elements works out the spatial derivatives. In order to denote the specific pixel on a monochrome image at the position (x, y), the following notation is employed:

$$U = f(x, y) \rightarrow U_{i,j}, \tag{2.3}$$

where the subscripts i and j refer to the positions on the image with respect to the horizontal (x-) and vertical (y-) directions, respectively. The distances between the pixels in terms of the x- and y- directions are assumed to be the same length, therefore, the subscripts i and j in Eq.(2.3) refer in positive integers. The notation for a color pixel is also carried out in much the same way as that for a monochrome pixel:

$$\mathbf{A}_{i,j} = A_{Ri,j}\mathbf{i} + A_{Gi,j}\mathbf{j} + A_{Bi,j}\mathbf{k}. \tag{2.4}$$

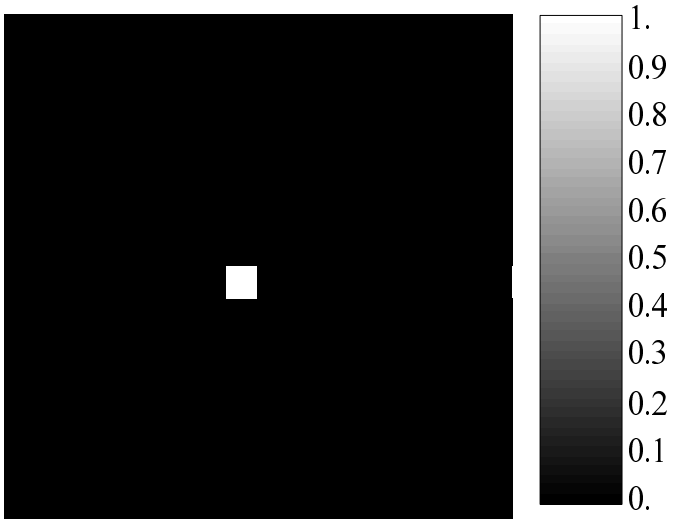

(a) A monochrome image

$$\begin{pmatrix}
0. & 0. & 0. & 0. & 0. & 0. & 0. & 0. & 0. & 0. & 0. & 0. & 0. & 0. & 0. & 0. \\
0. & 0. & 0. & 0. & 0. & 0. & 0. & 0. & 0. & 0. & 0. & 0. & 0. & 0. & 0. & 0. \\
0. & 0. & 0. & 0. & 0. & 0. & 0. & 0. & 0. & 0. & 0. & 0. & 0. & 0. & 0. & 0. \\
0. & 0. & 0. & 0. & 0. & 0. & 0. & 0. & 0. & 0. & 0. & 0. & 0. & 0. & 0. & 0. \\
0. & 0. & 0. & 0. & 0. & 0. & 0. & 0. & 0. & 0. & 0. & 0. & 0. & 0. & 0. & 0. \\
0. & 0. & 0. & 0. & 0. & 0. & 0. & 0. & 0. & 0. & 0. & 0. & 0. & 0. & 0. & 0. \\
0. & 0. & 0. & 0. & 0. & 0. & 0. & 0. & 0. & 0. & 0. & 0. & 0. & 0. & 0. & 0. \\
0. & 0. & 0. & 0. & 0. & 0. & 0. & 1. & 0. & 0. & 0. & 0. & 0. & 0. & 0. & 0. \\
0. & 0. & 0. & 0. & 0. & 0. & 0. & 0. & 0. & 0. & 0. & 0. & 0. & 0. & 0. & 0. \\
0. & 0. & 0. & 0. & 0. & 0. & 0. & 0. & 0. & 0. & 0. & 0. & 0. & 0. & 0. & 0. \\
0. & 0. & 0. & 0. & 0. & 0. & 0. & 0. & 0. & 0. & 0. & 0. & 0. & 0. & 0. & 0. \\
0. & 0. & 0. & 0. & 0. & 0. & 0. & 0. & 0. & 0. & 0. & 0. & 0. & 0. & 0. & 0. \\
0. & 0. & 0. & 0. & 0. & 0. & 0. & 0. & 0. & 0. & 0. & 0. & 0. & 0. & 0. & 0. \\
0. & 0. & 0. & 0. & 0. & 0. & 0. & 0. & 0. & 0. & 0. & 0. & 0. & 0. & 0. & 0. \\
0. & 0. & 0. & 0. & 0. & 0. & 0. & 0. & 0. & 0. & 0. & 0. & 0. & 0. & 0. & 0. \\
0. & 0. & 0. & 0. & 0. & 0. & 0. & 0. & 0. & 0. & 0. & 0. & 0. & 0. & 0. & 0.
\end{pmatrix}$$

(b) Scalar potentials represented by a matrix

Fig. 2.1. Monochrome image as a scalar field (16×16 pixels).

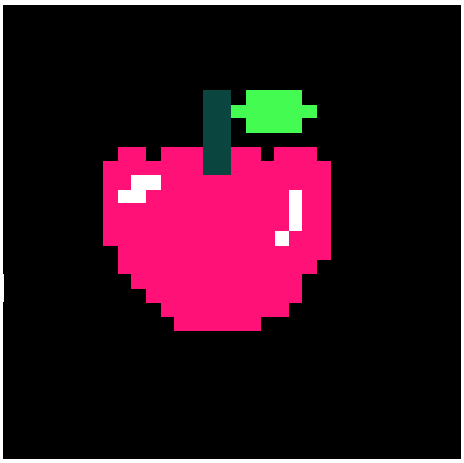

(a) A color image

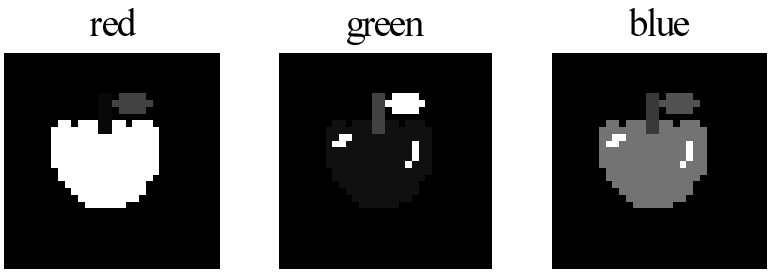

(b) Red, green, and blue components

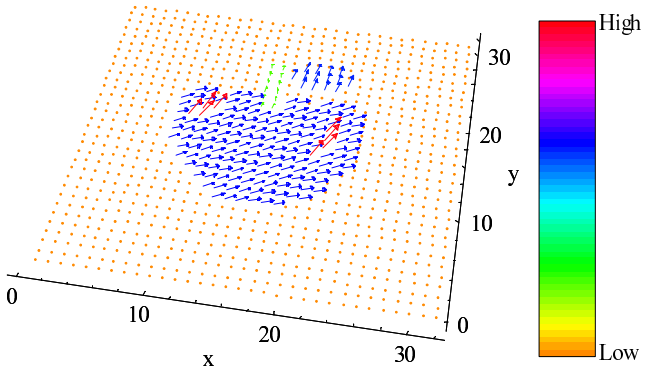

(c) Vector potential representation

Fig. 2.2. Color image as a vector field (32 × 32 pixels).

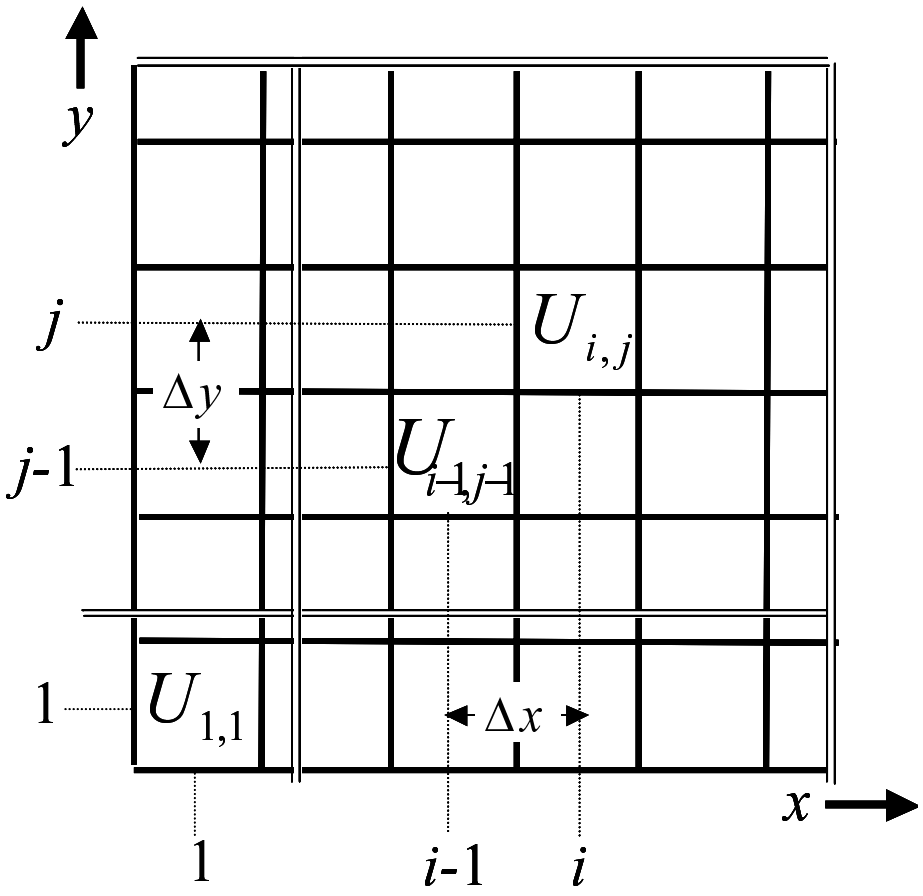

Fig. 2.3. Pixel value arrangement in a digital image.

2.1.2 Image Gradient Operator

Let a monochrome image to be a scalar field U, which is a function giving a scalar value to each point in two-dimensional space. The gradient operation,

$$\begin{aligned} \mathbf{E} &= -\nabla U, \\ &= -\left(\frac{\partial}{\partial x}\mathbf{i} + \frac{\partial}{\partial y}\mathbf{j}\right) U, \end{aligned} \tag{2.5}$$

provides an indication of how rapidly the scalar field changes in each of the directions, where $\mathbf{i}$ and $\mathbf{j}$ denote unit directional vectors with respect to the x- and y- directions, respectively. The symbol ∇ is a differential operator combining the partial derivatives in terms of the variables in space. As mentioned in Section 2.1.1, the images in digital computers are discretized. Numerical approximation of Eq.(2.5) is considered. As illustrated in Fig.2.3, the distances in directions of the x- and y- axes, i.e., Δx and Δy, are supposed to be the same value. Furthermore, assume Δx and Δy to be unit length, then the vector $\mathbf{E}_{i,j}$ based on Eq.(2.5) is approximated by the following central finite difference method [18, 19]:

$$\begin{aligned} \nabla U_{i,j} &\simeq \frac{U_{i+1,j} - U_{i-1,j}}{2\Delta x}\mathbf{i} + \frac{U_{i,j+1} - U_{i,j-1}}{2\Delta y}\mathbf{j}, \\ &\simeq \frac{U_{i+1,j} - U_{i-1,j}}{2}\mathbf{i} + \frac{U_{i,j+1} - U_{i,j-1}}{2}\mathbf{j}. \end{aligned} \tag{2.6}$$

When the differentiation is carried out to the boundary value problems, the boundary condition should be imposed. Here, the zero Dirichlet boundary condition is supposed at the edges of the images. Section 2.2 describes how to deal with the boundary values in detail.

Figures 2.4 and 2.5 illustrate the results of gradient in case of a dot and a line, respectively. In Figs. 2.4(b) and 2.5(b), the gradient fields are shown as the arrows indicating their magnitudes and directions, and the zero vectors are shown as the dots. In Fig.2.4, it is easy to find that four arrows diverge from the origin of the pixel having large in value. Fig.2.5 also has the same nature as that in Fig.2.4 and it follows the superposition principle. The gradient of a scalar field in physics fundamentally gives the arrows in entire region. However, the gradient shown here gives some zero vectors because the central finite difference scheme in Eq.(2.6) employs four pixels to determine the targeting vector. In order to carry out the gradient operation more precisely, the larger area around a pixel should be taken into account by the higher order approximation, fundamental solutions, etc [20].

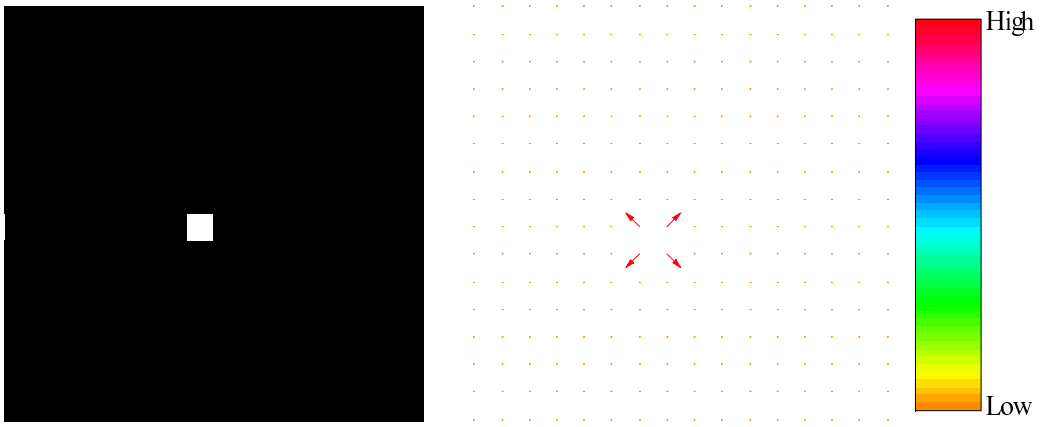

(a) A dot (b) Gradient vectors

Fig. 2.4. Gradient field of a dot (16 × 16 pixels).

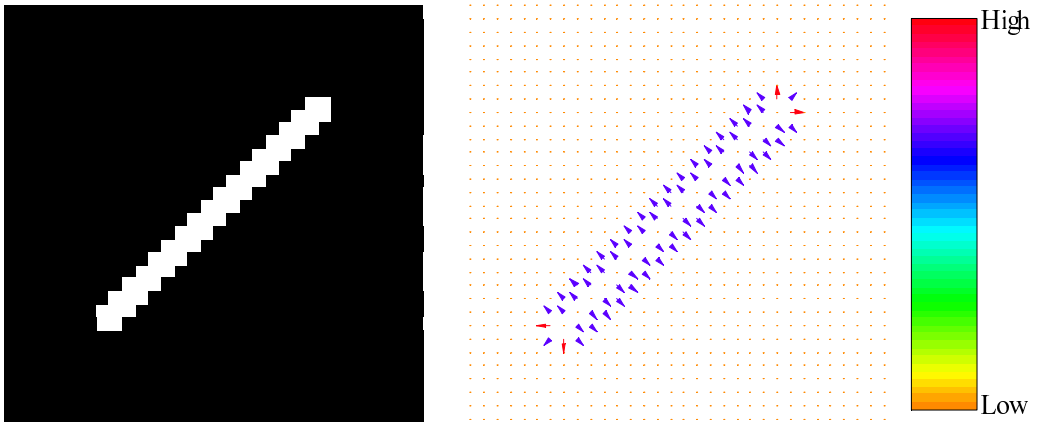

(a) A line (b) Gradient vectors

Fig. 2.5. Gradient field of a line (32 × 32 pixels).

2.1.3 Image Divergent Operator

The divergence is a differential operator for a vector field, giving a scalar field. The value of the divergence at a particular point evaluates the tendency of a vector field to point toward the point. The divergence of a gradient field $\mathbf{E}$,

$$\begin{aligned} \nabla \bullet \mathbf{E} &= \nabla \bullet (-\nabla U), \\ &= \left(\frac{\partial}{\partial x}\mathbf{i} + \frac{\partial}{\partial y}\mathbf{j}\right) \bullet \left(-\frac{\partial U}{\partial x}\mathbf{i} - \frac{\partial U}{\partial y}\mathbf{j}\right), \end{aligned} \tag{2.7}$$

translates another kind of scalar field so called source density distribution. The practical divergence at the pixel $U_{i,j}$ is also carried out by the same manner described in Section 2.1.2:

$$\begin{aligned} \nabla \bullet \nabla U_{i,j} &\simeq \frac{1}{2\Delta x}\left(\frac{U_{i+1,j} - U_{i,j}}{2\Delta x} - \frac{U_{i,j} - U_{i-1,j}}{2\Delta x}\right) \\ &\quad + \frac{1}{2\Delta y}\left(\frac{U_{i,j+1} - U_{i,j}}{2\Delta y} - \frac{U_{i,j} - U_{i,j-1}}{2\Delta y}\right), \\ &= \frac{1}{4}\left(\frac{U_{i+1,j} - 2U_{i,j} + U_{i-1,j}}{\Delta x^2} + \frac{U_{i,j+1} - 2U_{i,j} + U_{i,j-1}}{\Delta y^2}\right). \end{aligned} \tag{2.8}$$

Let the distances Δx and Δy in Eq.(2.8) to be unit length, then Fig.2.6 is obtained from the gradient fields of Figs. 2.4(b) and 2.5(b). In the practical calculation of the divergence, the values of the result become both positive and negative. If a negative value is assigned to a pixel, then the normalization of the pixel values shows the figures in this thesis. These distributions are so-called source density which yields a scalar potential field.

It is typically found in electrostatic field that the electric charge density makes the voltage distribution. This relation can be described by partial differential equation, as well as fundamental solutions with Green's functions. According to Coulomb's law, which is the representative fundamental solution in electric field, the gradient field $\mathbf{E}$ is given by,

$$\mathbf{E} \propto \frac{\sigma}{|\mathbf{r}|^3}\mathbf{r}, \tag{2.9}$$

where σ and $\mathbf{r}$ denote the source density and position vector to the source point toward the reference points, respectively. Fig.2.7 shows the gradient fields based on Coulomb's law with source densities in Fig.2.6. However, the source densities derived from the central finite difference approximation affects the accuracy of the gradient fields where the original scalar fields change rapidly. Thus, the image modeling by the field theory essentially requires higher order approximation of the spatial derivatives for precise operations.

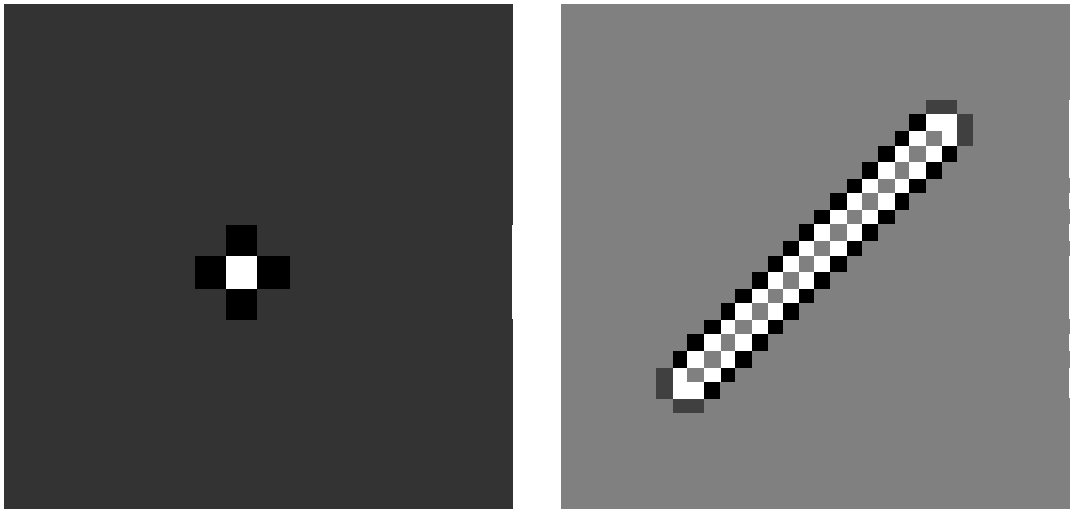

(a) Divergence of Fig.2.4(b) (16×16 pixels) (b) Divergence of Fig.2.5(b) (32×32 pixels)

Fig. 2.6. Divergence of the gradient fields.

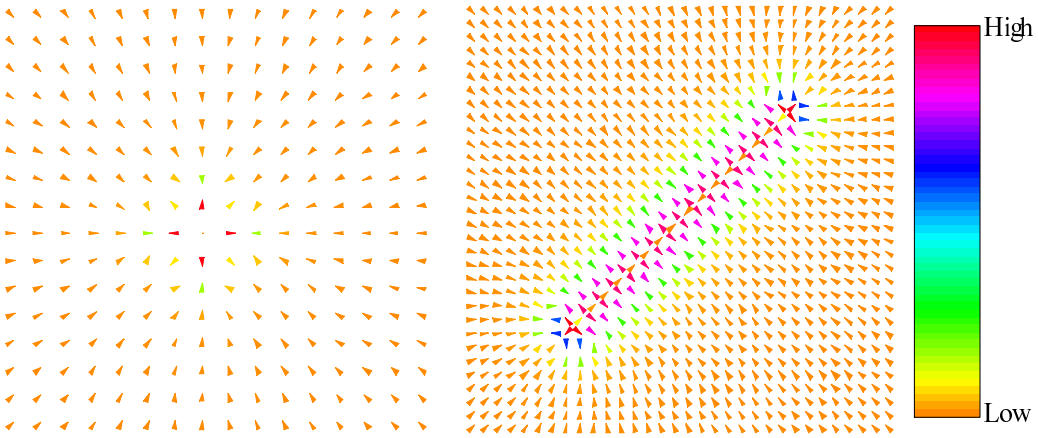

(a) Calculated from Fig.2.6(a) (b) Calculated from Fig.2.6(b)

Fig. 2.7. Gradient fields based on Coulomb's law.

2.1.4 Image Laplacian Operator

As described in Sections 2.1.2 and 2.1.3, the divergence of the vector field given by the gradient of a scalar field becomes a scalar field again. This process is referred to the Laplacian:

$$\begin{aligned} \nabla \bullet (\nabla U) &= \nabla^2 U, \\ &= \frac{\partial^2 U}{\partial x^2} + \frac{\partial^2 U}{\partial y^2}. \end{aligned} \tag{2.10}$$

The practical Laplacian in a digital image can be carried out by the central finite difference method. Let the distances between the pixels, Δx and Δy, to be unit length, then the Laplacian derived from five pixel values is,

$$\begin{aligned} \nabla^2 U_{i,j} &\simeq \frac{1}{4}\left(\frac{U_{i+1,j} - 2U_{i,j} + U_{i-1,j}}{\Delta x^2} + \frac{U_{i,j+1} - 2U_{i,j} + U_{i,j-1}}{\Delta y^2}\right), \\ &\simeq \frac{1}{4}\left(U_{i+1,j} + U_{i-1,j} + U_{i,j+1} + U_{i,j-1} - 4U_{i,j}\right). \end{aligned} \tag{2.11}$$

This is the same result as Eq.(2.8). There are some discretization methods to numerically approximate Eq.(2.10) [21]. In case of image processing based on the field theory, numerical approximation of the spatial derivatives happends to require higher accuracy using only the target pixel and its surrounding ones. A nine-point finite difference formula in Eq.(2.12) is possible to meet the request when the distances between the pixels, $\Delta x = \Delta y = \Delta$, are assumed to be unit length, viz.,

$$\begin{aligned} \nabla^2 U_{i,j} &\simeq \frac{1}{6\Delta^2}(U_{i-1,j-1} + 4U_{i-1,j} + U_{i-1,j+1} + 4U_{i,j-1} \\ &\quad +4U_{i,j+1} + U_{i+1,j-1} + 4U_{i+1,j} + U_{i+1,j+1} - 20U_{i,j}), \\ &\simeq \frac{1}{6}(U_{i-1,j-1} + 4U_{i-1,j} + U_{i-1,j+1} + 4U_{i,j-1} \\ &\quad +4U_{i,j+1} + U_{i+1,j-1} + 4U_{i+1,j} + U_{i+1,j+1} - 20U_{i,j}). \end{aligned} \tag{2.12}$$

Figs. 2.8 and 2.9 show the source densities obtained by means of Eqs. (2.11) and (2.12), respectively. The zero Dirichlet boundary conditions are set to the edges of the images.

The Laplacian is one of the popular techniques to extract the edges of target objects in image processing [22]. In this image modeling, the differentiation of the images leads to the governing equations that constitute the major frame part of this thesis.

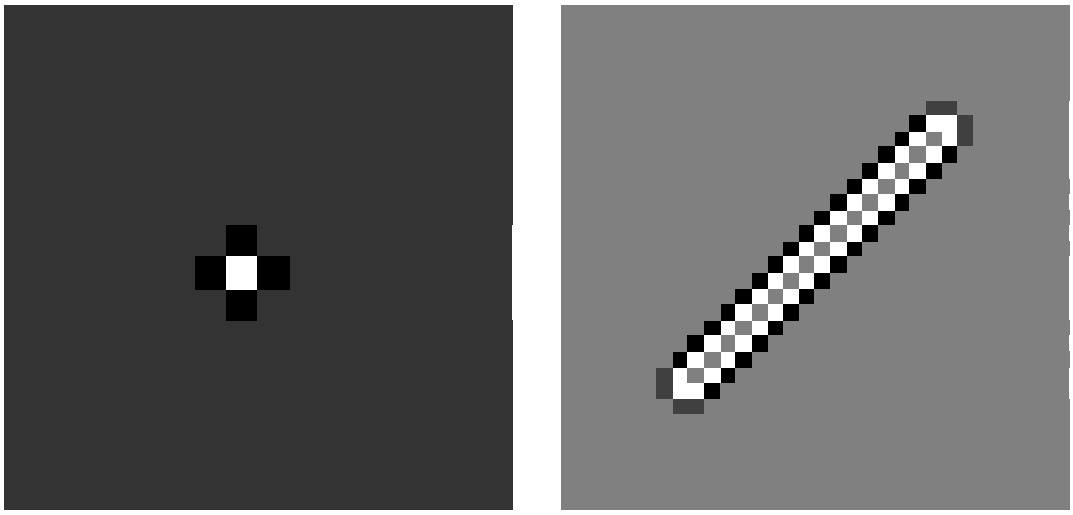

(a) Eq.(2.11) to Fig.2.4(a) (16×16 pixels) (b) Eq.(2.11) of Fig.2.5(a) (32×32 pixels)

Fig. 2.8. Laplacian of the monochrome images by means of Eq.(2.11).

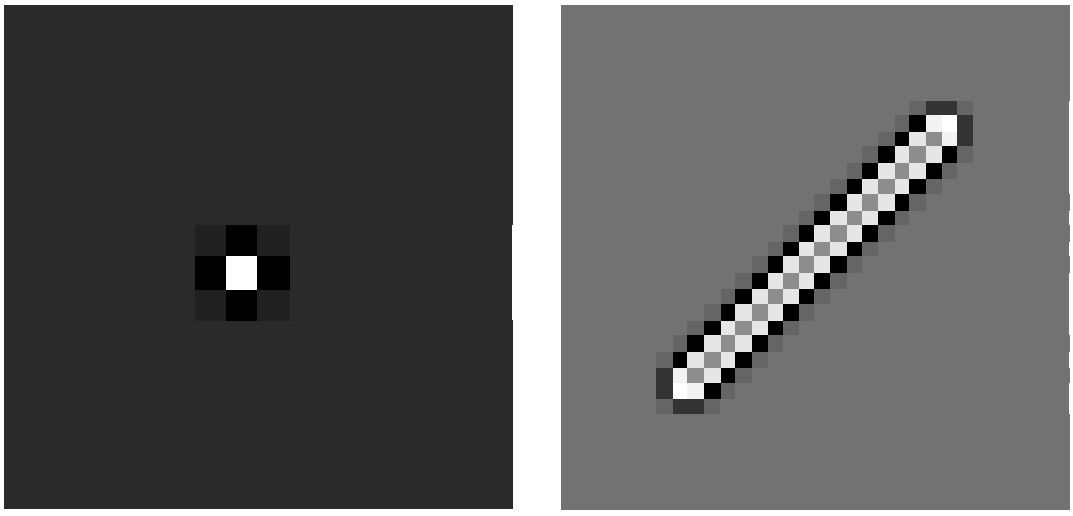

(a) A dot (16×16 pixels) (b) Eq.(2.12) of Fig.2.5(a) (32×32 pixels)

Fig. 2.9. Laplacian of the monochrome images by means of Eq.(2.12).

2.1.5 Image Rotational Operator

The rotation, another name is curl, is a differential operator for a vector field, giving the vector field orthogonal to the original vector field. The rotation of a vector field $\mathbf{A}$ is given by,

$$\nabla \times \mathbf{A} = \begin{vmatrix} \mathbf{i} & \mathbf{j} & \mathbf{k} \\ \frac{\partial}{\partial x} & \frac{\partial}{\partial y} & \frac{\partial}{\partial z} \\ A_R & A_G & A_B \end{vmatrix}. \tag{2.13}$$

Eq.(2.13) at a given point generates the vectors surrounding the point. When a monochrome image is regarded as one component of the vector potential field, then it is possible to demonstrate the nature of rotation on the images. Let A_B, one of the vector potential component, be a monochrome image, then Eq.(2.13) is reduced into,

$$\nabla \times \mathbf{A} = \left(\frac{\partial}{\partial y}\mathbf{i} - \frac{\partial}{\partial x}\mathbf{j} \right) A_B. \tag{2.14}$$

The practical rotation in a digital image is also carried out by the central finite difference method. Let the distances between the pixels, Δx and Δy, to be unit length, then the rotation of monochrome images is implemented by,

$$\begin{aligned} \nabla \times \mathbf{A}_{i,j} &\simeq \left(\frac{A_{Bi,j+1} - A_{Bi,j-1}}{2\Delta y}\mathbf{i} - \frac{A_{Bi+1,j} - A_{Bi-1,j}}{2\Delta x}\mathbf{j} \right), \\ &\simeq \left(\frac{A_{Bi,j+1} - A_{Bi,j-1}}{2}\mathbf{i} - \frac{A_{Bi+1,j} - A_{Bi-1,j}}{2}\mathbf{j} \right). \end{aligned} \tag{2.15}$$

Figures 2.10 and 2.11 illustrate the rotational fields of a dot and a line, respectively. In this case, the pixel value defines the positive vector potential which is upward from the surface of page. Both of the rotational fields shown in Figs. 2.10 and 2.11, therefore, make counterclockwise arrows. It is obvious that the arrows trace around the pixels having the similar in value and it follows the superposition principle as well.

There are two important mathematical relations in vector fields: One is that the rotation of the gradient field is identically zero, and the other is that the divergence of the rotational field is identically zero; namely,

$$\nabla \times \nabla U = 0, \tag{2.16}$$

and

$$\nabla \bullet \nabla \times \mathbf{A} = 0. \tag{2.17}$$

Introduction of the image vector operations, proposed here, suggests one of the systematic approaches to extract characteristics concerning with target objects on the images [23, 24].

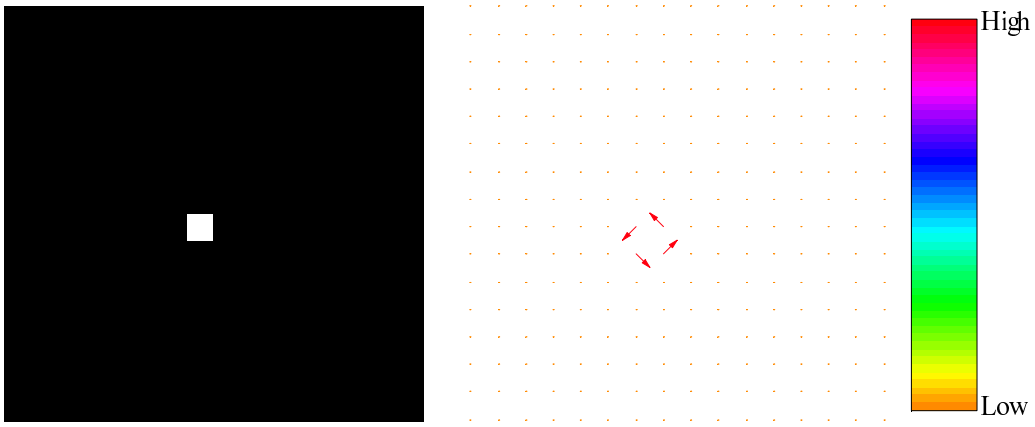

(a) A dot (b) Rotational vectors

Fig. 2.10. Rotational field of a dot (16 × 16 pixels).

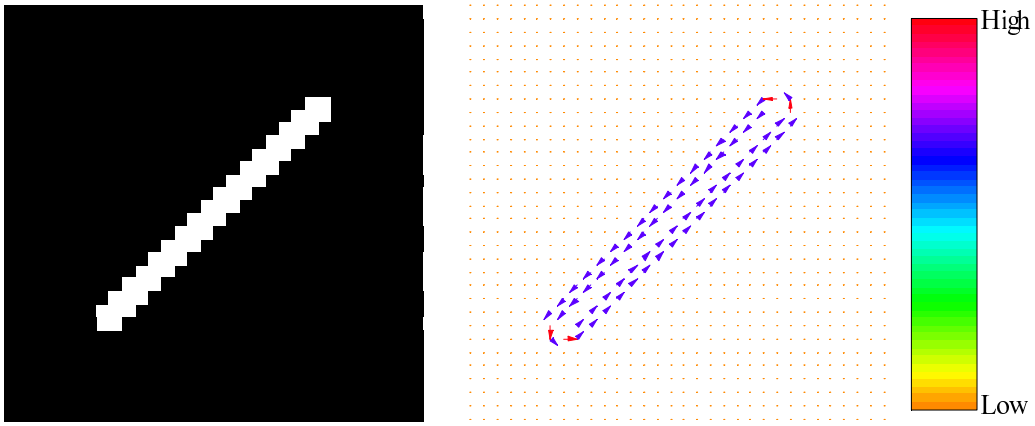

(a) A line (b) Rotational vectors

Fig. 2.11. Rotational field of a line (32 × 32 pixels).

2.1.6 Image Equations

The image modeling by the potential field with the vector operations derives governing equations.

At first, let us consider static images. The static image is the image unchanging on computer screens. In the same way as in electrostatic field, a static monochrome image can be represented by Poisson equation:

$$-\varepsilon\nabla^2 U = \sigma, \tag{2.18}$$

where U, σ, and ε represent a monochrome image, its image source density, and a medium parameter, respectively [18,19]. The image source density σ is derived by the Laplacian of the monochrome image like in Figs. 2.8 and 2.9. The medium parameter ε is used when image filter operations are applied.

In case of color images, the curl curl equation,

$$\nu\nabla\times\nabla\times\mathbf{A} = \nu\nabla\nabla\bullet\mathbf{A}-\nu\nabla^2\mathbf{A}, \tag{2.19}$$

represents a governing equation, since the vector potential field is employed to represent color images. Where ν is a medium parameter having the same function as ε in Eq.(2.18). To solve Eq.(2.19) is quite hard task, however, the idea of Coulomb gauge in electromagnetism:

$$\nabla\bullet\mathbf{A} = 0, \tag{2.20}$$

helps to remove this difficulty. In order to automatically satisfy Eq.(2.20), every color pixel of the color images is defined by,

$$\mathbf{A} = A_R(y,z)\mathbf{i}+A_G(z,x)\mathbf{j}+A_B(x,y)\mathbf{k}. \tag{2.21}$$

This assumption gives that the divergence of the color images is identically zero, namely,

$$\begin{aligned}\nabla\bullet\mathbf{A} &= \left(\frac{\partial}{\partial x}\mathbf{i}+\frac{\partial}{\partial y}\mathbf{j}+\frac{\partial}{\partial z}\mathbf{k}\right)\bullet\left[A_R(y,z)\mathbf{i}+A_G(z,x)\mathbf{j}+A_B(x,y)\mathbf{k}\right],\\ &= \frac{\partial A_R(y,z)}{\partial x}\mathbf{i}+\frac{\partial A_G(z,x)}{\partial y}\mathbf{j}+\frac{\partial A_B(x,y)}{\partial z}\mathbf{k},\\ &= 0.\end{aligned} \tag{2.22}$$

Therefore, Eq.(2.19) is reduced into three independent Poisson equations in terms of the RGB components,

$$-\nu\nabla^2\mathbf{A} = \mathbf{J}, \tag{2.23}$$

or,

$$\begin{aligned} -\nu_R \nabla^2 A_R &= \nu_R \left(\frac{\partial^2 A_R}{\partial y^2} - \frac{\partial^2 A_R}{\partial z^2} \right) = J_R, \\ -\nu_G \nabla^2 A_G &= \nu_G \left(\frac{\partial^2 A_G}{\partial z^2} - \frac{\partial^2 A_G}{\partial x^2} \right) = J_G, \\ -\nu_B \nabla^2 A_B &= \nu_B \left(\frac{\partial^2 A_B}{\partial x^2} - \frac{\partial^2 A_B}{\partial y^2} \right) = J_B, \end{aligned} \tag{2.24}$$

where **J** in Eq.(2.23) denotes color source density consisting of the source densities of RGB components; the subscripts R, G, and B refer to the red, green, and blue components, respectively. Thereby, the color image can be handled as three monochrome images independently. Moreover, holding Coulomb gauge means that the parallel computing/processing could be employed to handle color images. A major difference between color and monochrome images is that the color images require over three times greater size of computation memory as well as CPU resources. However, this difference can be reduced when a parallel processor machine is used. For example, if each of the RGB components is processed in parallel like a monochrome image, then the extra memories and CPU resources are only required to decompose and compose the color image. This means that color images require a similar CPU time to those of the monochrome image when using parallel processor machines [26].

Second, let us consider dynamic images. The dynamics image, that is to say animation, is the image consisting of some static images changing sequentially. In general, the display of dynamic images depends on time. Since Poisson equation represents static images, then the dynamic images can be expressed by time dependent partial differential equations, i.e., Helmholtz type of equations,

$$\varepsilon \nabla^2 U + \sum_{o=1}^{l} \alpha_o \frac{\partial^{(o)} U}{\partial t^{(o)}} = -\sigma, \tag{2.25}$$

where α_o is parameters how much effective the time derivative terms work in the dynamic images. The first term on the left in Eq.(2.25) expresses the spatial expanse due to the Laplacian. The second term on the left concerns about motion of the dynamic images [25]. On the right hand of Eq.(2.25), the source density σ contains also up to the $(l-1)$-times differentiable functions. Obviously for Eq.(2.24), it is possible to independently apply Eq.(2.25) to each of the RGB components in case of color images.

2.2 Static Image Equation

2.2.1 Governing Equations

The static image, which is the image unchanging on computer screens, is represented by Poisson type partial differential equations. The static monochrome and color images are obtained by solutions of the image Poisson equations,

$$\varepsilon \nabla^2 U = -\sigma, \tag{2.26}$$

and,

$$\nu \nabla^2 \mathbf{A} = -\mathbf{J}, \tag{2.27}$$

respectively. If it is possible to recover an image from its source density, then the modeling by Eqs. (2.26) and (2.27) is held.

As mentioned in the previous section, the color image can be handled as three independent monochrome images. Therefore, it is possible to focus on the solution strategies for the monochrome images. Since the image is discretized, then the numerical approximation is essentially required. This section discusses three approaches. The finite difference and Green's function method demonstrate to solve Eq.(2.26), or Eq.(2.27). Fig.2.12 shows monochrome images to verify the governing equation of static images by means of the finite differences and Green's functions [27]. The finite elements discuss the boundary conditions on the partial differential equations for the images.

To denote the discretized Poisson equation leading to the discretized source density $F_{i,j}$ at the position of pixel (i, j), it is assumed that the following equation:

$$\varepsilon_{i,j} \nabla^2 U_{i,j} = F_{i,j}, \tag{2.28}$$

represents the local pixels of static image. Consequently, the discretized Poisson equation gives a linear system of equations:

$$L\mathbf{U} = \mathbf{F}, \tag{2.29}$$

to be solved to generate the static images, where L, $\mathbf{U}$, and $\mathbf{F}$ represent the coefficient matrix corresponding to the Laplacian, solution vector containing the pixel values, and input vector corresponding to the source density $-\sigma$ in Eq.(2.26), respectively [18, 25, 28, 29].

(a) A dot (16×16 pixels) (b) Lenna (128×128 pixels)

Fig. 2.12. Test monochrome images.

2.2.2 Finite Difference Method

The finite difference method is one of the powerful strategies solving differential equations numerically. Direct substitution of the differential terms by finite differences derives relevant formulas from the central difference approximation, Taylor series, and so on. To carry out Eq.(2.28), the pixels on image are assumed to be nodal points of the finite difference method. Two types of finite difference approximations with homogeneous medium parameter $\varepsilon_{i,j} = 1$ are discussed in the present study.

One is a five-points finite difference formula which determines a source density $F_{i,j}$ from five pixel values around the pixel $U_{i,j}$,

$$F_{i,j} = \frac{1}{4}\left(U_{i+1,j} + U_{i-1,j} + U_{i,j+1} + U_{i,j-1} - 4U_{i,j}\right). \tag{2.30}$$

The other is a nine-points finite difference formula which determines a source density $F_{i,j}$ from nine pixel values around the pixel $U_{i,j}$,

$$\begin{aligned} F_{i,j} = \frac{1}{6}(&U_{i-1,j-1} + 4U_{i-1,j} + U_{i-1,j+1} + 4U_{i,j-1} \\ &+4U_{i,j+1} + U_{i+1,j-1} + 4U_{i+1,j} + U_{i+1,j+1} - 20U_{i,j}). \end{aligned} \tag{2.31}$$

Figures 2.13 and 2.14 show the source densities of Figs. 2.12(a) and 2.12(b), respectively. When the numbers of pixels along with the x- and y- directions are m and n, respectively, then the number of elements in

the vectors **U** and **F** to be solved becomes $m \times n$. Therefore, the system matrix L in Eq.(2.29) is a square matrix having $(m \times n)^2$ elements derived by Eqs. (2.30) and (2.31). When the Laplacians in Eqs. (2.30) and (2.31) are carried out, the boundary conditions should be imposed. Here, the zero Dirichlet boundary conditions are set to the edges of the images. More precisely illustrated in Fig.2.15, add pixels outside of the image, then the pixel values are set to zero. After that, the Laplacian is implemented.

If Eq.(2.26) is held, then it is possible to recover the original images from the source densities by solving the vector **U** in Eq.(2.29). Namely, calculating the inverse matrices of L yields the static images. To set up the inverse matrices is quite inefficient and requires much memories due to the sparse matrices in case of the image differential equations. Therefore, a successive over relaxation (SOR) method employing equi-meshed nodal points solves these problems [21]. Figs. 2.16 and 2.17 show the recovered images from the source densities shown in Figs. 2.13 and 2.14, respectively. When Eq.(2.29) is solved, the zero Dirichlet boundary condition is also set to the edges of the images in much the same way as when the Laplacian is carried out. The correlation coefficients become 1 within computational error of 10^{-8} order in every pair of the original images and the source densities, suggesting that Eq.(2.26) is possible to consider as monochrome image representation.

On the other hand, the color image is represented by a vector Poisson equation Eq.(2.27) assuming each of the RGB components to be independent data, as expressed in Eq.(2.24). Let us consider Fig.2.18 as a test color image. At first, the Laplacian is applied to each of the RGB components to obtain the color source density **J**. Fig.2.19 shows the color source densities by means of Eqs. (2.30) and (2.31). The Laplacian removes the constant and first differentiable terms so that most of part in Fig.2.19 is gray color, while the high intensity of color pixels outlines the target, i.e., where higher rate of pixel value variation can be seen. Second, solving Poisson equations with the color source density recovers each of the RGB components. Finally, they are synthesized to display the recovered color images in Fig.2.20.

In this case, assuming Coulomb gauge in Eq.(2.22), three systems of equations having the vectors **U** and **F** with order of $m \times n$ are essentially solved when the numbers of pixels in terms of the x- and y- directions are m and n, respectively. If some relations among the RGB components are given, then the vectors **U** and **F** in Eq.(2.29) have $3 \times m \times n$ elements at most. Thus, the curl curl operation in Eq.(2.19) basically results in a system matrix L having $(3 \times m \times n)^2$ elements.

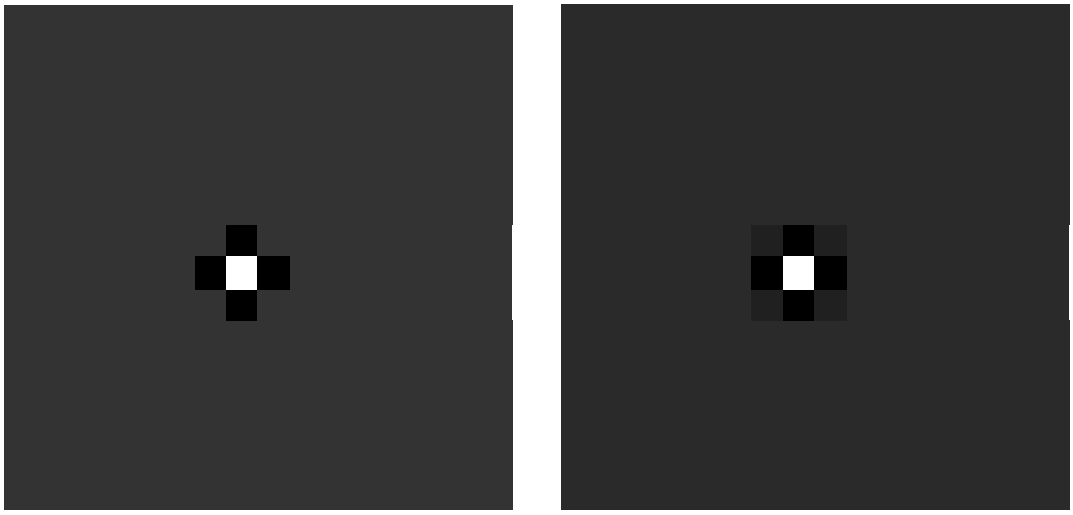

(a) Five-points formula Eq.(2.30) (b) Nine-points formula Eq.(2.31)

Fig. 2.13. Source densities of Fig.2.12(a) (16 × 16 pixels).

(a) Five-points formula Eq.(2.30) (b) Nine-points formula Eq.(2.31)

Fig. 2.14. Source densities of Fig.2.12(b) (128 × 128 pixels).

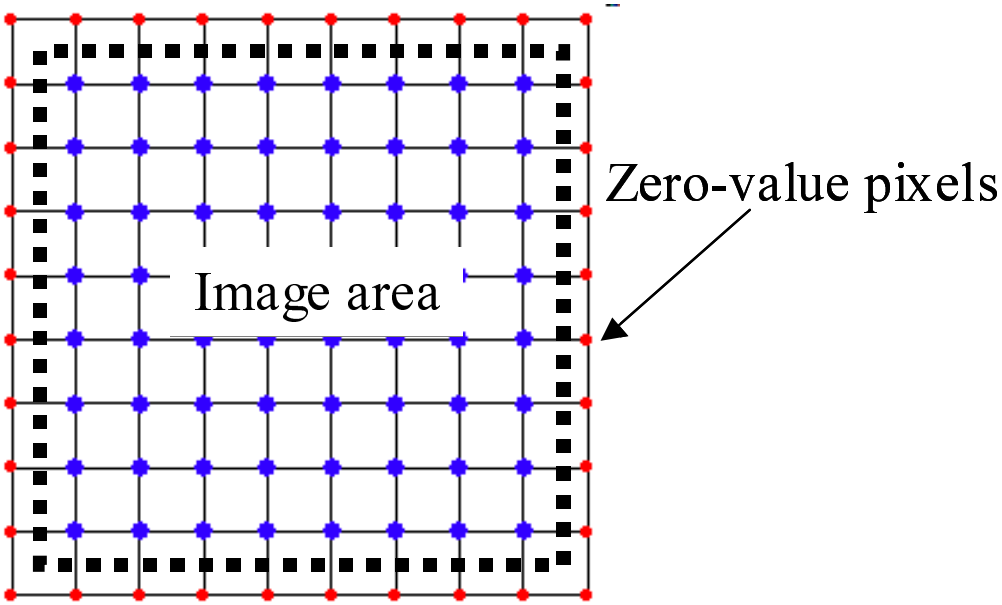

Fig. 2.15. Boundary condition for finite difference method. Extra pixels are added to set up the boundary condition for differential operations. After the operations, the added pixels are removed. Blue and red points represent the original and added pixels, respectively.

(a) Five-points formula Eq.(2.30) (b) Nine-points formula Eq.(2.31)

Fig. 2.16. Image recovery from the source densities in Fig.2.13 by finite difference method (16 $\times$ 16 pixels).

(a) Five-points formula Eq.(2.30) (b) Nine-points formula Eq.(2.31)

Fig. 2.17. Image recovery from the source densities in Fig.2.14 by finite difference method (128 $\times$ 128 pixels).

Fig. 2.18. Test color image (128 × 128 pixels).

(a) Five-points formula Eq.(2.30)

(b) Nine-points formula Eq.(2.31)

Fig. 2.19. Color source densities of Fig.2.18 (128 × 128 pixels).

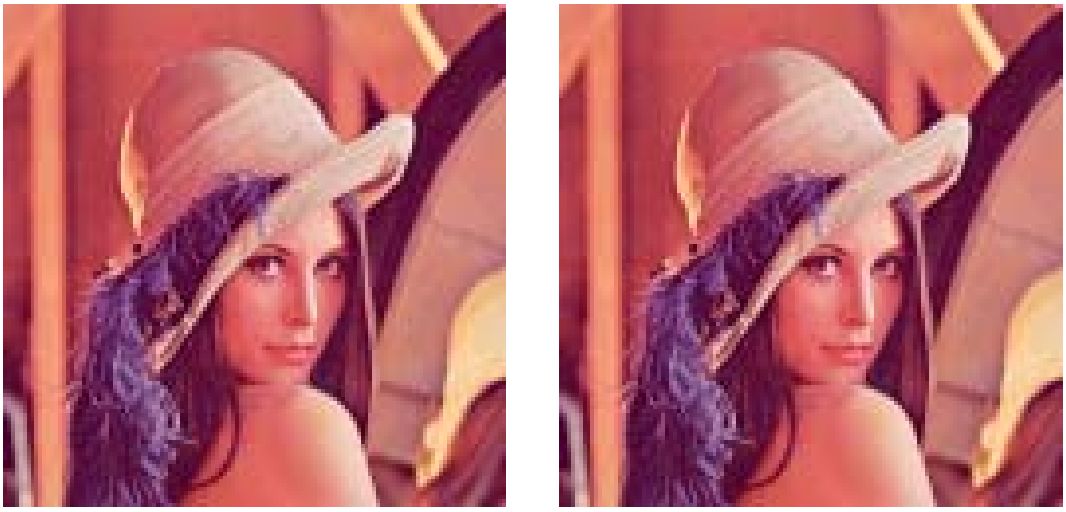

(a) Five-points formula Eq.(2.30) (b) Nine-points formula Eq.(2.31)

Fig. 2.20. Color image recovery from the color source densities in Fig.2.19 by finite difference method (128 $\times$ 128 pixels).

2.2.3 Green's Function Method

As is well known, Poisson equation Eq.(2.26) has a fundamental solution:

$$U = \frac{1}{\varepsilon}\int_{\Omega} g(r)\sigma \mathrm{d}\Omega, \tag{2.32}$$

where Ω is the entire surface containing the source densities in Figs. 2.13 and 2.14; $g(r)$ is Green's function given by,

$$g(r) = \frac{1}{4\pi|r|}. \tag{2.33}$$

In Eq.(2.33), r denotes a distance between the source and field points [30]. Green's function schemes are free from boundary conditions of the differential equations. However, consideration of this distance r reveals a serious difficulty,

$$r \to 0, \quad g(r) \to \infty. \tag{2.34}$$

The condition Eq.(2.34) gives an integral kernel to the solution methodology of Eq.(2.32). This is the intrinsically difficult problem always encountered

in the integral type of solutions. Instead of discussing this problem, the minimum distance is supposed to be $r = 1$ in Eq.(2.33) to discuss the nature of solutions employing Green's functions. Let $r_{(i,j),(is,js)}$ denote the distance between the reference pixel point (i, j) and the source density point (is, js). The pixel $U_{i,j}$ from the source densities is recovered by means of,

$$U_{i,j} = \sum_{is=1}^{m} \sum_{js=1}^{n} \frac{1}{\varepsilon_{is,js}} g(r_{(i,j),(is,js)}) F_{is,js}. \tag{2.35}$$

Eq.(2.35) gives Figs. 2.21 and 2.22 from the source densities shown in Figs. 2.13 and 2.14, respectively. Figs. 2.21 and 2.22 employ the minimum distance $r_{(i,j),(i,j)} = 1$ to avoid the problem on the integral kernels described above. Moreover, the medium parameter ε in Eq.(2.32) are homogeneous. In Fig.2.21, the correlation coefficients between the original and the recovered images are 1. However, in case of Fig.2.22, the correlation coefficients for Figs. 2.22(a) and 2.22(b) are 0.39553 and 0.39314.

Although the rough approximation Eq.(2.34) applies to solve the integral kernel problem, the major errors are mainly composed of the corners of image due to the source densities given by finite difference methods. Figs. 2.21 and 2.22 demonstrate that the continuity of Green's function $g(r)$ works a smooth and continuous potential distribution, suggesting that great possibility of Green's solution strategy.

On the other hand, consider the system of equations derived from Green's function Eq.(2.35), otherwise Eq.(2.32), then it reduces into:

$$G\mathbf{F} = \mathbf{U}, \tag{2.36}$$

where the order of the vectors $\mathbf{U}$ and $\mathbf{F}$ is $m \times n$ when the numbers of pixels along with the x- and y- directions are m and n, respectively. Moreover, the matrix G is a system matrix constituting Green's function. It is obvious that the inversion of matrix G is equivalent relation to the matrix L in Eq.(2.29). This means that the inverse matrix G^{-1} gives the Laplacian based on Green's function. Namely, producting G^{-1} and $\mathbf{U}$ yields the source density $\mathbf{F}$. Fig.2.23 shows the source densities of the test monochrome images in Fig.2.12. Moreover, Fig.2.24 shows the recovered images from Fig.2.23 with exact reproducibility. Fig.2.23(a) reveals that the source densities spread all over the image, and it is similar pattern to the nine-points finite difference approximation just around the targeting pixel. In case of the finite difference method, it is assumed that the solution can be expanded by Taylor series. Higher order approximation of the finite difference method is realized by considering coefficients of higher order terms on Taylor series, whereas Green's function strategy yields a kind of the generalized discretization for the Laplacian that takes all the reference points into account.

(a) Five-points formula Eq.(2.30) (b) Nine-points formula Eq.(2.31)

Fig. 2.21. Image recovery from the source densities in Fig.2.13 by Green's function (16×16 pixels).

(a) Five-points formula Eq.(2.30) (b) Nine-points formula Eq.(2.31)

Fig. 2.22. Image recovery from the source densities in Fig.2.14 by Green's function (128×128 pixels).

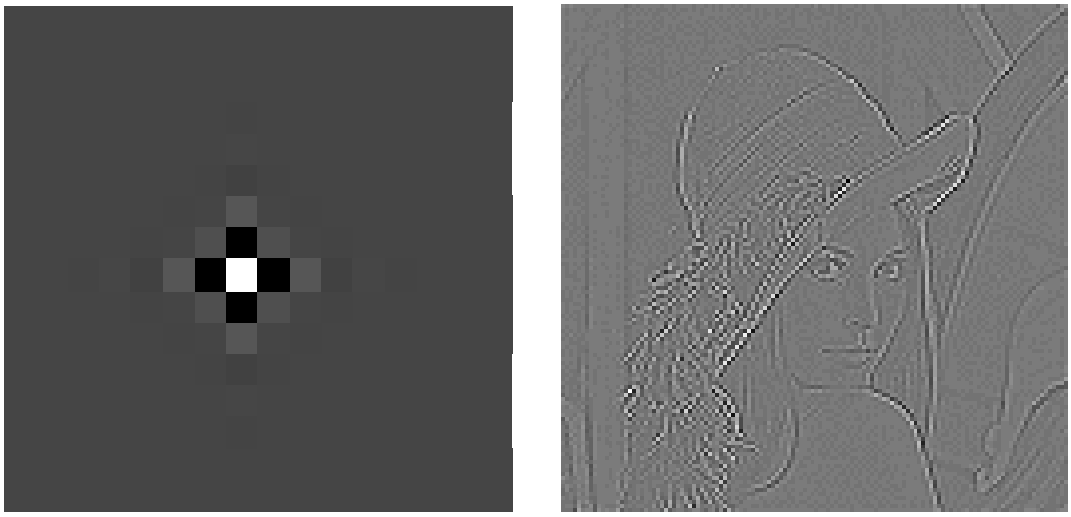

(a) A dot (16 × 16 pixels) (b) Lenna (128 × 128 pixels)

Fig. 2.23. Source density distributions by the Laplacian derived from Green's function.

(a) A dot (16 × 16 pixels) (b) Lenna (128 × 128 pixels)

Fig. 2.24. Image recovery from the source densities shown in Fig.2.23 by means of Green's function.

2.2.4 Finite Element Method

A formal solution of Eq.(2.26) by the variational principle is given by minimizing following functional:

$$W(U^*) = \frac{1}{2}\int_s \varepsilon(\nabla U^*)^2 \mathrm{d}s - \int_s \sigma U^* \mathrm{d}s, \tag{2.37}$$

where s denotes the entire surface containing all of the source densities in Figs. 2.13 and 2.14; and U^* is an approximate solution interpolated by a set of the space variables x and y. Eq.(2.38) gives the approximate solution U^*:

$$U^* = U + \xi\varphi, \tag{2.38}$$

where ξ and φ are the numerical parameter and differentiable function; and $\xi\varphi$ denotes an error, respectively. Substituting Eq.(2.38) into Eq.(2.37) divides into the functionals of true and excess terms:

$$W(U^*) = W(U) + \xi\int_s (\varepsilon\nabla U \bullet \nabla\varphi - \sigma\varphi)\mathrm{d}s + \frac{\xi^2}{2}\int_s \varepsilon(\nabla\varphi)^2 \mathrm{d}s. \tag{2.39}$$

The first variation of Eq.(2.39) gives,

$$\begin{aligned}
\Delta W &= \lim_{\xi\to 0}\frac{W(U^*) - W(U)}{\xi}, \\
&= \lim_{\xi\to 0}\left[\int_s \{\varepsilon\nabla U \bullet \nabla\varphi - \sigma\varphi\}\,\mathrm{d}s + \frac{1}{2}\int_s \xi(\nabla\varphi)^2 \mathrm{d}s\right], \\
&= \int_s \{\varepsilon\nabla U \bullet \nabla\varphi - \sigma\varphi\}\,\mathrm{d}s, \\
&= 0.
\end{aligned} \tag{2.40}$$

Green's theorem rewrites Eq.(2.40) to,

$$\begin{aligned}
\Delta W &= -\int_s \varphi\left(\varepsilon\nabla^2 U + \sigma\right)\mathrm{d}s + \oint_c \varphi\frac{\partial U}{\partial n_c}\cdot \mathrm{d}\mathbf{l}, \\
&= 0,
\end{aligned} \tag{2.41}$$

where $\partial/\partial n_c$ and $\mathbf{l}$ are the normal derivative and line enclosing the target area s, respectively. Thus, the first variation of the functional Eq.(2.37) finds

$$\varepsilon\nabla^2 U = -\sigma, \tag{2.42}$$

$$\frac{\partial U}{\partial n_c} = 0. \tag{2.43}$$

Apply a triangular mesh system and the first order interpolating function of the variables x and y for the approximate solution,

$$U^*(x,y) = a + bx + cy \quad \text{or} \quad \begin{pmatrix} 1 & x & y \end{pmatrix} \begin{pmatrix} a & b & c \end{pmatrix}^T, \qquad (2.44)$$

then the first variation ΔW derives a system of equations, in Eq.(2.29), giving the finite element solution of Eq.(2.26).

Figures 2.25 and 2.26 show the recovered images by the finite elements employing zero Dirichlet boundary conditions around the edges of the images. These images are also obtained from the source densities derived by Eqs. (2.30) and (2.31). In Fig.2.25, the correlation coefficients among the original image and the recovered images, i.e., Figs. 2.25(a) and 2.25(b), are 1 and 0.99326, respectively. In case of Fig.2.26, the correlation coefficients for Figs. 2.26(a) and 2.26(b) are 1 and 0.99877, respectively. The original image used in the demonstration of Fig.2.26 is a pixel-resampled image of Fig.2.12(b). The coefficient matrices of L in Eq.(2.29) derived from the five-points finite differences and the finite elements employing right-angle isosceles triangular elements are identical. Therefore, the source densities by means of Eq.(2.30) give exact solutions.

As is well known, the finite elements result in solving a linear system of equations like in Eq.(2.29). Employing fine mesh systems is inefficient for image handling because a large size sparse system matrix is always associated with finite elements. However, one of the advantages to use finite elements is that adaptive mesh systems can be applied to reduce the number of pixels to be computed. An example of coarse mesh systems is shown in Fig.2.27. Non-zero value of the source density given in Fig.2.27(b) determines where the nodal points should be set up. In this case, the number of nodal points can be reduced to 36.3 % of pixels in the original image.

Finite element method is also convenient to discuss the boundary conditions in this image modeling because it automatically satisfies Neumann type boundary condition expressed in Eq.(2.43). Obviously, setting the symmetrical boundary condition to all edge of the image gives a singular system matrix L in Eq.(2.29), resulting in solving an ill-posed linear system [31]. Let us consider a zero-and-symmetrical mixed boundary condition to check up the effect of boundary conditions. Fig.2.28 shows a verified set of boundary conditions and the recovered image. The right side of Fig.2.28(b) where Neumann boundary condition is imposed becomes large in pixel values. The effect of boundary condition plainly destroys the original image. This is because the boundary condition differs from the operation of the Laplacian. Thus, the boundary condition should be the same as that of the source density calculation.

(a) Five-points formula Eq.(2.30) (b) Nine-points formula Eq.(2.31)

Fig. 2.25. Image recovery from the source densities in Fig.2.13 by finite element method (16×16 pixels).

(a) Five-points formula Eq.(2.30) (b) Nine-points formula Eq.(2.31)

Fig. 2.26. Image recovery from the source densities in Fig.2.14 by finite element method (64×64 pixels).

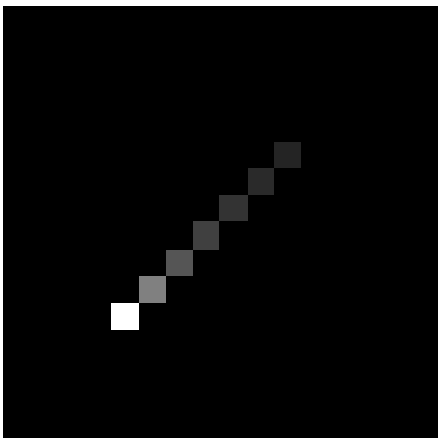

(a) Original image

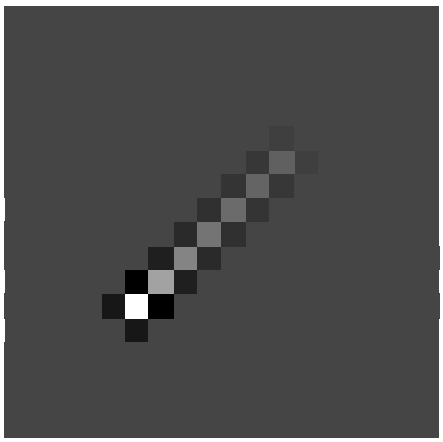

(b) Source density by Eq.(2.30)

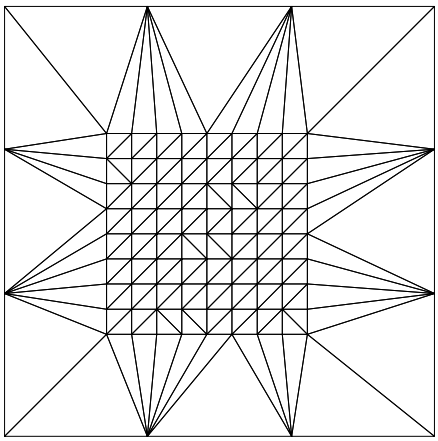

(c) Coarse mesh system

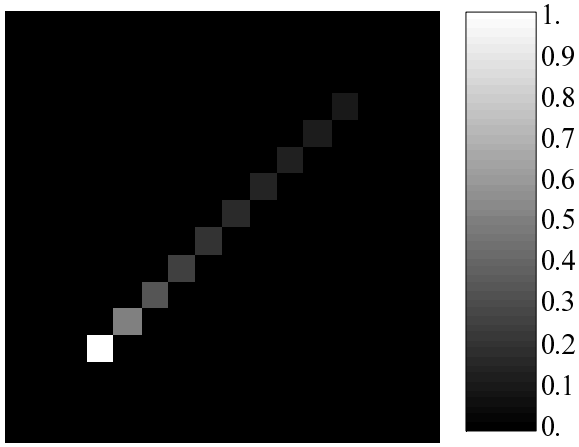

(d) Recovered image

Fig. 2.27. Coarse mesh system to recover image (16 $\times$ 16 pixels).

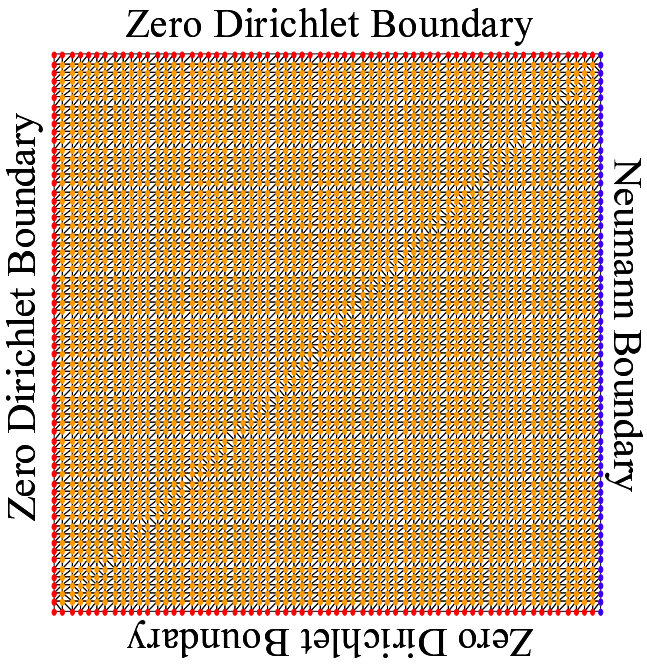

(a) Verified boundary conditions

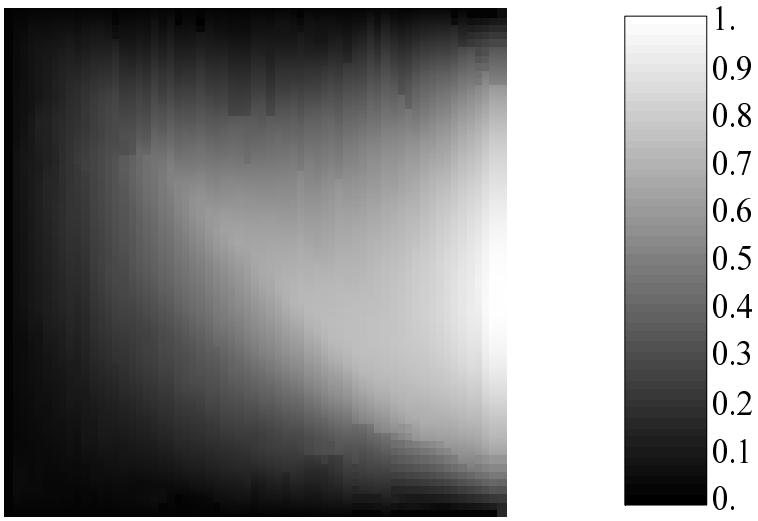

(b) Recovered image

Fig. 2.28. Verification of boundary conditions (64 × 64 pixels). The original image is the same as that in Fig.2.26.

2.2.5 Image Modification

One of the attractive contents of the image modeling is that solving the partial differential equation and Green's function systemizes the image processing.

At first, employing fine mesh system to solve Eq.(2.26) or Eq.(2.27) with low resolution source densities enables to generate high resolution of images. Figs. 2.29 and 2.30 show the demonstration of image resolution enrichment. After Laplacian is applied to the original images in Figs. 2.12(a) and 2.12(b) to obtain their source densities, then the image recovery is carried out. The fine mesh system to the source densities is used to increase the number of pixels. In these cases, the number of nodal points is increased to 150 % when solving Eq.(2.29) with the source densities. It is obvious that the image Poisson equation is able to change the number of pixels and smoothly generates the images.

Second, the image Poisson equation makes it possible to change aspect ratio of the images in much the same way as demonstrated above. Fig.2.31 shows examples of aspect ratio modification. The finite difference method performs the modification from the source density derived by Eq.(2.31). In these cases, the subdivision ratio of spatial stepwidths with respect to the horizontal or vertical directions determines the aspect ratio of images. Although the pixels are discretized, solving the image Poisson equation is capable of modifying resolution as well as aspect ratio of the images according to the partial differential equations.

Finally, a method of image emphasis/deemphasis is demonstrated. Considering the medium parameter ε when the image Poisson equation is solved, then the points where the new medium parameters are reset up are targets to be emphasized/deemphasized. Namely, the image recovery is carry out after applying the medium parameter to each point on the source density distribution. Figs. 2.32 and 2.33 demonstrate image emphasis and deemphasis by means of the image Poisson equation, respectively. Both figures show the arranged source densities and emphasized/deemphasized images. Fig.2.32 emphasizes around Lenna's eyes so that the value of source density around her eyes is amplified. The recovered image looks smoothly and accomplishes the image emphasis. On the other hand, Fig.2.33 deemphasizes her face so that the value of source density on her face is attenuated. The recovered image looks also smoothly and works out the image deemphasis.

The demonstration, shown in this section, reveals that the medium parameter ε works as a kind of image filters that make it possible to carry out image processing. Thus, the image source density representation systemizes image processing.

(a) Five-points formula Eq.(2.30) (b) Nine-points formula Eq.(2.31)

Fig. 2.29. Image resolution enrichment from 16 × 16 pixels-source densities in Fig.2.13 to the images having 24 × 24 pixels.

(a) Five-points formula Eq.(2.30) (b) Nine-points formula Eq.(2.31)

Fig. 2.30. Image resolution enrichment from 128 × 128 pixels-source densities in Fig.2.14 to the images having 192 × 192 pixels.

(a) V:H=1:1.5

(b) V:H=1.5:1

Fig. 2.31. Aspect ratio modification from Fig.2.12(b). V and H denote the expansion ratios in the horizontal and vertical directions, respectively. The resolution of the original image is 128 $\times$ 128 pixels.

(a) Arranged source density (b) Recovered image

Fig. 2.32. Image emphasis by arranged source density around Lenna's eyes (128 × 128 pixels).

(a) Arranged source density (b) Recovered image

Fig. 2.33. Image deemphasis by arranged source density around Lenna's face (128 × 128 pixels).

2.3 Dynamic Image Equation

2.3.1 Governing Equations

As verified in the previous section, the static image can be represented by the image Poisson equation. The solution of image Poisson equation generates any types of images from their image source density representation and accomplishes image resolution enrichment, image emphasis, and compression accompanied with the solution strategies.

On the other hand, dynamic images, i.e., animations, never work continuously, but they contain a large number of static images, so-call frames, to smoothly play back. For instance, two frames, shown in Fig.2.34, are a minimum set to realize a dynamic image by switching them. This means that representation for dynamic images also relates to the governing equation of static images. Therefore, a Helmholtz type governing equation can be considered since it includes Poisson equation itself. Helmholtz type of equations covers most of representation for physical dynamic systems, for instance, fluid dynamics in mechanical engineering, electromagnetodynamic field expressed by Maxwell's equations, Schrödinger's equation in quantum mechanics, etc. The image modeling proposed in the present study also results in the same manner [25, 32].

The Helmholtz type partial differential equation consists of the spatial as well as time derivative terms. The representative Helmholtz type equation in physical systems is as follow:

$$\varepsilon \nabla^2 U + \alpha_1 \frac{\partial U}{\partial t} + \alpha_2 \frac{\partial^2 U}{\partial t^2} \quad = \quad -\sigma. \tag{2.45}$$

where t, ε, α_1, α_2, and σ express the time, medium parameter, velocity parameter, repetitive moving speed parameter, and time-dependent source density, respectively. The Helmholtz type equation in Eq.(2.45) is classified into two types. One is the diffusion equation when $\alpha_1 \neq 0, \alpha_2 = 0$, and the other is the wave equation when $\alpha_1 = 0, \alpha_2 \neq 0$. The former represents a spreading or shrinking animation, and the latter represents a vibrating or repetitive animation. Furthermore, when $\alpha_1 = 0, \alpha_2 = 0$ is considered, then Eq.(2.45) is reduced into the image Poisson equation in Eq.(2.26), meaning that stopping animation, i.e., static images, can be obtained from Eq.(2.45). Thereby, the image Helmholtz equation Eq.(2.45) is able to generate any types of animation.

(a) Initial frame (b) Final frame

Fig. 2.34. A couple of sample images for the initial and final frames of dynamic image (240 $\times$ 240 pixels).

2.3.2 Discretization

The dynamics image in digital computers is composed of static images sequentially changing with a switching time step Δt. Therefore, discretization of Eq.(2.45) is also essentially required in terms of not only spatial derivatives but also time derivatives.

For the discretization on spatial derivatives, Section 2.2 discusses how Laplacian works in the image modeling. On the other hand, an approach of the state variables reduces higher order time derivative terms into the first order time derivative form. Thereby, a system of equations having the first order time derivative term is considered.

Since L denote a coefficient matrix corresponding to the Laplacian in Eq.(2.29), as well as Eq.(2.45), then the discretized Helmholtz equation is given by,

$$\left[L + \frac{\partial}{\partial t}T\right]\mathbf{U} \quad = \quad \mathbf{F}, \tag{2.46}$$

where T, $\mathbf{U}$, and $\mathbf{F}$ denote the coefficient matrix corresponding to the time derivative terms, vector representing pixel values, and input vector corresponding to the source density, respectively. When the numbers of pixels with respect to the x- and y- directions are m and n, respectively, then the number of elements in the vectors $\mathbf{U}$ and $\mathbf{F}$ becomes $m \times n$. However, it depends on the needed order time derivatives of the image Helmholtz equation.

In case that the first and second order time derivatives are considered, these vectors are constituted by $2 \times m \times n$ elements. In this section 2.3, the case of the first order time derivative, i.e., a diffusion equation, is discussed to show a procedure to derive a general solution for the dynamic images.

2.3.3 Modal Analysis

In order to derive a general solution of Eq.(2.46), a modal analysis is carried out [33].

At first, apply the inverse matrix T^{-1} to both side of the system equation in Eq.(2.46). Denoting $T^{-1}L$ as Γ simplifies the time derivative term:

$$\left[\Gamma + \frac{\partial}{\partial t} I\right] \mathbf{U} = T^{-1}\mathbf{F}, \tag{2.47}$$

where I is an identity matrix with order $m \times n$.

Second, let us consider the following homogeneous equation:

$$\left[\Gamma + \frac{\partial}{\partial t} I\right] \mathbf{U} = \mathbf{0}. \tag{2.48}$$

If the matrices L and T in Eq.(2.46) are symmetric forms and L is a positive definite matrix, then it is possible to evaluate the $m \times n$-th characteristic values and their associated characteristic vectors $\mathbf{v}_i$, $i = 1, 2, \cdots, m \times n$. The modal matrix M consisting of the characteristic vectors as its column vectors is defined as,

$$M = \left[\mathbf{v_1}, \mathbf{v_2}, \ldots, \mathbf{v_{m \times n}}\right]. \tag{2.49}$$

Third, the linear transformation of the vector $\mathbf{U}$, namely,

$$\mathbf{U} = M\mathbf{C}, \tag{2.50}$$

rewrites Eq.(2.48) to,

$$\left[M^{-1}\Gamma M + \frac{\partial}{\partial t}\left(M^{-1} I M\right)\right] \mathbf{C} = M^{-1}T^{-1}\mathbf{F}, \tag{2.51}$$

where

$$M^{-1}\Gamma M = \mathrm{diag}\left[\lambda_1, \lambda_2, \ldots, \lambda_{m \times n}\right], \tag{2.52}$$

$$M^{-1} I M = I, \tag{2.53}$$

$$M^{-1}T^{-1}\mathbf{F} = \left[g_1, g_2, \ldots, g_{m \times n}\right]^T, \tag{2.54}$$

$$\mathbf{C} = \left[C_1, C_2, \ldots, C_{m \times n}\right]^T. \tag{2.55}$$

Thereby, the elements of vector $\mathbf{C}$, $C_i, i = 1, 2, \ldots, m \times n$, are given by the first order differential equations:

$$C_i = \frac{g_i}{\lambda_i + \frac{\partial}{\partial t}}. \tag{2.56}$$

Let $C_i(0)$ be an initial value of C_i, then the solution $C_i(t)$ results in,

$$C_i(t) = \left[C_i(0) - \frac{g_i}{\lambda_i}\right] \mathrm{e}^{-\lambda_i t} + \frac{g_i}{\lambda_i}. \tag{2.57}$$

Finally, the general solution $\mathbf{U}(t)$ can be obtained by means of Eq.(2.50),

$$\mathbf{U}(t) = \mathrm{e}^{-\Lambda t}\left[\mathbf{U}(t_S) - \mathbf{U}(t_L)\right] + \mathbf{U}(t_L), \tag{2.58}$$

$$\Lambda = \mathrm{diag}\left[\lambda_1, \lambda_2, \ldots, \lambda_{m\times n}\right], \tag{2.59}$$

where $\mathbf{U}(t_S)$ and $\mathbf{U}(t_L)$ denote the initial and final frames in animation, respectively; and $\lambda_i, i = 1, 2, \ldots, m \times n$, are the characteristic values of matrix Γ in Eq.(2.47); moreover, $\mathrm{e}^{-\Lambda t}$ is a diagonalized state transition matrix concerning with the time transition of animation. If the initial frame, final frame, and relevant state transition matrix are given, then it is possible to generate any frame of animation analytically.

2.3.4 Equivalent Characteristic Value

The general solution of the image Helmholtz equation given by Eq.(2.58) requires a couple of frames and state transition matrix at least. Since the medium parameters concerned with the time derivative terms are not given, then the state transition matrix is unknown.

Here, one of the methodologies to determine the state transition matrix from the given frames of animation is proposed. If the solution $\mathbf{U}(t)$ is assumed to be one of the frames of animation, then it is possible to determine the elements in the matrix Λ by rearranging Eq.(2.58):

$$\Lambda = -\frac{1}{\Delta t} \ln\left[\frac{\mathbf{U}(t_S + \Delta t) - \mathbf{U}(t_L)}{\mathbf{U}(t_S) - \mathbf{U}(t_L)}\right]. \tag{2.60}$$

Substituting the matrix Λ into the general solution Eq.(2.58) generates the frames of animation during $t_S \le t \le t_L$. Therefore, the time step Δt should be less than $t_L - t_S$. Since the matrix Λ is a diagonal matrix, then Eq.(2.60) is carried out at each corresponding pixel value of three frames of animation. By means of Eq.(2.60), generating animation needs three frames in stead of given state transition matrix. The matrix Λ, which corresponds to the

characteristic value matrix, can be determined from given data. Thereby, it is called the method of *equivalent characteristic value* [34,35].

To demonstrate generating animation, two images shown in Fig.2.34 are used as the initial and final frames of animation. A frame existing between initial and final frames is approximately generated by averaged pixel values of the initial and final frames, as shown in Fig.2.35. Fig.2.36 shows the equivalent characteristic values determined by three images based on Eq.(2.60). The position of the elements corresponds to that of the pixels. Because of the logarithmic function in Eq.(2.60), the obtained equivalent characteristic value become complex number. The equivalent characteristic values approximate the state transition matrix $e^{-\Lambda t}$. In this case, the frame generated by means of Eqs. (2.58) and (2.60) is constrained to be $\mathbf{U}(t_S+\Delta t)$ at $t = t_S+\Delta t$.

Fig. 2.35. Generated medium frame for $t = (t_S + t_L)/2$ (240×240 pixels).

2.3.5 Generation of Animation

The method using Eqs. (2.58) and (2.60) generates the animation according to the image Helmholtz equation. The exponential function in Eq.(2.58) makes it possible to generate the frames continuously. In this demonstration, the initial time t_S and final time t_L are set to 0 and 3.0, respectively and the medium frame shown in Fig.2.35 is the image at $t = (t_S + t_L)/2 = 1.5$.

Figure 2.37 summarizes transition of correlation coefficients among the given and generated frames shown in Fig.2.38. It is obvious that Fig.2.38(f) is equivalent to Fig.2.35 in terms of correlation coefficient. On the other hand, Fig.2.38(i) which is generated at the final time $t = t_L = 3.0$ is different from the final frame Fig.2.34(b). This is because Eq.(2.58) converges to the final frame $\mathbf{U}(t_L)$ when time t reaches infinity.

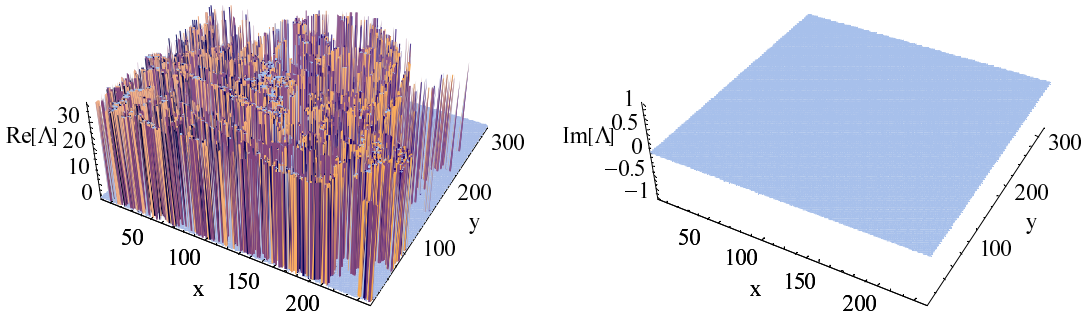

(a) Real part (b) Imaginary part

Fig. 2.36. Equivalent characteristic values by means of Eq.(2.60) (240 × 240 elements). Figs. 2.34(a), 2.34(b), and 2.35 are used.

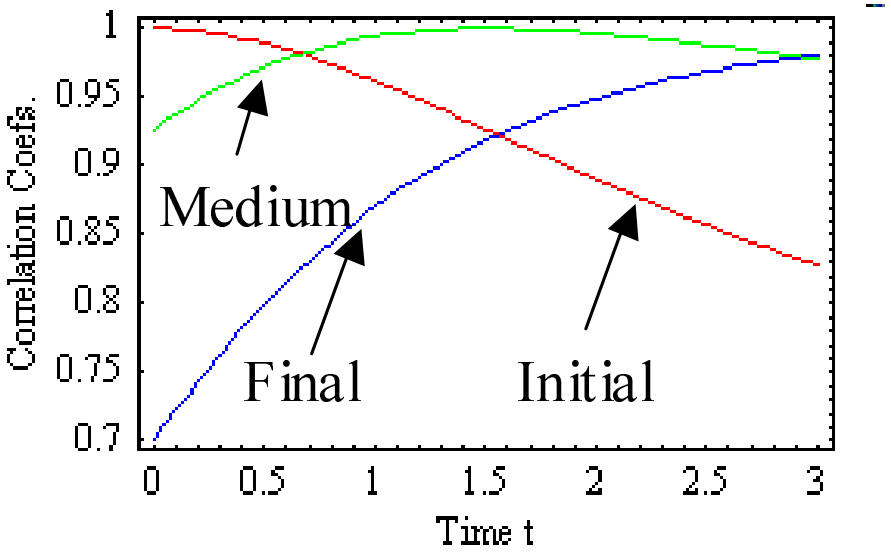

Fig. 2.37. Transition of correlation coefficients among the given and generated frames. Red, green, and blue indicate the correlation coefficients of the initial, medium, and final frames, respectively.

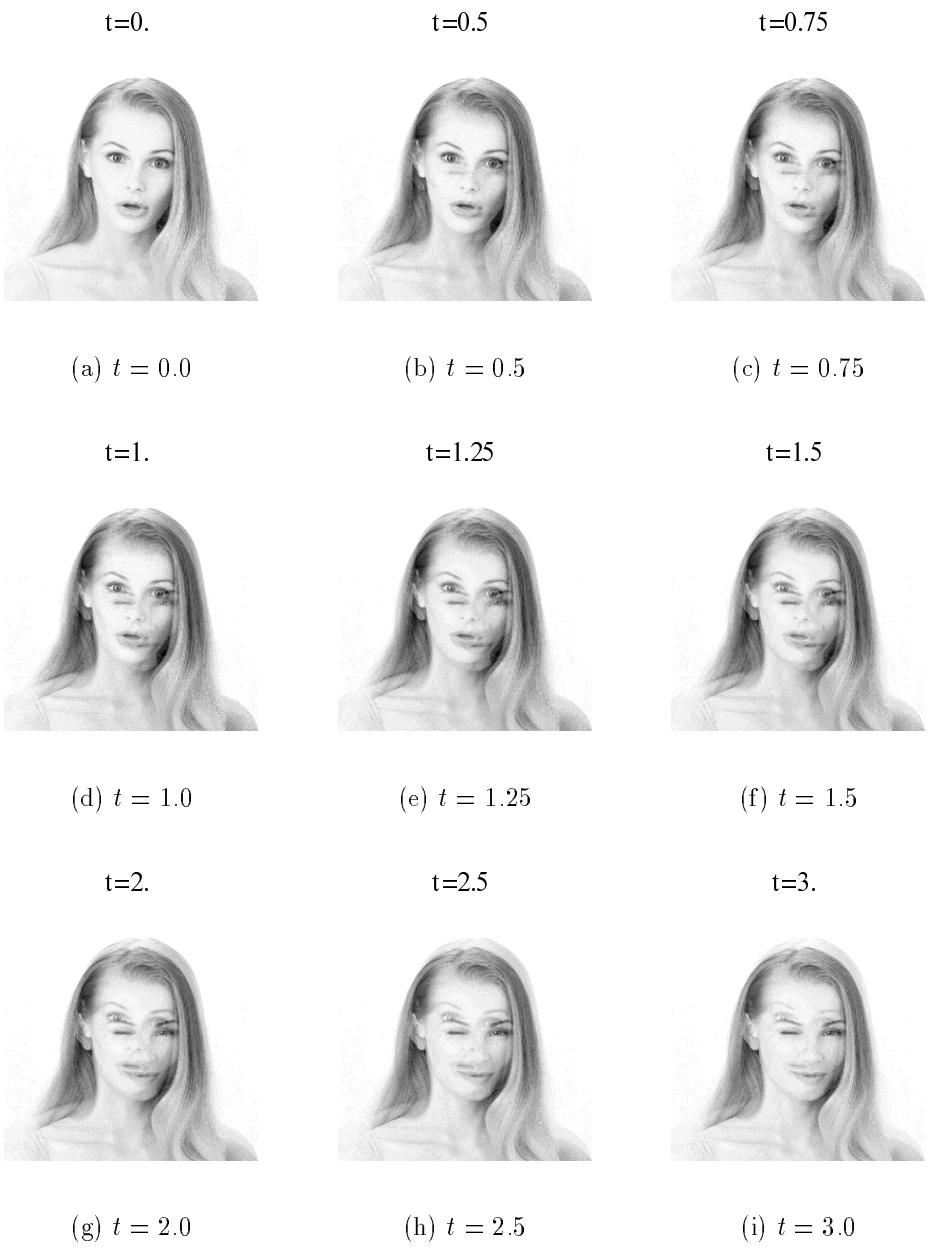

Fig. 2.38. Generated frames of animation by means of Eqs.(2.58) and (2.60) (240×240 pixels).

Further verification having definite physical meaning is considered in the imaged magnetic vector potential distribution obtained from the finite element solutions. A two-dimensional finite element analysis calculates the magnetic field of a magnetic material. The magnetic vector potential on the nodal points of finite elements is imaged as the contrast to make an animation. The calculated magnetic vector potential images are sampled with a constant time interval, then the generated frames by means of the image Helmholtz equation are compared with the finite element solutions.

The constitutive equation representing dynamic magnetic hysteresis is given by,

$$\mathbf{H} + \frac{\mu_r}{s}\frac{\mathrm{d}\mathbf{H}}{\mathrm{d}t} = \frac{\mathbf{B}}{\mu} + \frac{1}{s}\frac{\mathrm{d}\mathbf{B}}{\mathrm{d}t}, \tag{2.61}$$

where $\mathbf{H}$, $\mathbf{B}$, μ, μ_r, and s are the magnetic field (A/m), magnetic flux density (T), permeability (H/m), reversible permeability (H/m), and hysteresis parameter (Ω/m), respectively [36–39].

Let us consider a two-dimensional problem on the magnetic vector potential distribution. The target to be analyzed is an infinitely long magnetic material bar having a rectangular cross section as shown in Fig.2.39. Then the current density is impressed as a step function to the direction perpendicular to the paper space. The constitutive equation in Eq.(2.61) derives the governing equation for the z-component of magnetic vector potential A_z (Wb/m) from the quasi-static condition of electromagnetic fields:

$$\left(\frac{1}{\mu} + \frac{1}{s}\frac{\partial}{\partial t}\right)\nabla^2 A_z - \kappa\frac{\partial}{\partial t}\left(1 + \frac{\mu_r}{s}\frac{\partial}{\partial t}\right)A_z = -\left(1 + \frac{\mu_r}{s}\frac{\partial}{\partial t}\right)J_z, \tag{2.62}$$

where $J_z(\mathrm{A/m^2})$ denotes the z-component of the impressed current density. Employing the triangular finite elements with first order interpolating function subdivides the target region, and then the zero Dirichlet boundary condition $A_z = 0$ is set to the boundary of magnetic material. To solve this second order partial differential equation, Laplace transform with state variable equations is employed, calculating a transient magnetic vector potential to generate its animation frames. Table 2.1 lists the parameters used in the calculation.

The finite element solution from $t = 0$ s to $t = 25$ s is sampled every 5s to make an animation, then the image Helmholtz equation is applied. Three frames of the animation derive the equivalent characteristic value matrix Λ in Eq.(2.60). Define one of the periods with three sampled frames $\mathbf{U}(i -$

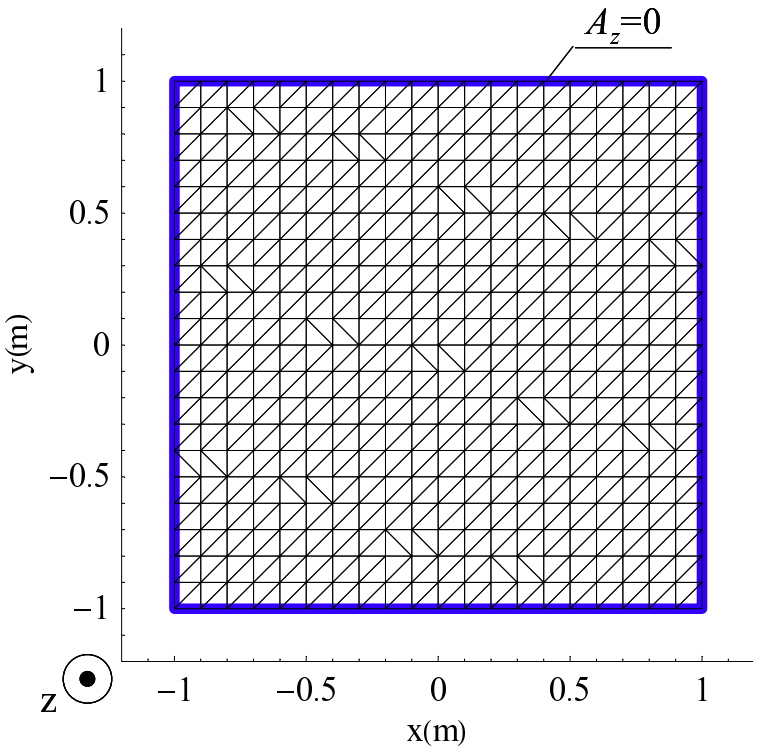

Fig. 2.39. Model for numerical simulation of magnetodynamics.

Table 2.1. Parameters used in the calculation.

Permeability	μ	500 μ_0	H/m
Reversible permeability	μ_r	50 μ_0	H/m
Hysteresis parameter	s	1.0×10^{-4}	Ω/m
Conductivity	κ	1.0×10^{4}	S/m
Impressed current density	J_z	1000	A/m^2
Number of nodal points		441	
Number of triangular elements		800	

$\Delta t), \mathbf{U}(i)$, and $\mathbf{U}(i+\Delta t)$, then the equivalent characteristic value matrix Λ_i in each of the periods is sequentially obtained by,

$$\Lambda_i = -\frac{1}{\Delta t} \ln \left[\frac{\mathbf{U}(i) - \mathbf{U}(i+\Delta t)}{\mathbf{U}(i-\Delta t) - \mathbf{U}(i+\Delta t)} \right], i = 2\Delta t, 3\Delta t, \ldots, (l-1)\Delta t, \tag{2.63}$$

where l corresponds to the number of frames. The time step Δt is 5 s in this case.

Figure 2.40 shows the equivalent characteristic value distributions in each of the periods. Substituting the equivalent characteristic value matrix Λ_i represented in Fig.2.40 into the general solution in Eq.(2.58) gives the magnetic vector potential distributions as generated animation frames. Fig.2.41 shows the generated magnetic vector potential distributions compared with the finite element solutions. The results shown in Fig.2.41 compare the solutions between the sampled times. Fig.2.42 gives the correlation coefficients between the solutions of finite elements and image Helmholtz equations. It is obvious that the method of image Helmholtz equation makes it possible to estimate the frame at arbitrary time from sequentially given three frames. Although the image Helmholtz equation here takes into account only first order time derivative term, it is possible to estimate accurately the frames of the partial differential equation having both the first and second order time derivative terms.

Furthermore, Fig.2.40 reveals some remarkable features. At first, the amplitude of magnetic vector potentals is inhomogeneous on the distribution. However, the equivalent characteristic value becomes a constant since the same parameters and governing equation are applied in each of the triangular elements. Therefore, the equivalent characteristic value is independent of the amplitude/value of pixels. Second, the equivalent characteristic values obtained in this verification can be classified into two cases. One is larger value, shown in Fig.2.40(a), the other is smaller value, shown in Figs. 2.40(b)-(e). Because of the second order time derivative, two equivalent characteristic values can be obtained. It can be considered that the characteristic value corresponding to the dynamics is extracted by means of Eq.(2.63). More precisely, since the larger characteristic value represents the dynamic of fast responce, then the dynamics during $0 \leq t < 5$ s is represented by large in equivalent characteristic value. Figs. 2.40(b)-(e) mean that the responce converges upon a steady state after $t = 5$ s. Finally, the equivalent characteristic value keeps a constant independent of time on the steady state.

When the image Helmholtz equation having only first order time derivative is employed, the equivalent characteristic value represents the dominated

dynamics during the target period and the averaged characteristic value can be obtained. As verified above, the equivalent characteristic value is capable of extracting the dynamics from the frame of animation, suggesting that it makes it possible to clarify the dynamics of physical systems imaged by visualizing devices.

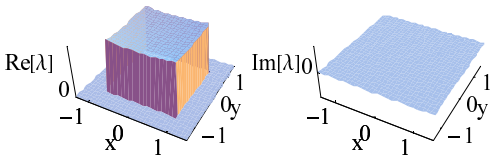

(a) $0 \leq t < 5$ s

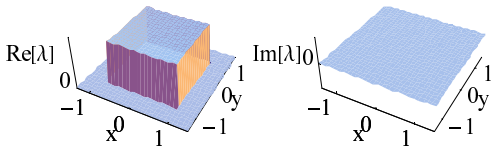

(b) $5 \leq t < 10$ s

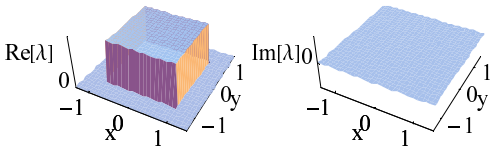

(c) $10 \leq t < 15$ s

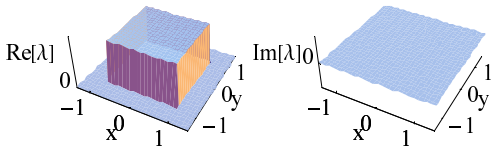

(d) $15 \leq t < 20$ s

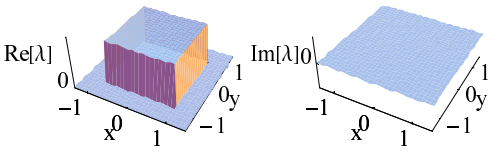

(e) $20 \leq t < 25$ s

Fig. 2.40. Equivalent characteristic value distributions in each of the periods.

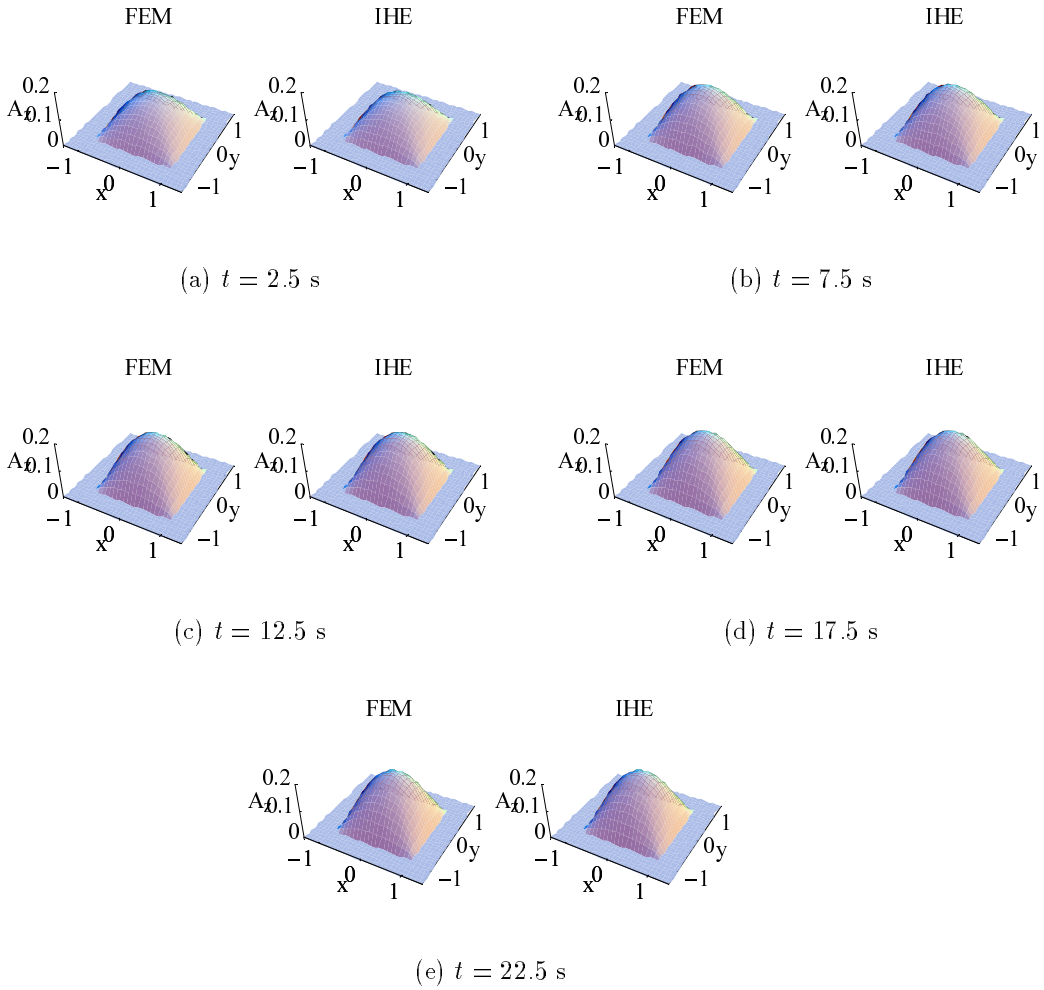

Fig. 2.41. Comparison between the finite element solutions and frames generated by means of the image Helmholtz equations.

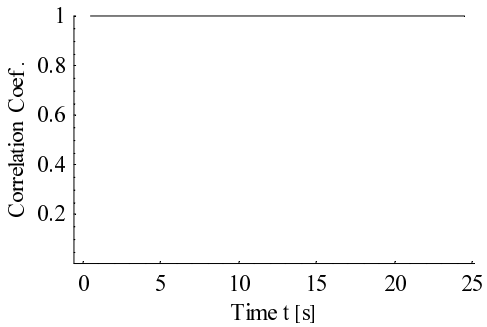

Fig. 2.42. Correlation coefficients between the solutions of finite elements and image Helmholtz equations.

2.4 Orthonormal Transformation

2.4.1 Modal-Wavelet Transform

The previous sections mainly describe the governing equations for static and dynamic images. The numerical calculation, obtained images, and correlation analysis verify successfully the nature of the image modeling based on the classical field theory. Based on the calculus, the field formulated by differential and integral equations can be divided into *modes* introducing spatial frequencies like wave propagation in waveguides. In this section, one of the orthonormal transformations, modal-wavelet transform (MWT), is derived from the image governing equations, described in the previous sections.

Assume any numerical data set to be the potential or source fields. A scalar field U caused by source density σ could be obtained by solving the differential equation in Eq.(2.26). The fundamental solution in Eq.(2.32) also gives a scalar field U from source density σ. Discretization of Eq.(2.26) and Eq.(2.32) by numerical methods derives the following system of equations:

$$L\mathbf{U} = \mathbf{F}, \tag{2.64}$$

and

$$G\mathbf{F} = \mathbf{U}, \tag{2.65}$$

where $\mathbf{F}$ and $\mathbf{U}$ represent the source density σ and the scalar field U in the vector forms, respectively. Moreover, L and G denote the coefficient matrices derived from the Laplacian operator in Eq.(2.26) and Green's function in Eq.(2.32), respectively. It is obvious that L and G^{-1} works the same function, yielding the source density distribution when they are applied to data sets. Solving Eq.(2.64) or Eq.(2.65) with the source density as vector $\mathbf{F}$ reproduces the original data set. As shown in Section 2.2, the image Poisson equation with relevant boundary conditions makes it possible to recover the original image from its source density. Therefore, it is possible to apply also to any kind of numerical data sets [19, 40].

As is well known, the matrices L in Eq.(2.64) and G in Eq.(2.65) derived by available discretizing methods, e.g., finite elements, etc., become the symmetrical as well as positive definite matrices. In case when the vector $\mathbf{U}$ has q elements, it is possible to obtain the characteristic values λ_i, $i = 1, 2, \cdots, q$, of the matrices L and G and their respective characteristic vectors $\mathbf{v}_i$, $i = 1, 2, \cdots, q$. The matrix composed of the characteristic vectors $\mathbf{v}_i$, $i = 1, 2, \cdots, q$, as its columns is called the modal matrix:

$$M_q = [\mathbf{v}_1, \mathbf{v}_2, \ldots, \mathbf{v}_q]. \tag{2.66}$$

Because of the orthogonality, it holds following relationship:

$$M_q {M_q}^T = I_q, \tag{2.67}$$

where the superscript T refers to a matrix transpose and I_q is a q by q identity matrix. The modal matrix derived from the coefficient matrix L or G has the same nature as those of the conventional discrete wavelet transform (DWT) matrices [41, 42].

Figure 2.43 illustrates the potential distributions given by the characteristic vectors constituting the matrix M_q in case of a two-dimensional data set model. Consider a two-dimensional rectangular region governed by Eq.(2.26), then a coefficient matrix L in Eq.(2.64) is constructed by the finite element schemes. The orthonormal matrix M_q derives from the characteristic vectors $\mathbf{v}_i$ constructed from the coefficient matrix L. The characteristic vectors illustrated in Fig.2.43 are linear independent, representing the respective modes in terms of the data set space [13]. A linear combination of the characteristic vectors $\mathbf{v}_i$ provides with the two-dimensional shapes as possible in a given data set, just corresponding to the multi-resolution orthonormal decomposition of conventional DWT. Hence, MWT proposed here is to employ the modal matrix as wavelet-like transform matrices to carry out orthonormal transformation.

2.4.2 Frequency Characteristics

The MWT matrices can be derived by various methods of discretizations. The MWT matrices introduced here are classified into two types. One is differential equation type assumed a subject data set to be a potential field. The other is integral expression type assumed a subject data set to be the field source distribution. At first, let us consider MWT derived from a differential equation. The simplest system matrix L can be obtained by one-dimensional Laplacian operation approximated by an equi-spaced three points finite difference. Namely, the matrix L in Eq.(2.64) is given by

$$\nabla^2 U = \frac{\partial^2 U}{\partial x^2} \simeq U_{x-1} - 2U_x + U_{x+1}, \quad x = 1, 2, \cdots, q, \tag{2.68}$$

where the distance of two adjacent data is assumed to be 1. Then, applying the Jacobi method yields a modal matrix M_q in Eq.(2.66) [43]. Therefore, the dimension of matrix M_q depends on the number of subdivision of Eq.(2.68). This means that it is possible to generate an optimal basis having the same data size as that of the subject. In the Laplace partial differential equation, two types of boundary conditions should be considered, i.e., the Dirichlet-

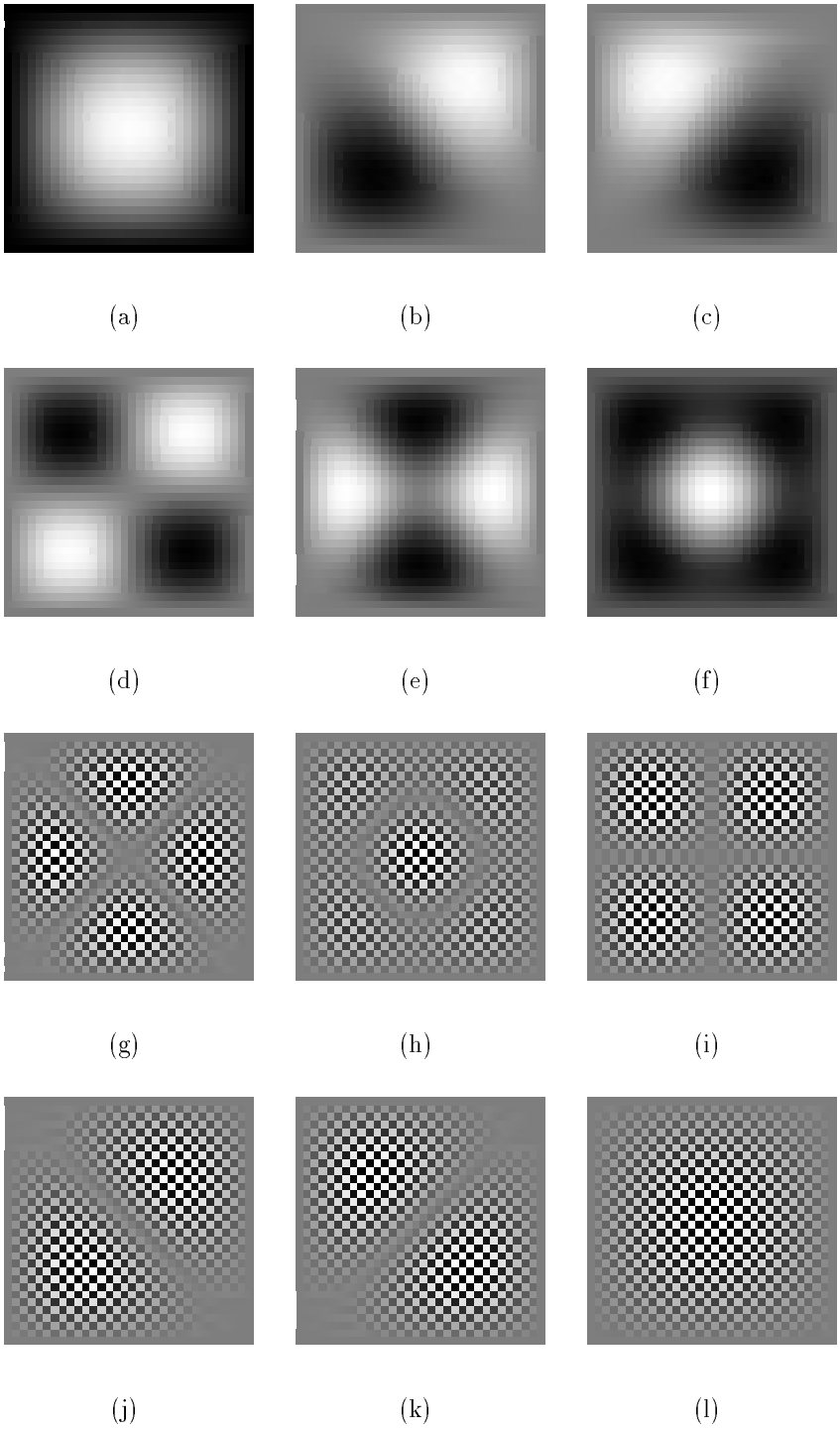

Fig. 2.43. Images represented by characteristic vectors [30 $\times$ 30 pixels (q = 900)] . (a)-(f) $\mathbf{v}_1$-$\mathbf{v}_6$ having the lower level of characteristic values. (g)-(l) $\mathbf{v}_{q-5}$-$\mathbf{v}_q$ having the higher level of characteristic values.

and Neumann- type boundary conditions. Figs.2.44(a) and 2.44(b) illustrate typical MWT matrices based on one-dimensional differential equation with the Dirichlet- or Neumann- type boundary condition. As shown in Figs. 2.45 and 2.46, the bases constrained by the Dirichlet- and Neumann- type boundary conditions become odd- and even- functions, respectively. The bases of MWT look like sinusoidal functions, however, the bases are not composed of the single frequency component. Moreover, the elements constituting the transform matrices never become the complex numbers like the Fourier transform, suggesting that effective multi-resolution analysis can be carried out.

Second, let us consider MWT derived from integral expression. A three-dimensional Green's function $g(r)$ in Eq.(2.32) is considered. However, the three-dimensional Green's function takes infinity when $g(0)$ due to integral kernel. In order to remove this difficulty the matrix G in Eq.(2.65) is given by assuming the minimum distance $r_{i,i} = 1$, thus,

$$g(r) \simeq \begin{cases} \frac{1}{r_{i,j}} & i \neq j \\ 1 & i = j \end{cases} \qquad i = 1, 2, \cdots, q, \quad j = 1, 2, \cdots, q, \tag{2.69}$$

where the subscripts i and j refer the source and reference points, respectively. Thereby, $r_{i,j}$ represents the distance between them. Since the system matrix derived from Eq.(2.69) becomes symmetrical, then the Jacobi method can be applied to obtain its modal matrix in much the same way as the MWT matrix based on differential equation. Figs. 2.44(c) and 2.47 show the MWT matrix and its bases. They have the similar patterns to that of the MWT matrix derived by imposing the Dirichlet boundary condition. Fig.2.48 shows a comparison between the MWT and Daubechies 2nd order wavelets along with the spectrum of Fig.2.12(b). In Fig.2.48, the left-bottom and right-top corners in each image correspond to the fundamental and the highest harmonics components, respectively. The transform matrix is non-orthogonal to the subject data set, then the major spectrum concentrates around the mother wavelets that are the spectra concentrated around the left-bottom corner of images in Fig.2.48. It is also the same nature as the cases when the higher order DWT are applied.

2.4.3 Image Compression

To compare with the conventional DWT, image compression is carried out. At first, apply MWT or DWT to Fig.2.12(b), then the spectrum are obtained. Second, neglecting higher level of obtained spectrum compresses the original data quantity. Finally, image recovery is performed by inverse MWT or DWT. To apply various compression ratios reveals the image recoverability of MWT or DWT.

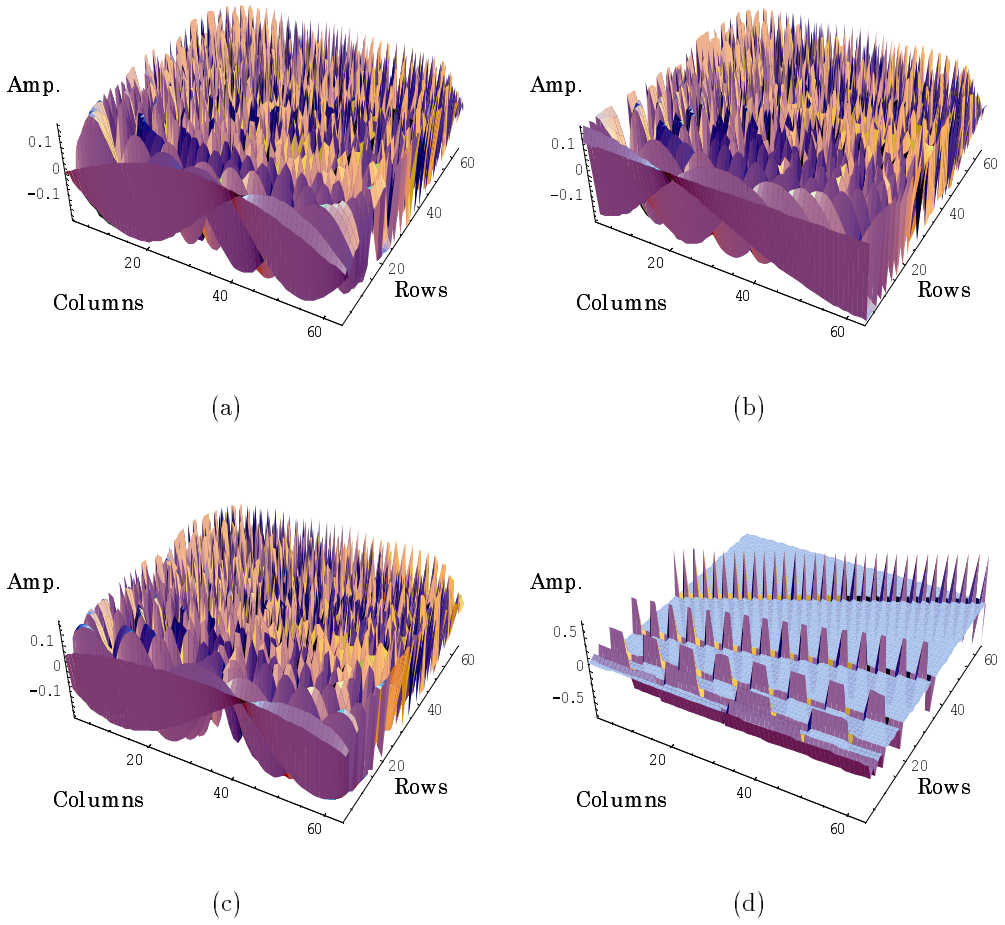

Fig. 2.44. Modal-wavelet transform matrices (64 × 64 elements). (a) Dirichlet-type boundary condition. (b) Neumann-type boundary condition. (c) Green's function-type. (d) Daubechies 2nd order.

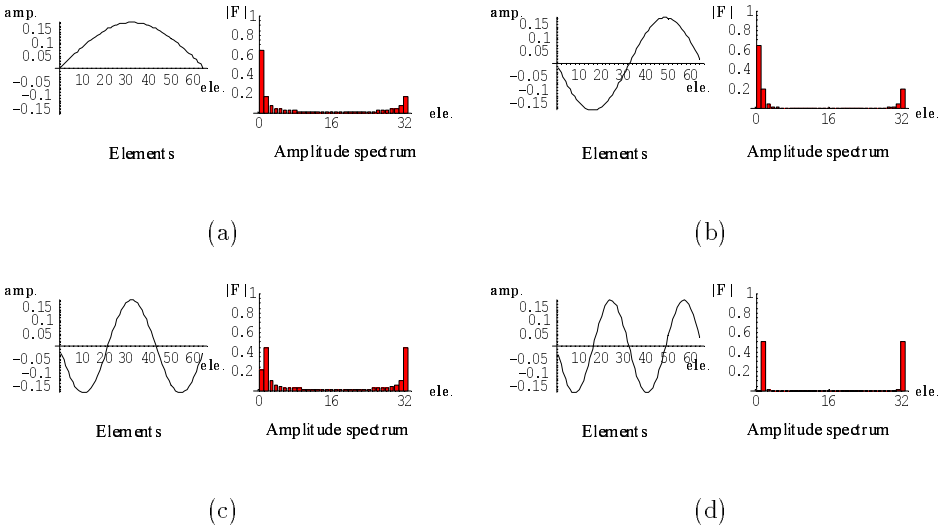

Fig. 2.45. Elements of the row vectors in the matrix shown in Fig.2.44(a) and their Fourier amplitude spectra. (a)-(d) The first-forth row vectors.

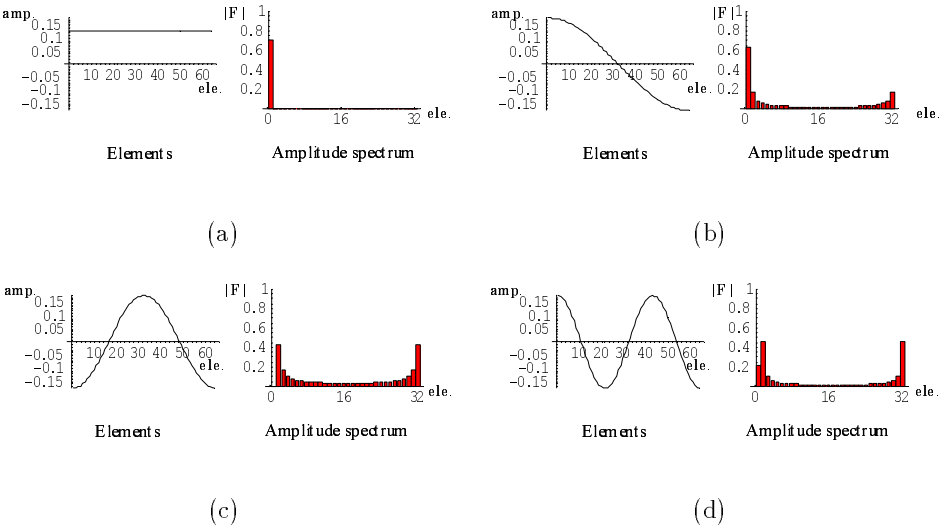

Fig. 2.46. Elements of the row vectors in the matrix shown in Fig.2.44(b) and their Fourier amplitude spectra. (a)-(d) The first-forth row vectors.

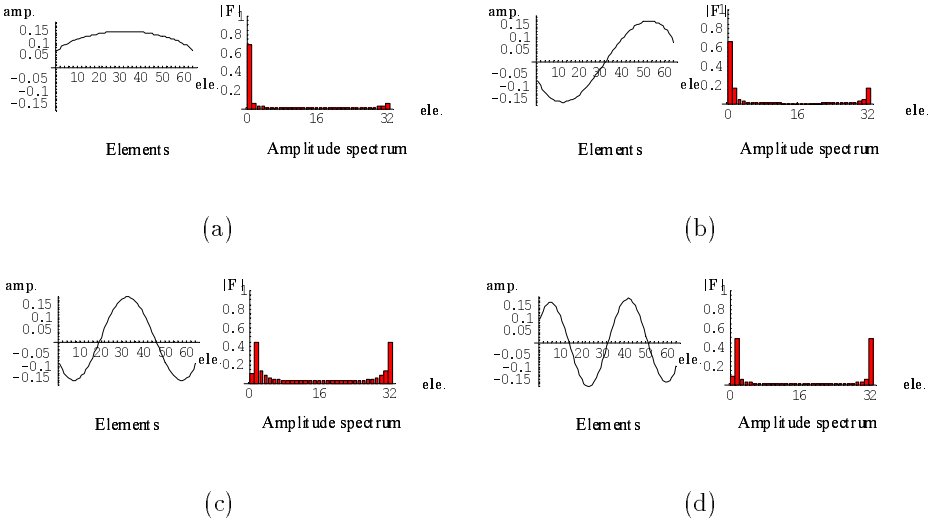

Fig. 2.47. Elements of the row vectors in the matrix shown in Fig.2.44(c) and their Fourier amplitude spectra. (a)-(d) The first-forth row vectors.

Figure 2.49 shows the comparison of image recovery from 25 % compressed image of Fig.2.12(b). MWT of Dirichlet-, Neumann- and Green's function- types compares with Daubechies 2nd order. Correlation coefficients of Figs. 2.49(a)-(d) are 0.889, 0.935, 0.930, and 0.887, respectively. The recovered image of the Daubechies 2nd order DWT looks like when the pixels are resampled, whereas the other results show smooth images according to the frequency characteristics of bases. However, the image recovered by the Dirichlet-type MWT, as shown in Fig.2.49(a), has stripe-like patterns along with the frame/edge of image and gives a relatively low correlation coefficient with the original image. The transform matrix of the Dirichlet-type MWT illustrated in Fig.2.44(a) has no constant term which gives an averaged image. This means that the spectrum must cover wide frequency ranges to represent the avaraged image. It is confirmed that the spectrum shown in Fig.2.48(a) spreads over higer frequency levels. Therefore, the Dirichlet-type MWT efficiently divides the subject data set without constant term into the orthogonal data sets. MWT of the Neumann- and Green's function-types has the functions covering constant terms as the first level of bases as shown in Figs. 2.46(a) and 2.47(a), meaning that the avaraged images can be accurately represented by several spectra. Therefore, Figs. 2.48(b) and 2.48(c) have higher density of the spectra around the lower frequency range, resulting in the high correlation coefficients of the recovered images.

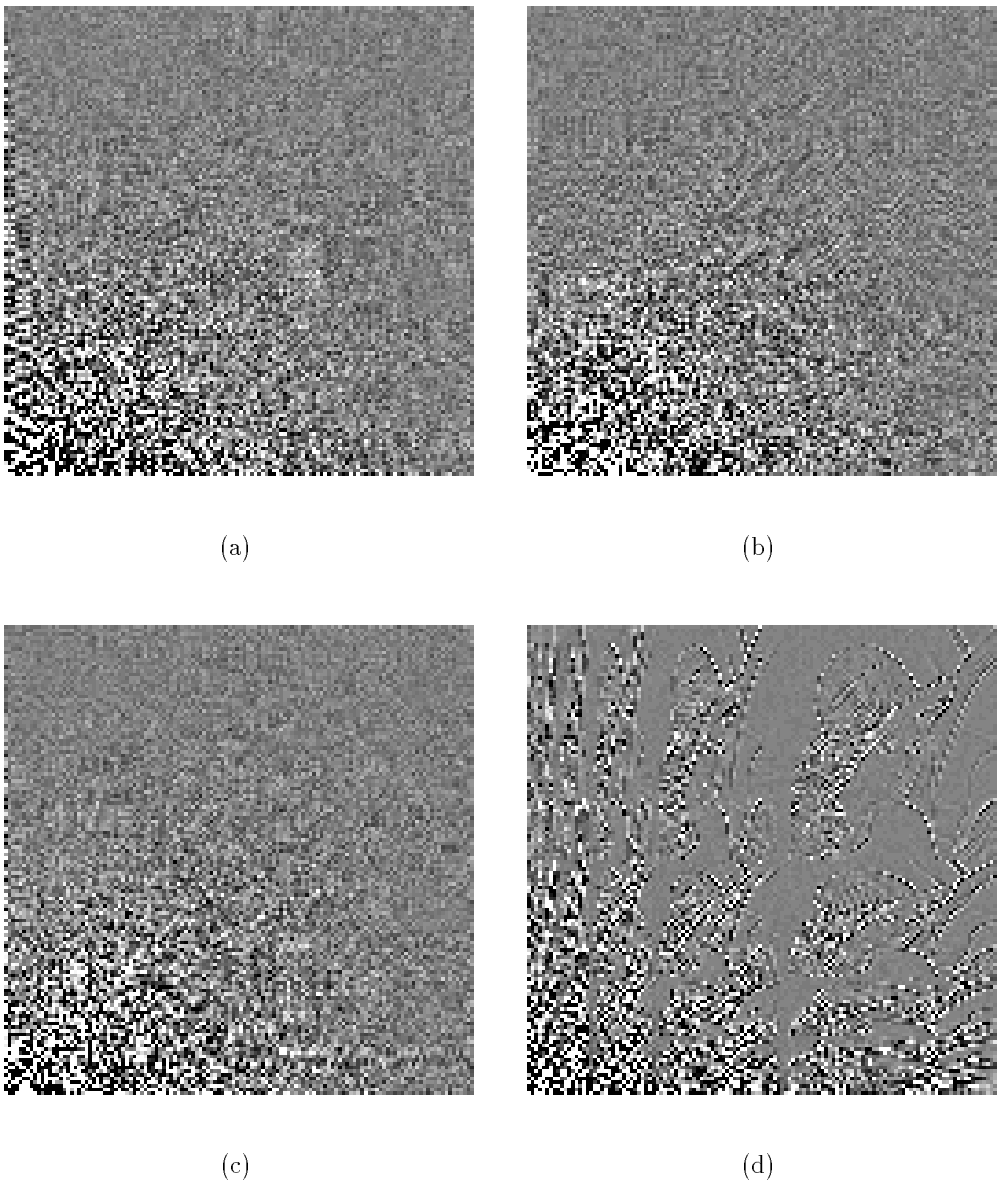

(a) (b)

(c) (d)

Fig. 2.48. Wavelet spectra of Fig.2.12(b) (128 $\times$ 128 pixels). (a) MWT with Dirichlet boundary condition. (b) MWT with Neumann boundary condition. (c) MWT with Green's function. (d) Daubechies 2nd order.

On the other hand, the recovered images of MWT are smooth like when applying a higher order of DWT matrix. The correlation coefficients versus compressed ratios of the MWT and DWT in Fig.2.50 suggest a fairly good recoverability of MWT. Although higher order DWT is applied, for example, Coifman's 30th order yields the low accuracy of recoverbility in less than the compression ratio of 5 %. This is because DWT strictly classifies orthogonal data sets as wavelet levels. It should be noted that MWT is capable of higher recoverability when having poor data quantity since the transform matrix of MWT only depends on the subject data length. Thus, efficient data compression can be performed by MWT. Moreover, MWT has infinite number of combinations to derive the transform matrices and bases. Therefore, it is possible for users to derive optimal bases and realize bases having arbitrary characteristics based on the idea of the classical field theory.

2.5 Summary

This chapter has described the theoretical background of the image modeling based on the classical field theory. Assume a pixel representing digital images to be a kind of field potentials, then the image handling methodologies and its mathematical formulation can be achieved.

At first, scalar and vector potentials represent monochrome and color pixels, respectively. Introducing Coulomb gauge to color images reduces into considering three independent monochrome images.

Second, the image vector operations, i.e., the gradient, divergence, and rotation, are introduced by the finite difference approximation, leading to the image governing equations and the solution strategies for them. Poisson and Helmholtz types of partial differential equations are considered as the image governing equations of static and dynamic images, respectively.

Third, the image govering equations and their solution are described. The image Poisson equation, which is the governing equation for static image, is demonstrated by finite differences, finite elements, and Green's function schemes. It shows that the static images can be generated by the solution of the image Poisson equation with image source densities. How to set the boundary condition is of importance to recover images correctly. Rearranging image source density derived from the Laplacian of target image has versatile capability to process the image. On the other hand, the image Helmholtz equation, which is the governing equation for dynamic image, generates the animation frame at arbitrary time. Modal analysis of the image Helmholtz equation derives a general solution. It reveals that two frames of animation and a state transition matrix are essentially required to generate animations.

(a) (b)

(c) (d)

Fig. 2.49. Comparison of image recovery from the 25 % compressed image of Fig.2.12(b) (128 $\times$ 128 elements). (a) Dirichlet-type boundary condition. (b) Neumann-type boundary condition. (c) Green's function-type. (d) Daubechies 2nd order.

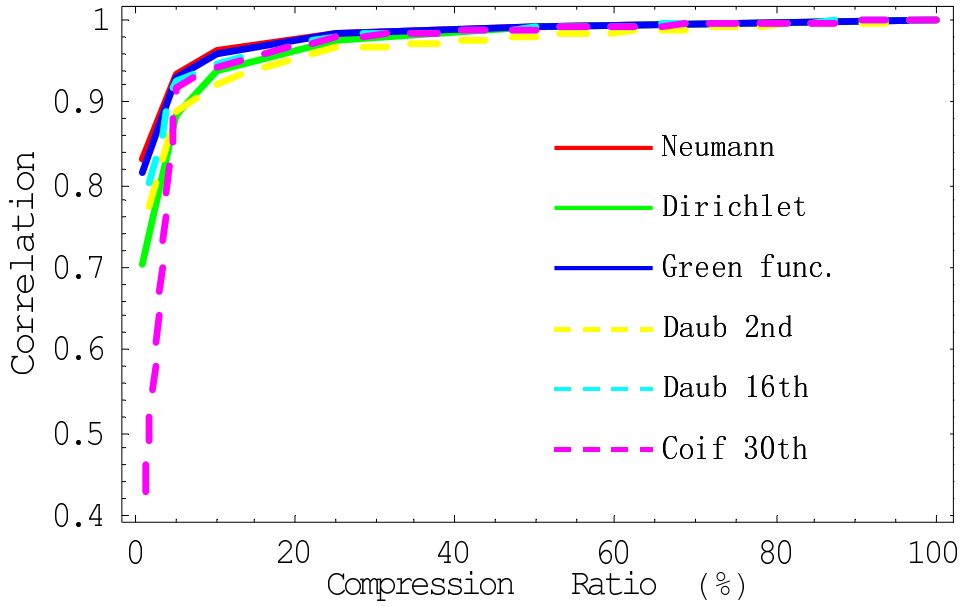

Fig. 2.50. Correlation coefficients vs. compressed ratios of the image data Fig.2.12(b). Neumann-, Dirichlet-, and Green's function- types of MWT and Daubechies 2nd, Daubechies 16th, and Coifman 30th order DWT are evaluated.

In order to overcome this difficulty, the method of equivalent characteristic value is proposed to determine the state transition matrix from the given three frames of animation. The time-discretized frames of animation can be converted to continuous functions by means of the equivalent characteristic values.

Finally, modal-wavelet transform is proposed as a novel orthonormal transformation for image data representation. Modal analysis of the discretized image governing equations leads to orthonormal basis functions having the nature of both wavelet and Fourier transforms. Image data compression performs fairly high efficiency comparing with those of the conventional discrete wavelets.

This image modeling is just corresponding to modeling in physical fields. Thus, the image analysis based on this image modeling can be carried in a quite efficient manner when applying to the physical systems.

CHAPTER 3

Applications in Visualized Fields

3.1 Vector Analysis in Static Images

3.1.1 Sketch-like Image Generation

One of the applications using the image vector operations is to draw sketch-like images by computers. The image vector operations in Section 2.1 are capable of generating the sketch-like images by calculating vector magnitude at each position [18, 24]. When a monochrome image is regarded as a scalar field U, then the image gradient operation gives vector field. On the other hand, the image rotation operation can be applied when a monochrome image is assumed to be one component of vector potential field.

Figure 3.1 illustrates the gradient and the rotation of the monochrome image shown in Fig.2.12(b). The arrows in Fig.3.1(a) point to the point across the contours supposed on the image. In case of Fig.3.1(b), the arrows tend to trace along with the contour lines. The vector magnitudes of the obtained vectorized fields derive the sketch-like images.

Figure 3.2 shows the results of sketch generation. After taking the square roots of the image vectors, the contrast of image is reversed. Since the divergent and rotational fields are orthogonal each other, then the similar sketch-like images can be generated. It reveals that the image vector operations accomplish automatic sketch generation by using computers.

When this methodology is applied to a color image, it is possible to generate the colored sketch-like image. Fig.3.3 shows the result of sketch generation in case of a color image. According to the image modeling of this study, a color image are reduced into three independent monochrome images. Sketching for Fig.3.3 is carried out in each of RGB components independently, after that they are synthesized to display.

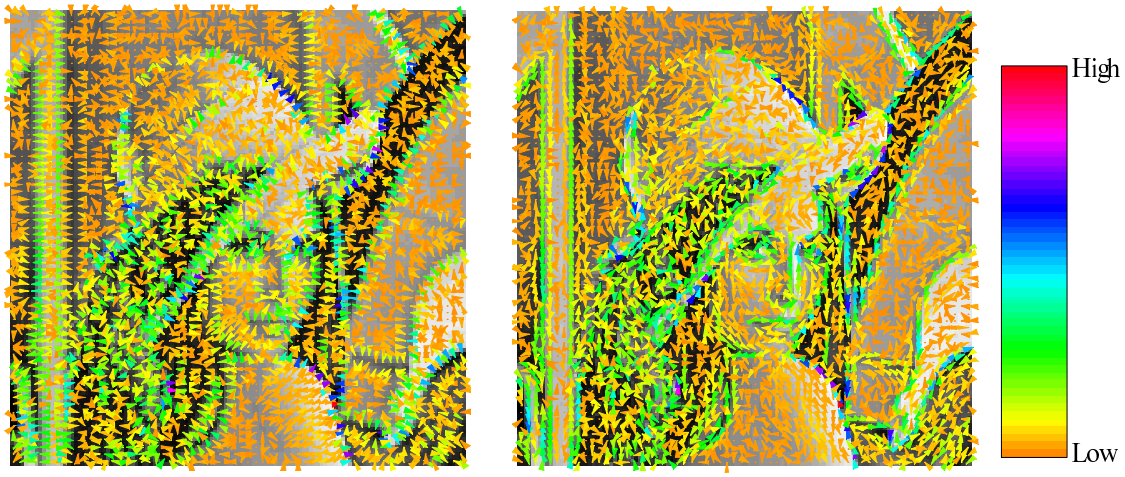

(a) Gradient (b) Rotation

Fig. 3.1. Image vectors of Fig.2.12(b) to draw sketch-like images (128 × 128 pixels).

(a) Gradient (b) Rotation

Fig. 3.2. Sketch-like images obtained by the image vectors in Fig.3.1 (128 × 128 pixels).

(a) Color image (b) Color sketch-like image

Fig. 3.3. Colored sketch-like images (128 × 128 pixels).

3.1.2 Flaw Shape Classification

The image vector operations provide an effective methodology in flaw inspection. In the large-scale metal structures, especially in case of nuclear power stations, non-destructive inspection is of paramount importance. The major way to carry out is visual testing (VT) which is just to be seen by human eyes. Due to the radio-activated area, industrial robots carrying CCD cameras play role in helping prompt inspections. Therefore, VT needs effective systems in order to classify the conditions on target surfaces.

An example of the flaw classification on weld parts is demonstrated here. There are two typical flaws to be classified [23]. One is circular type defects originated from the quality of welding. The other is line type defects concerning with cracks after assembling. Figs. 3.4 and 3.5 show the CCD images of the circular and line type defects, respectively. The right columns of these figures illustrate the rotational vector operation of the CCD images. The image vectors emphasize the contour lines concerning with the major defects.

To classify the type of flaws, the angles of image vectors are investigated by weighted histogram. Calculating both angles and magnitudes of the image vectors gives the weighted histograms shown in Figs. 3.6 and 3.7. In these histograms, the horizontal- and vertical- axes correspond to the vector

angles and total of vector magnitudes, respectively. The weighted histogram emphasizes the angle of vectors having high intensity in magnitude. The line type defects are characterized by peak distributions around 90 degrees indicating vertical direction. On the other hand, the distribution of circular type defects covers wider range than that of the line type defects. It reveals that the shape of flaws can be classified by the distribution of vector directions. It should be noted that the peaks observed at ± 45 and ± 135 degrees in any type of defects. This is because the nature of centeral finite difference method in Eq.(2.15) to generate the image vectors.

3.1.3 Summary

This section has demonstrated a couple of applications employing the image vector operations.

One is to generate sketch-like images. Applying the image vector operations to the images derives a kind of contour lines from differentiation. Magnitudes, as well as directions of the image vectors make it possible to generate the sketch-like images. Moreover, the colored sketch image can be generated from independently evaluated sketches in each of RGB components. The results of sketch image generation suggest that the image vector operations may work out some of the human-oriented tasks.

Another application is concerned with non-destructive testing. Applying the image vector operations to the images given by VT makes it possible to classify the shapes of surface flaws on the welded parts of structures. Orientations, as well as magnitudes of the image vectors classifies tested images into the line and circle types of flaws.

The image vector operations of visualized fields have a variety of applications to solve the problems associated with characteristic of spatial distribution.

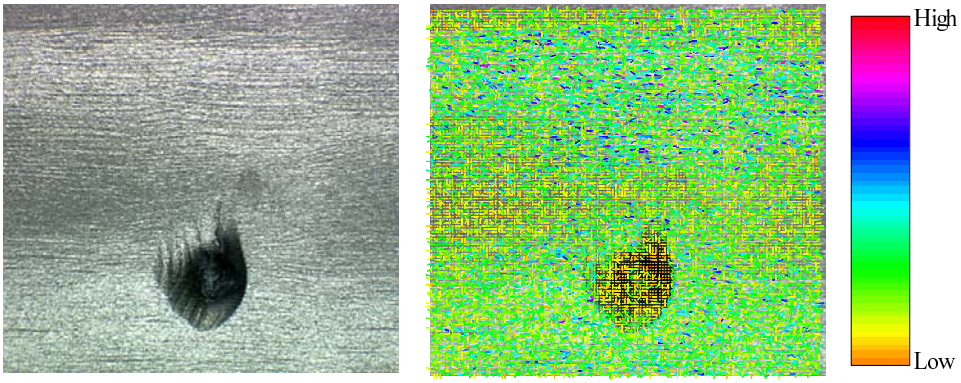

(a) No.1

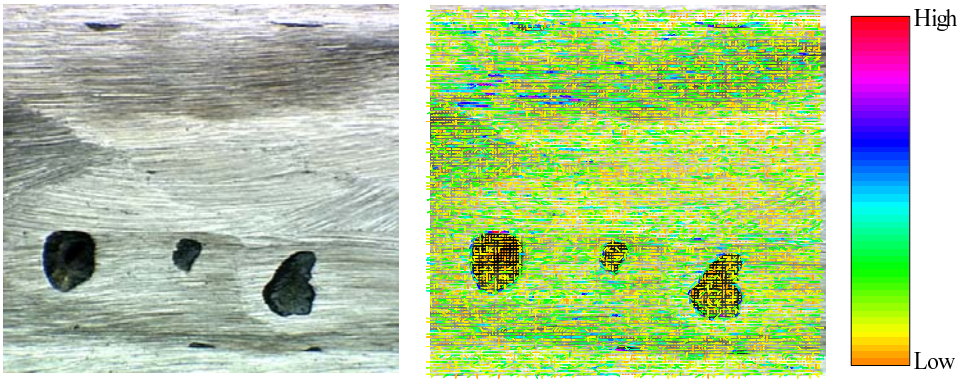

(b) No.2

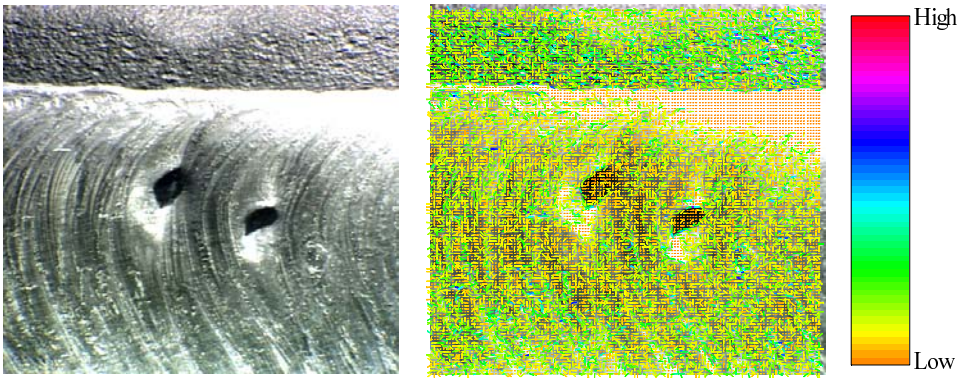

(c) No.3

Fig. 3.4. Circular type defects on weld parts and rotational image vectors (480 × 512 pixels).

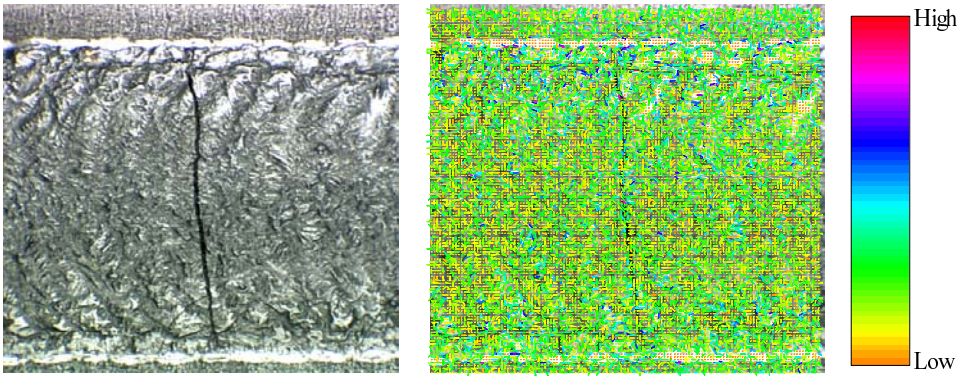

(a) No.1

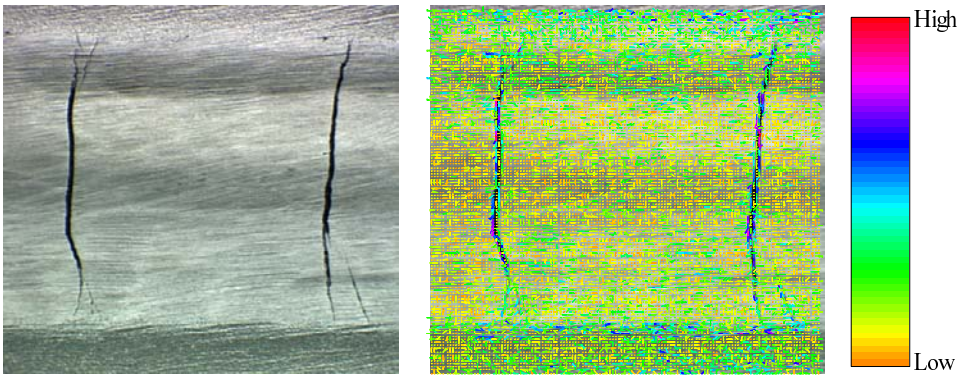

(b) No.2

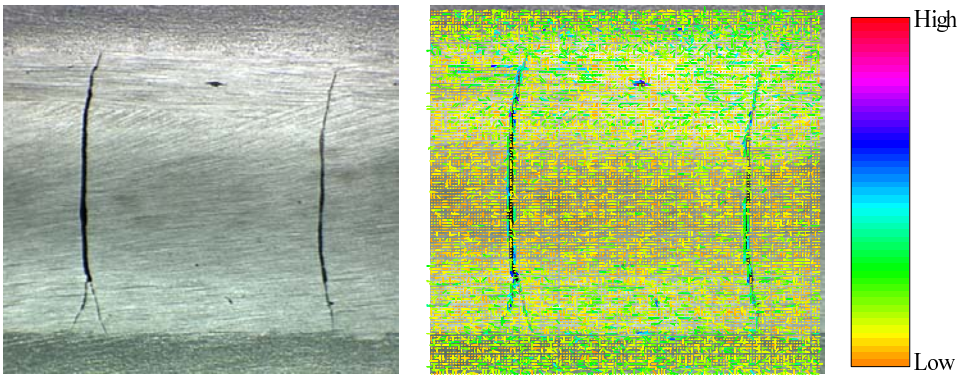

(c) No.3

Fig. 3.5. Line type defects on weld parts and rotational image vectors (480 $\times$ 512 pixels).

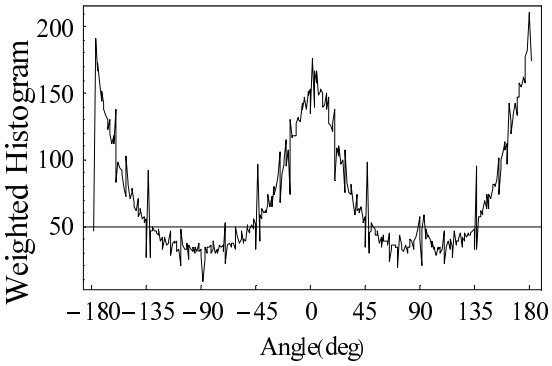

(a) No.1

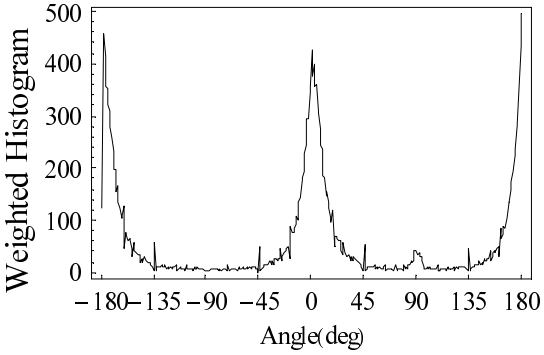

(b) No.2

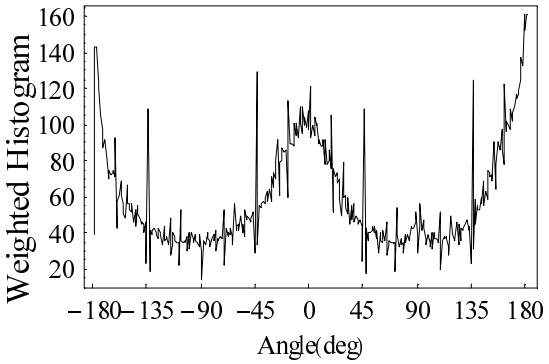

(c) No.3

Fig. 3.6. Weighted histograms of the rotational vector angles in case of circular type defects.

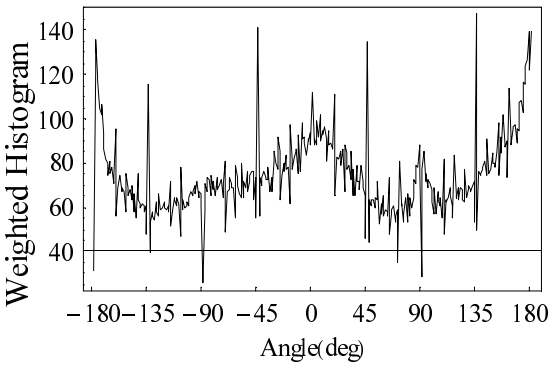

(a) No.1

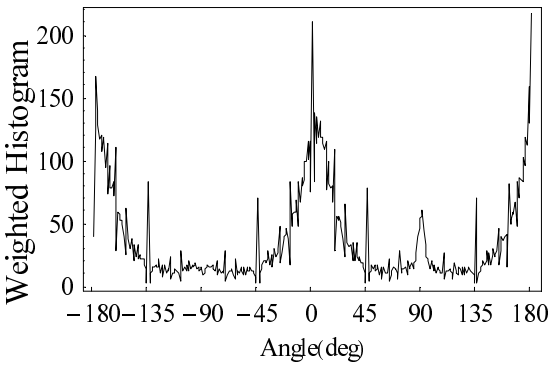

(b) No.2

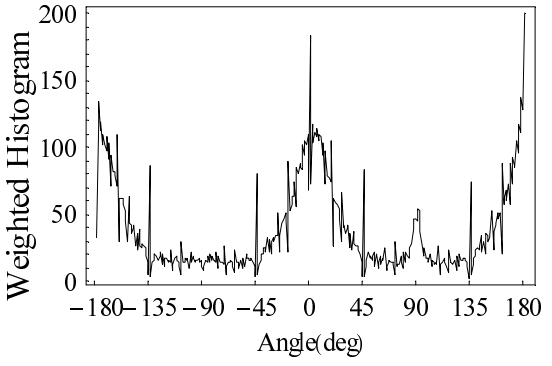

(c) No.3

Fig. 3.7. Weighted histograms of the rotational vector angles in case of line type defects.

3.2 Magnetic Field Imaging

3.2.1 Field Visualization by Color Image

This section proposes a novel methodology to visualize the electromagnetic vector fields by means of the image Poisson equations.

The electromagnetic field data visualizing precise distribution essentially requires enormous data quantity, because the electromagnetic field spreads into the space around electronic devices with infinitely high-resolution. In order to handle such electromagnetic field data efficiently, two approaches may be considered. One is an inverse solution approach, which recovers electromagnetic field distribution from its electromagnetic field source evaluated as a solution of inverse problem. The other one is to employ a digital image handling technique. As described in Section 2.2, the image Poisson equation is possible to generate the high-resolution image from the image of low resolution source density, Thereby, the spatial resolution of the measured data can be improved by solving for the image Poisson equation.

In order to apply this methodology, a three-dimensional vector field on a plane like in Fig.3.8(a) is represented by a color image as demonstrated in Fig.3.8. Namely, the x-, y-, and z- components of vector fields in Cartesian coordinate system are projected onto the red, green, and blue (RGB) components of the color image, respectively. For example, the projection of the vector components shown in Fig.3.8(b) to the RGB components of color image visualizes the vector distribution by the color image. Conversely, the color image in Fig.3.8(c) is represented by the vector distribution. The measured magnetic field always shows poor resolution like in Fig.3.8(c), however, applying the image Poisson equation improves the resolution of image from source density approach.

Figure 3.9 shows the practically measured magnetic field on a DC/DC converter utilizing a film type transformer [44–46]. Magnetic vector field is measured on the transformer by solenoid coil in each of directional components. The number of measured points is 32 by 32 in x- and y- directions with measuring interval of 5 mm. The measured field is imaged in much the same way as that in Fig.3.8.

3.2.2 Spatial Resolution Refinement

To refine the measured data, the image resolution enrichment of the image Poisson equation is applied to the colored image in Fig.3.8.

At first, the Laplacian described in Section 2.1 is applied to each of the RGB components of color images in order to obtain the image source densi-

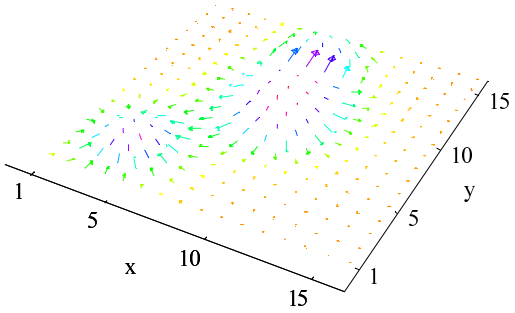

(a) A vector field

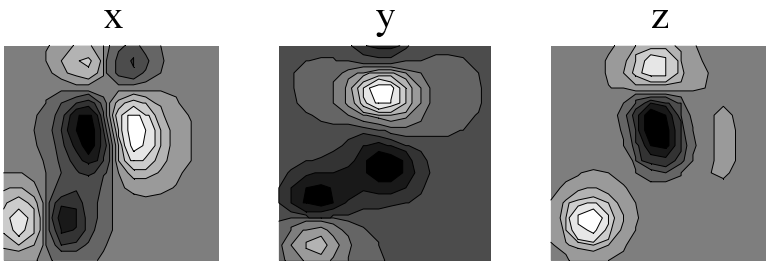

(b) $x, y,$ and$z$ components of the vector field

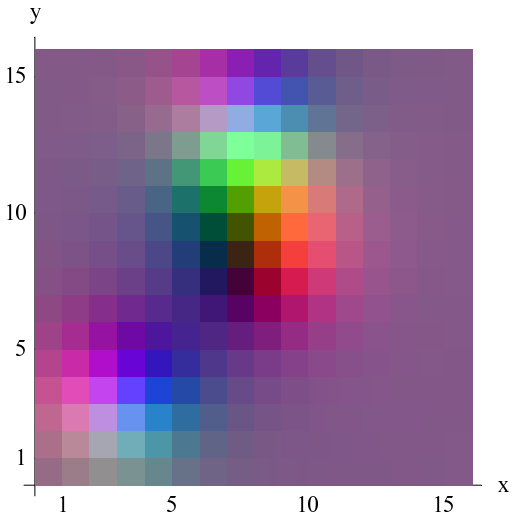

(c) Imaged by color image (16×16 pixels)

Fig. 3.8. Vector field imaging by color image.

(a) DC/DC converter utilizing a film type transformer

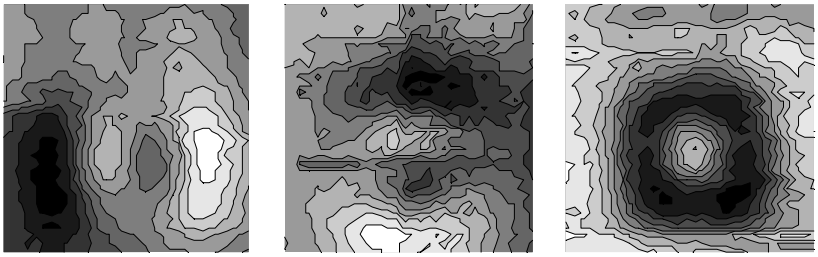

(b) x, y, and z components of the measured magnetic field

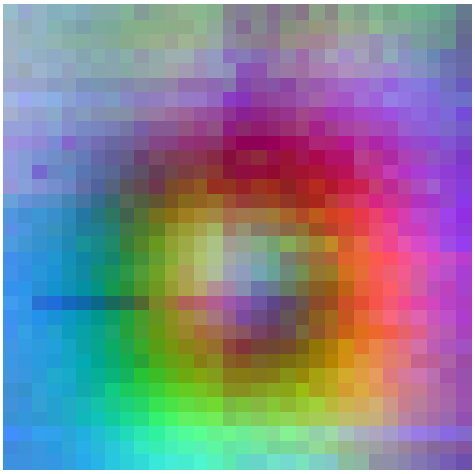

(c) Measured magnetic field and imaged by color image (32×32 pixels)

Fig. 3.9. Magnetic field distribution on a DC/DC converter.

ties. Second, solving for three image Poisson equations, i.e., in each of the RGB components, recovers the RGB components of the color image. Finally, synthesizing the RGB components gives the recovered color image to display. When the same number of nodal points as that in the Laplacian operation is used to solve the image Poisson equations, the original color image can be obtained with quite high accuracy. When the number of nodal points is changed to solve the image Poisson equations, it is possible to change the resolution of the image.

In order to check up validity of this methodology, accuracy of refinement is evaluated with discarded color images of the measured magnetic field. In other word, the pixels in Fig.3.9(c) are simply resampled to make low resolution images. Fig.3.10 shows the low resolution color images generated from Fig.3.9(c). Carry out the Laplacian of each image in Fig.3.10, then the low resolution image source densities are obtained. Employing the fine mesh system corresponding to 32 $\times$ 32 pixels yields the recovered images with 32 $\times$ 32 pixels. Fig.3.11 shows the results of image enriched resolution for the measured magnetic field. Moreover, the recovered vector fields corresponding to Fig.3.11 are illustrated in Fig.3.12. The nine-point finite difference formula of the Laplacian is employed here. The correlation coefficients between Fig.3.9(c) and Figs. 3.11(a)-(d) are 0.930, 0.901, 0.822, and 0.503, respectively. Fig.3.13 summarizes the correlation coefficients versus the number of pixels. Although 25 % of the original number of pixels, image recovery with the image Poisson equation achieves over 0.9 of correlation coefficient. It is remarkable that the correlation coefficient over 0.5 can be obtained from only 1.56 % of the original number of pixels. This is because the image modeling by the classical field theory just corresponds to the same mathematical background as electromagnetic field. An optimal interpolation can be realized by solving for the image Poisson equation.

3.2.3 Summary

This section demonstrates a methodology of measured data improvement by means of the image Poisson equation.

The source representation for the imaged magnetic field is capable of improving the resolution of the original field. Setting the required nodal points to the source density enables to change the resolution of image freely.

The methodology is verified by comparing with the practically measured field. As a result, 25 % of the original number of pixels is possible to recover the original resolution of field having 0.9 in correlation coefficient. It is shown that the image modeling by the classical field theory is one of the quite efficient image handling approaches in this kind of visualized physics.

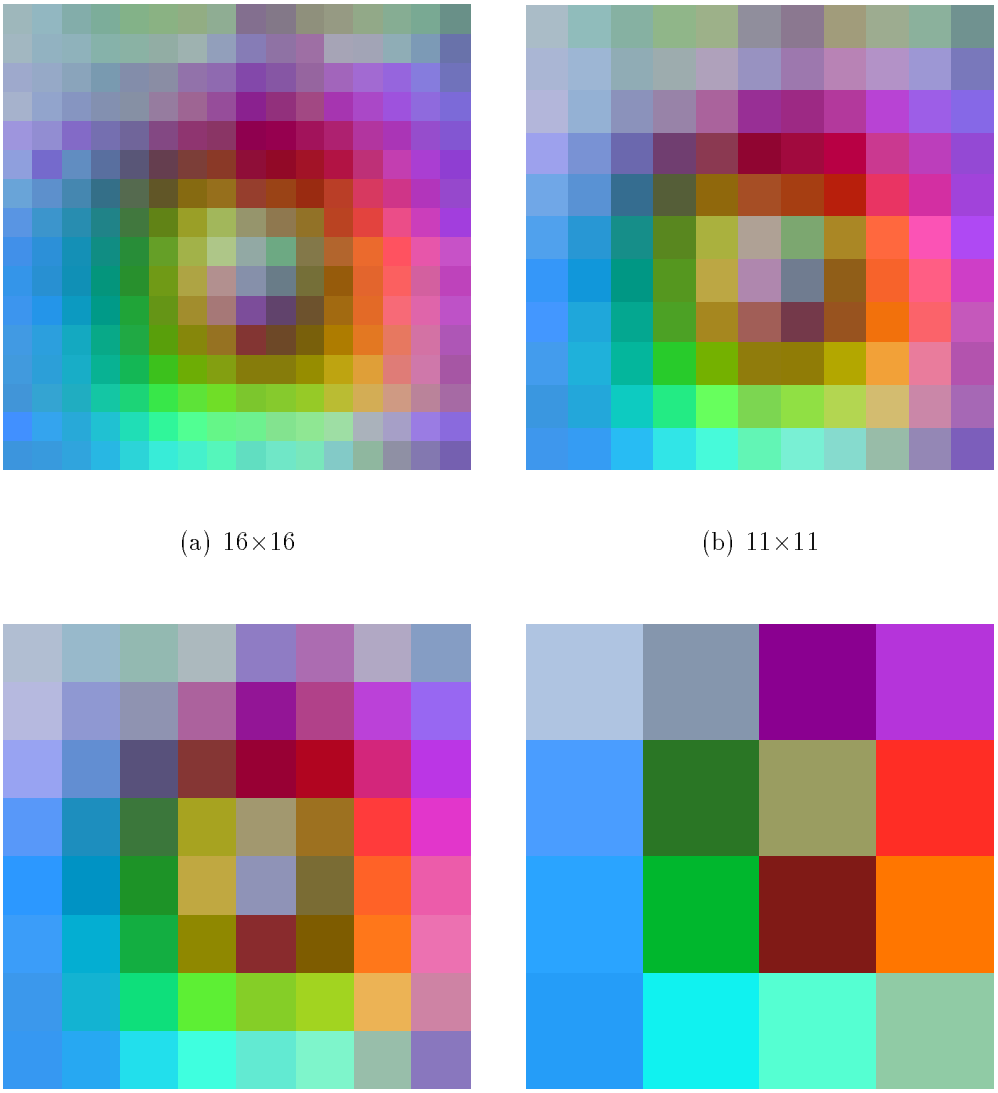

(a) 16×16 (b) 11×11

(c) 8×8 (d) 4×4

Fig. 3.10. Imaged magnetic fields with low resolutions.

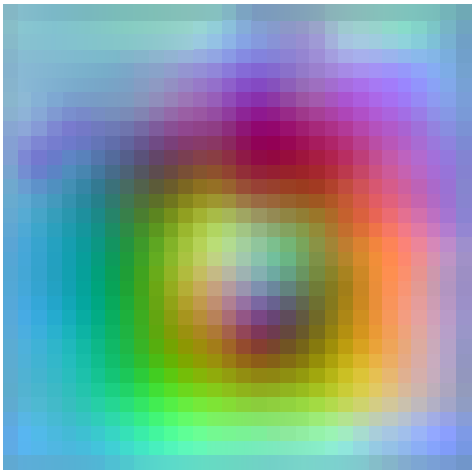

(a) From 16×16 to 32×32

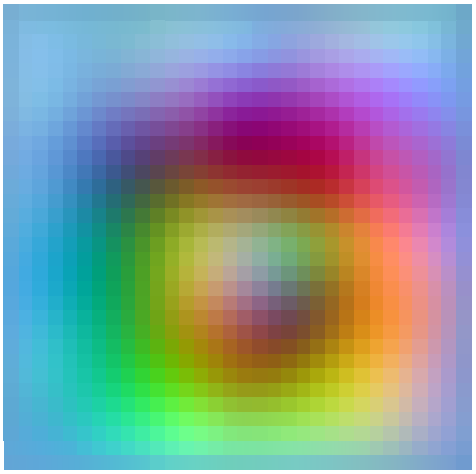

(b) From 11×11 to 32×32

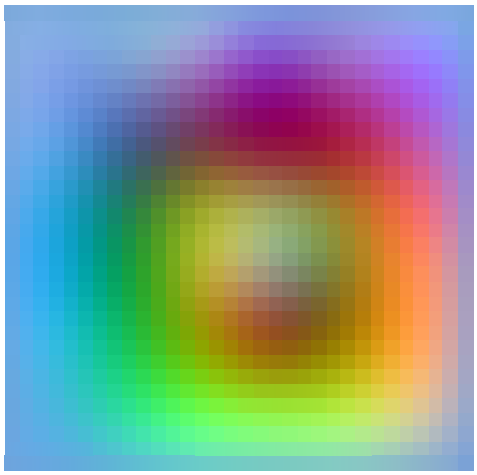

(c) From 8×8 to 32×32

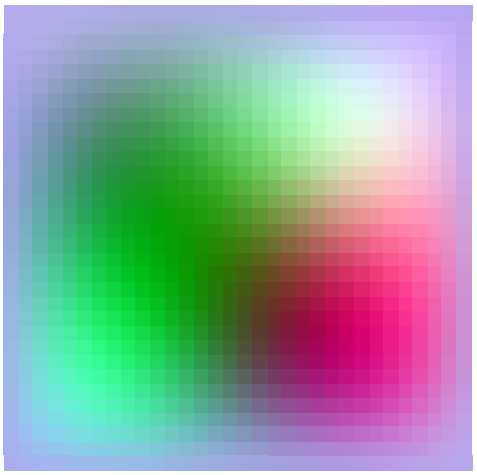

(d) From 4×4 to 32×32

Fig. 3.11. Magnetic fields enriched resolution from the imaged magnetic fields with low resolutions in Fig.3.10.

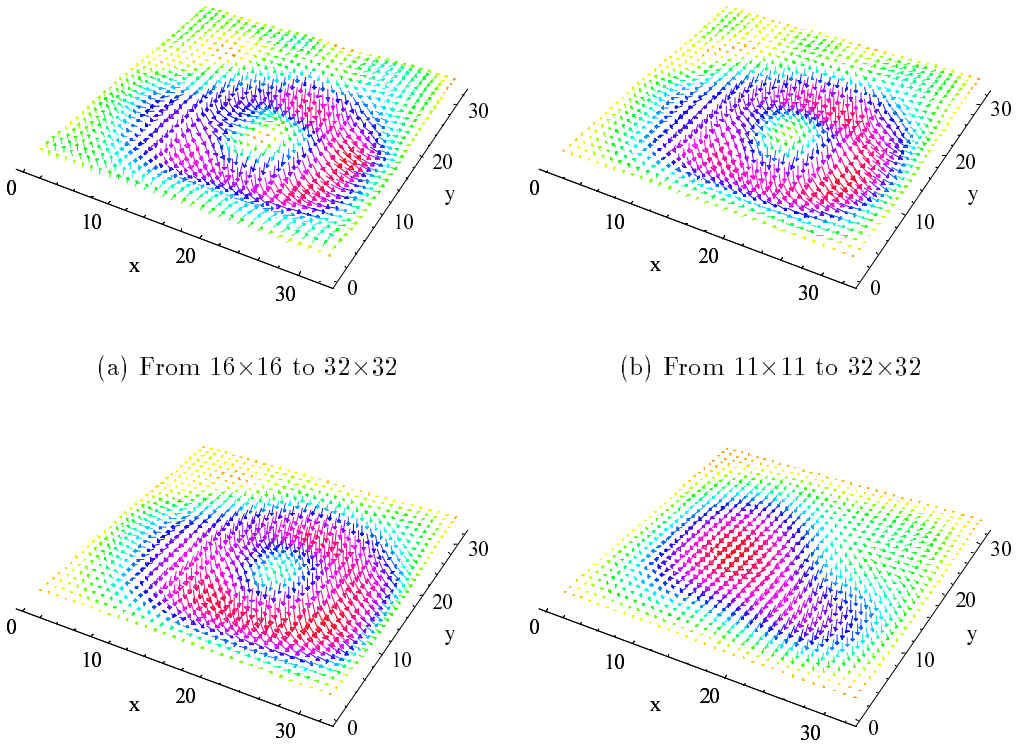

(a) From 16×16 to 32×32

(b) From 11×11 to 32×32

(c) From 8×8 to 32×32

(d) From 4×4 to 32×32

Fig. 3.12. Recovered magnetic vector fields.

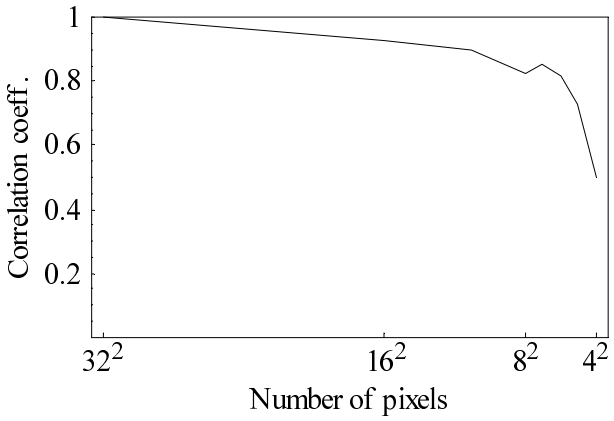

Fig. 3.13. Correlation coefficients between the imaged original field in Fig.3.9(c) and recovered fields.

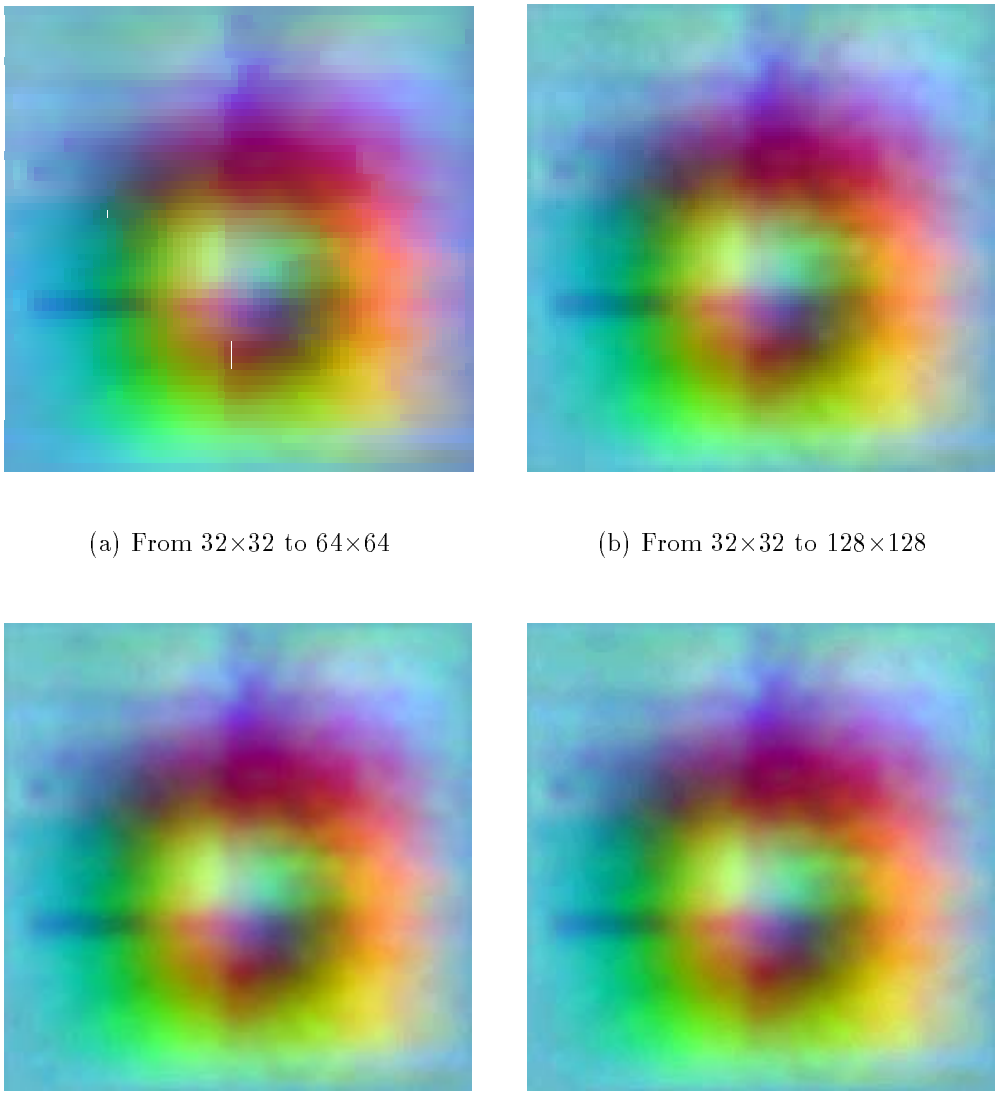

(a) From 32×32 to 64×64

(b) From 32×32 to 128×128

(c) From 32×32 to 192×192

(d) From 32×32 to 256×256

Fig. 3.14. High resolution magnetic field generation from the measured magnetic field shown in Fig.3.9(c).

3.3 Magnetic Domain Dynamics

3.3.1 SEM Images of GO Steel Sheet

As an application of the image Helmholtz equation, this section deals with magnetic domain images (Fig.3.15) obtained by a scanning electron microscope (SEM) to analyze magnetic domain dynamics and visualize iron loss. The understanding of magnetic domain behaviors such as domain structure and boundary displacement leads to the quality evaluation of magnetic materials [47]. Since the domain observation visualizes magnetized states as the contrast of images, then investigation on microscopy-based measurement such as Kerr effect has been spurred [48, 49]. Heretofore, experts could only accomplish iron loss evaluation from the domain observation based on elaborate analyses. This background stimulates the image Helmholtz equation to provide an effective means to visualize and to quantify the local iron loss as well as the domain motion dynamics [50–53].

Apply the image Helmholtz equation to the observed domain images, then iron loss distribution is visualized from a series of distinct magnetized domain images. The state transition matrix by means of equivalent characteristic values represents the characteristic values of physical dynamic system visualized by finite number of images as an animation. In this magnetic domain image analysis, assuming the averaged contrast of domain image as an entire flux density leads that the characteristics of domain motion deduces from the state transition matrix.

Fig.3.15 shows the SEM magnetic domain images of a grain-oriented electrical steel under the distinct magnetized states [54]. The specimen is the ORIENTCORE HI-B (Nippon Steel Corporation product) without surface coating and its thickness is 0.23 mm. Fig.3.16 shows the SEM device used to the magnetic domain observation. It employs the backscattered electron (Type-II) to image the patterns of magnetization [47]. The observation is carried out at 160-kV acceleration voltage. At this condition, the domain patterns about 10 μm depth from the surface of specimen could be visualized as shown in Fig.3.15 [55]. The external field is applied to the rolling direction with sloping excitation. Fig.3.16(b) shows the sample holder in the SEM device. To produce the external field, the sample holder has a magnetic yoke with the exciting coils under the specimen as illustrated in Fig.3.16(c). The conditions of domain image measurement used here are listed in Table 3.1.

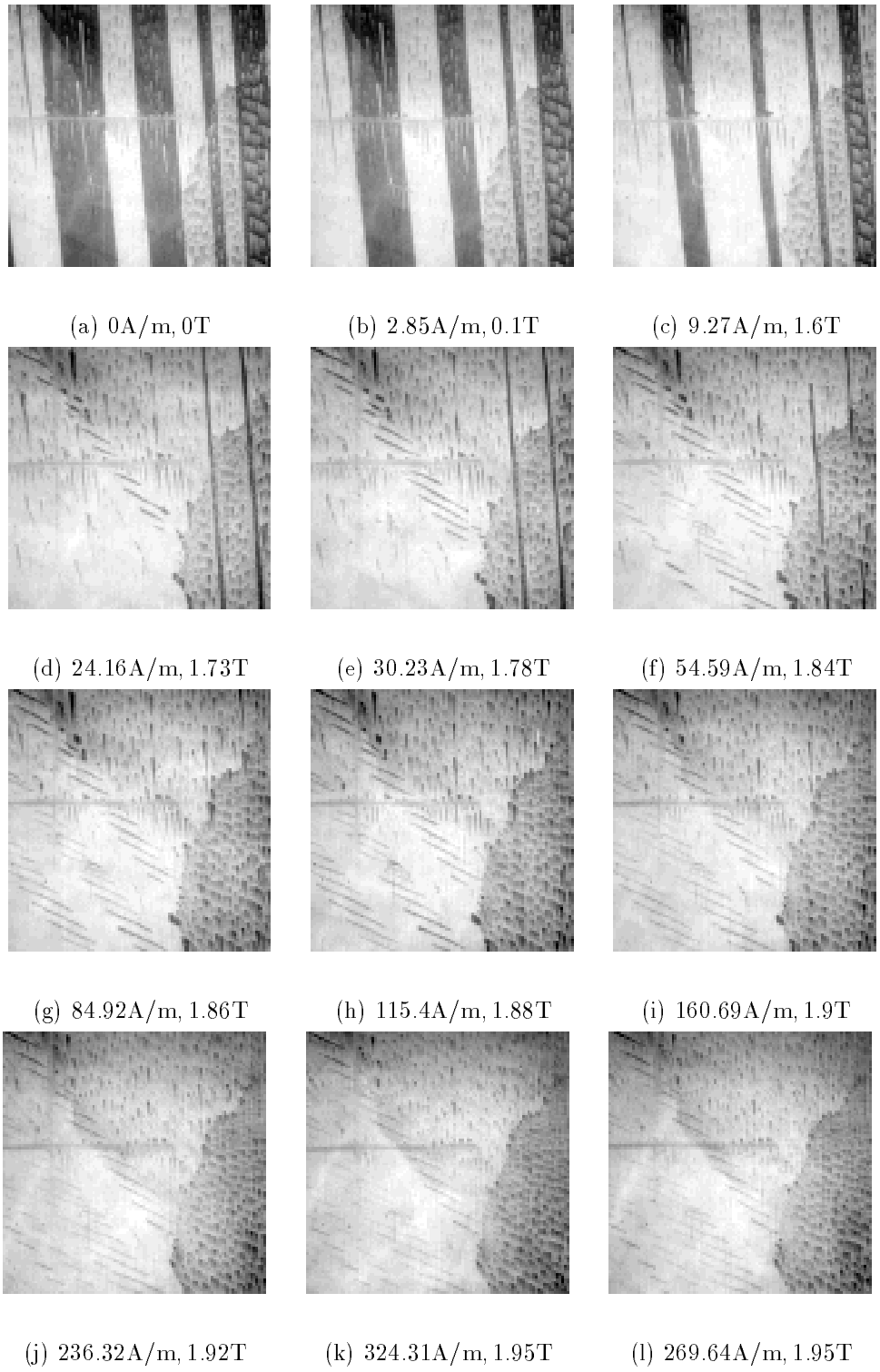

(a) 0A/m, 0T (b) 2.85A/m, 0.1T (c) 9.27A/m, 1.6T

(d) 24.16A/m, 1.73T (e) 30.23A/m, 1.78T (f) 54.59A/m, 1.84T

(g) 84.92A/m, 1.86T (h) 115.4A/m, 1.88T (i) 160.69A/m, 1.9T

(j) 236.32A/m, 1.92T (k) 324.31A/m, 1.95T (l) 269.64A/m, 1.95T

Fig. 3.15. Magnetic domain images of a grain-oriented electrical steel observed by high-voltage SEM (100 $\times$100 pixels, 0.1 mm/pixel). The vertical direction is the rolling direction and applied external field axis.

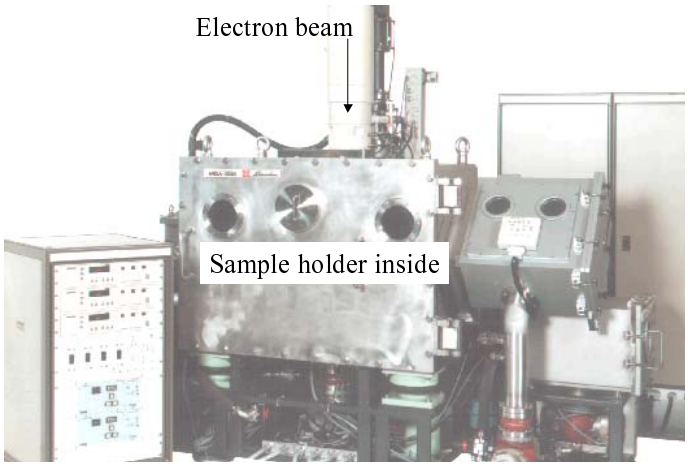

(a) Exterior of SEM device

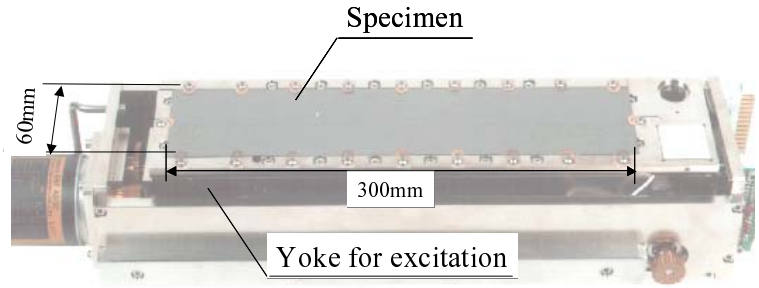

(b) Sample holder

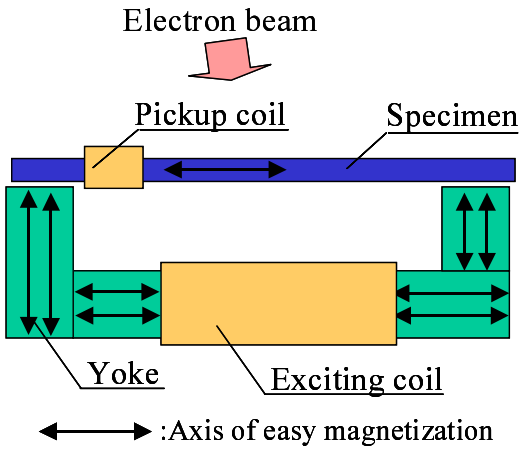

(c) Magnetic circuit

Fig. 3.16. SEM device for magnetic domain observation.

Table 3.1. Condition of observed SEM domain images. (H:Applied magnetic field intensity, B:Flux density)

No.	H [A/m]	B [T]	No.	H [A/m]	B [T]	No.	H [A/m]	B [T]
1	0.00	0.00	9	160.69	1.90	17	28.53	1.83
2	2.85	0.10	10	236.32	1.92	18	3.73	1.77
3	9.26	1.63	11	324.31	1.95	19	0.00	1.73
4	24.16	1.73	12	269.64	1.95	20	-4.60	1.73
5	30.23	1.78	13	214.13	1.93	21	-5.95	-0.06
6	54.59	1.84	14	160.37	1.92	22	-7.45	-1.43
7	84.92	1.86	15	98.68	1.91	23	-9.07	-1.56
8	115.39	1.88	16	54.66	1.84	24	-11.50	-1.62

3.3.2 Visualization of Magnetic Domain Dynamics

Suppose that a domain image as Fig.3.15 consists of a two-dimensional scalar field U, and then the dynamics of domains can be represented by the image Helmholtz equation. In magnetized state, since the domain motion is caused by applied external field H, then the image Helmholtz equation takes into account the first derivative term of the applied external field H:

$$\nabla^2 U + \alpha \frac{\partial U}{\partial H} = -\sigma, \tag{3.1}$$

where α and σ denote a domain motion parameter and an image source density given by the Laplacian of the final domain image, respectively. In Eq.(3.1), the parameter α is unknown. Calculation of the parameter α is the key to visualize the characteristic of domain motion dynamics as well as iron loss generating parts.

According to Section 2.3, a general solution of Eq.(3.1) is reduced into:

$$\mathbf{U}(H) = \mathrm{e}^{-\Lambda H}\left[\mathbf{U}(H_S) - \mathbf{U}(H_L)\right] + \mathbf{U}(H_L), \tag{3.2}$$

where $\mathbf{U}(H_S)$ and $\mathbf{U}(H_L)$ denote the initial and the final domain images, respectively. Because of the parameter α in Eq.(3.1), the state transition matrix $\mathrm{e}^{-\Lambda H}$ in Eq.(3.2) is unknown as well. It is essentially required to determine the elements of the state transition matrix from the given domain images.

If the solution $\mathbf{U}(H)$ in Eq.(3.2) is given as one of the domain images, then, it is possible to determine the elements of matrix Λ, the equivalent

characteristic values, as the same manner as Eq.(2.60), i.e.,

$$\Lambda = -\frac{1}{\Delta H} \ln \left[\frac{\mathbf{U}(H) - \mathbf{U}(H_L)}{\mathbf{U}(H_S) - \mathbf{U}(H_L)} \right]. \tag{3.3}$$

Since the matrix Λ is a diagonal matrix as described in Section 2.3.3, then Eq.(3.3) is carried out at each corresponding pixel value of three distinct domain images. Thereby, the elements in the i-th matrix Λ_i, are determined from a series of three distinct domain images:

$$\Lambda_i = -\frac{1}{H_{i+1} - H_i} \ln \left[\frac{\mathbf{U}(i+1) - \mathbf{U}(i+2)}{\mathbf{U}(i) - \mathbf{U}(i+2)} \right], \tag{3.4}$$

where $\mathbf{U}(i)$ refers to the i-th SEM domain images listed in Table 3.1. Finally, substituting Eq.(3.4) into Eq.(3.2) gives the solution with piecewise linear approximation.

3.3.3 Visualization of Iron Losses

As is well known, the state transition matrix of state variable equations represents the physical parameters and/or constants of the dynamic systems. Similarly, the state transition matrices Λ_i derived from a series of domain images by means of Eq.(3.4) is possible to extract the parameters representing domain dynamics of magnetization region from H_i to H_{i+1}. Due to a logarithmic function in Eq.(3.4), various cases of the element in the matrices Λ_i should be discussed. Let us consider an pixel $U(i)$ in the i-th frame of SEM domain animation with Eq.(3.5), which is the value under the logarithmic function in Eq.(3.4):

$$f_i \;=\; \frac{U(i+1) - U(i+2)}{U(i) - U(i+2)}. \tag{3.5}$$

Case 1: $f_i \geq 1$ The logarithmic function takes a positive real number or zero. Such an element in the matrices Λ just represents attenuation or no change term even though Eq.(3.1) is held.

Case 2: $0 < f_i < 1$ The logarithmic function takes a negative real number. Such an element in the matrices Λ represents divergence term.

Case 3: $f_i = 0$ The logarithmic function becomes indeterminate. This means that the pixel values $U(i+1)$ and $U(i+2)$ are identical not holding Eq.(3.1), i.e., the pixel value takes a constant during the state transition.

Case 4: $0 > f_i > -1$ The logarithmic function takes a complex number composing of the negative real and positive imaginary parts. This imaginary part means the phase lag to the variable H. Thus, iron loss can be visualized as in this case.

Case 5: $f_i \leq 1$ The logarithmic function takes a complex number composing of the positive real and imaginary parts. This complex number means the phase lag to the variable H. Thereby, iron loss can be visualized as the same as **Case 4**.

Fig.3.17 shows the elements in the matrices Λ_i. The arrangement of the elements is the same as the domain pattern in Fig.3.15. The elements become complex numbers due to the logarithmic function in Eq.(3.4). The real and imaginary parts represent in-phase and 90 difference phase components to the applied field, respectively. Namely, visualization of iron loss generating parts can be accomplished by the imaginary part of the matrices Λ_i.

At first, let us consider the real parts of the matrices in Fig.3.17. In the weak field, the moving parts of the negatively magnetized parts (black parts in Fig.3.15) relatively take larger in value. This magnetization process is mainly carried out by the magnetic boundary displacements [left hand side (LHS) of Fig.3.17(a)] and magnetic domain movements [LHS of Figs. 3.17(b) and (c)]. Increasing the field, the magnetization process by domain movement is finished. The elements in the matrices correspond to the rotation of magnetization [LHS of Figs. 3.17(d)-(g)]. In highly magnetized state, the elements shown in the LHS of Fig.3.17(h) takes relatively small in value due to saturation.

Second, consider the imaginary parts of the matrices in Fig.3.17. In the weak field, the real part of this region corresponds to the magnetic boundary displacement. However, in case of imaginary part, the elements in the right hand side (RHS) of Fig.3.17(a) are close to zero. This means that the magnetic boundaries move without delay components. In RHS of Fig.3.17(b)-(d), the values represent at the grain boundary. This is considered to be the friction among the grain boundaries. Increasing the field results in the closure domains. In this region, these elements are then related to iron loss [RHS of Fig.3.17(d) and (e)]. Moreover, in highly magnetized state as in Fig.3.17(h), magnetization proceeds at the closure domains although the saturation. The iron loss in this region can be visualized at these kinds of domain parts.

3.3.4 Comparison with Magnetization Models

In the references [37] and [56], relationship between the flux density B and field H has been clarified by a constitutive equation containing Preisach

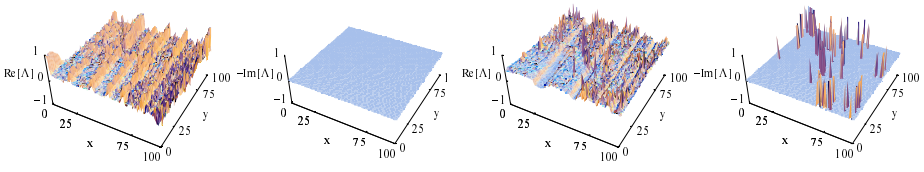

(a) $0 \leq H < 2.85$ A/m (b) $2.85 \leq H < 9.26$ A/m

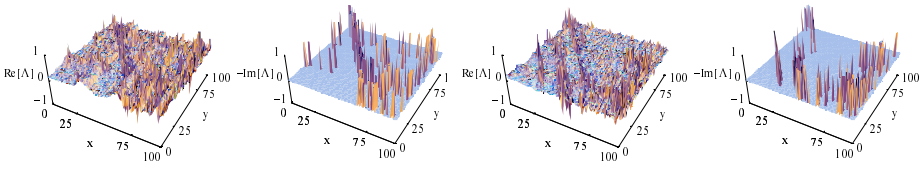

(c) $9.26 \leq H < 24.16$ A/m (d) $24.16 \leq H < 30.23$ A/m

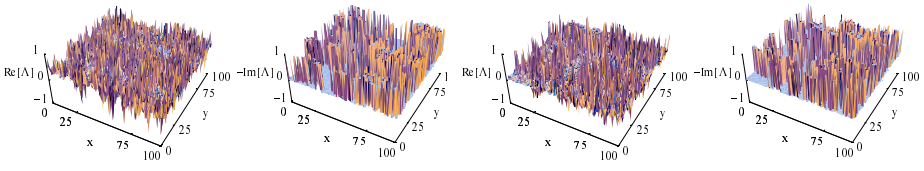

(e) $30.23 \leq H < 54.59$ A/m (f) $54.59 \leq H < 84.92$ A/m

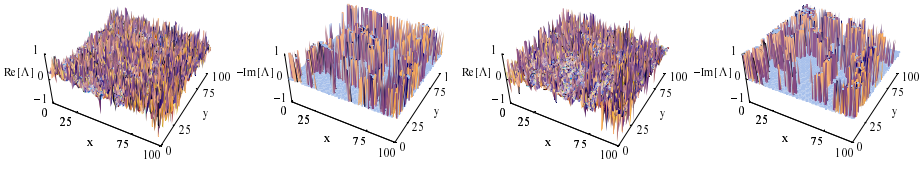

(g) $84.92 \leq H < 115.39$ A/m (h) $115.39 \leq H < 160.69$ A/m

Fig. 3.17. Visualization of iron loss by means of the equivalent characteristic values determined from three distinct SEM domain images (100×100 elements).

function Ψ:

$$H_e + H_c = \frac{1}{\mu}B + \frac{1}{\Psi}\frac{dB}{dH}, \tag{3.6}$$

where H_e and H_c are applied and coercive fields, respectively; μ is permeability. In addition, their intensive numerical and experimental works have verified the validity of Eq.(3.6). According to the reference [56], an analytical solution of Eq.(3.6) assuming the constant μ and Ψ gives,

$$\begin{aligned} B &= \mu H + [B_0 - \mu H]\exp(-\frac{\Psi}{\mu}H), \\ &= B_f + [B_0 - B_f]\exp(-\lambda H), \end{aligned} \tag{3.7}$$

where B_f and B_0 are the final and initial flux densities, respectively; and λ is characteristic value. When the three magnetic flux densities B_i, B_{i+1}, and B_{i+2} as the domain images during the field change ΔH_i, Eq.(3.7) can be rewritten by,

$$B_{i+1} = B_{i+2} + [B_i - B_{i+2}]\exp(-\lambda \Delta H_i). \tag{3.8}$$

Hence, modifying Eq.(3.8) gives Preisach function:

$$\Psi = \mu\lambda = -\frac{\mu}{\Delta H_i}\ln\left[\frac{B_{i+1} - B_{i+2}}{B_i - B_{i+2}}\right]. \tag{3.9}$$

Eq.(3.9) is just the same expression as equivalent characteristic values. The matrix Λ corresponds to Ψ/μ. Assuming constant μ and Ψ during $H_i \leq H < H_{i+1}$, Λ_i obtained by means of Eq.(3.4) makes it possible to represent Preisach function of its magnetization region with piecewise linear approximation. Moreover, the relation between Preisach function Ψ and the hysteresis paramater s shown in Eq.(2.61) is given by,

$$s = \Psi\frac{\partial H}{\partial t}. \tag{3.10}$$

Therefore, the dynamics of magnetization can be evaluated by means of the equivalent characteristic values when the applied field distribution is given.

Because Preisach function Ψ is the rate of change of permeability to the applied field [57,58], taking a large value in the real and imaginary parts of matrix Λ means that the rate of change of permeability to the applied field H is large, thereby, such a process is non-linear in the applied field. Conversely, a small value of Λ means that the rate of change of permeability to the applied field becomes small and results in linear magnetization processes.

3.3.5 Dynamic Domain Image Generation and Global Magnetization Curve

Substituting the matrices Λ of Eq.(3.4) into Eq.(3.1) yields domain images as the solution $\mathbf{U}(H)$, namely,

$$\mathbf{U}(H) = e^{\frac{1}{H_{i+1}-H_i}\ln\left[\frac{\mathbf{U}(i+1)-\mathbf{U}(i+2)}{\mathbf{U}(i)-\mathbf{U}(i+2)}\right]H}\left[\mathbf{U}(i)-\mathbf{U}(i+2)\right]+\mathbf{U}(i+2)\Big|_{H_i\le H\le H_{i+1}}. \tag{3.11}$$

Computing the averaged contrast of an entire domain image gives a flux density. Fig.3.18 shows the computed magnetization curve. Even though the domain images represent a limited area of the specimen, the experimental magnetization curve shown in Fig.3.19 supports the computed result.

3.3.6 Local Magnetization Curves

Focusing on the particular points on the domain images like in Fig.3.20, it is possible to generate the local magnetization curves as shown in Fig.3.21.

Fig.3.20 shows the selected parts for drawing local magnetization curves. The properties of selected parts are listed as follows:

1. Position Nos.1 and 2 : At the 180° domains
2. Position Nos.3 and 4 : At the lancet domains
3. Position Nos.5 and 6 : At the strained parts.

Fig.3.21 shows the magnetization curves computed from each of the pixel values. The local magnetization curves shown here are based on that of entire specimen in Fig.3.19. This methodology makes it possible to estimate the magnetization processes reflecting on the physical condition of the specimen.

At first, in the magnetization curves at the 180° basic domains [Fig.3.21(a)], the residual inductions are higher than those at the lancets [Fig.3.21(b)], and the strained parts [Fig.3.21(c)]. This means that the lancet and strained parts are hard to be magnetized. Inversely, the 180° basic domains are hard to move due to keeping minimum static magnetic energy. Second, in Fig.3.21(b), the discontinuous curves are obtained at the beginning of rotating magnetization region due to the lancet domain generations. This results in the theoretical conclusion in [59]. Finally, in Fig.3.21(c), a discontinuous curve is obtained at the position 5 due to the physical stress to the specimen. However, the curve at the position 6 is reconstructed smoothly. This is considered to cause by stretching strain.

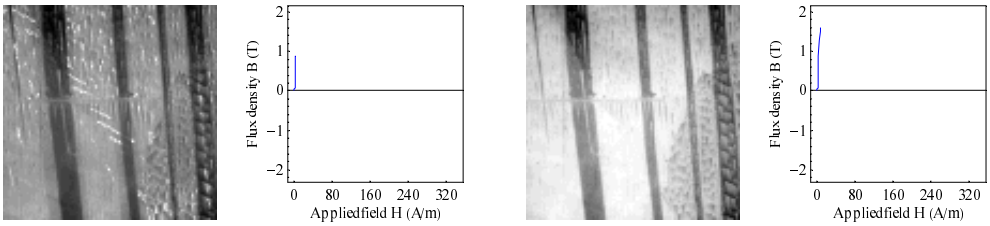

(a) 4.46 A/m, 0.90 T

(b) 9.27 A/m, 1.60 T

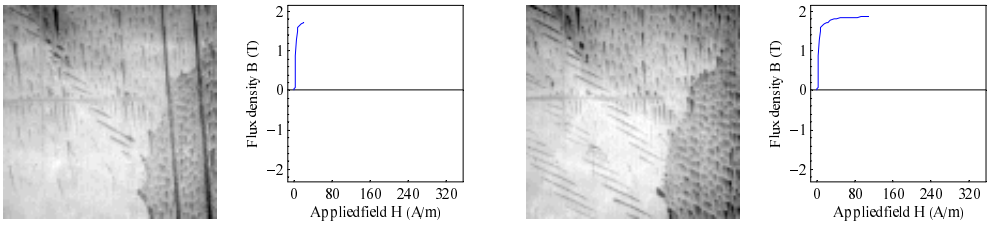

(c) 20.44 A/m, 1.71 T

(d) 107.77 A/m, 1.88 T

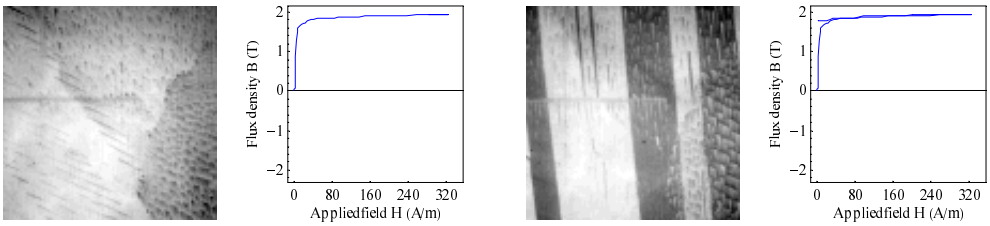

(e) 283.31 A/m, 1.95 T

(f) 3.73 A/m, 1.77 T

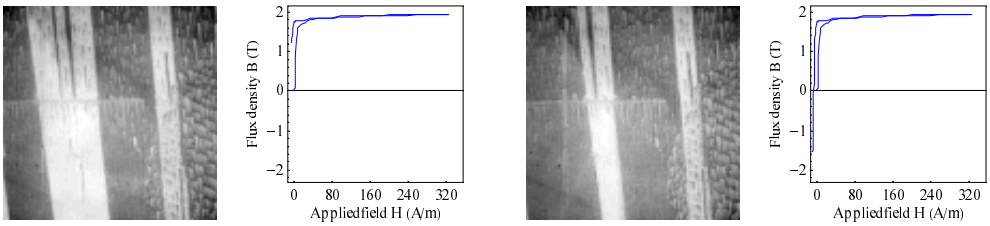

(g) -4.60 A/m, 1.22 T

(h) -8.65 A/m, -1.54 T

Fig. 3.18. Generated SEM domain images and global magnetization curves calculated from averaged contrasts of the generated images (100 × 100 pixels).

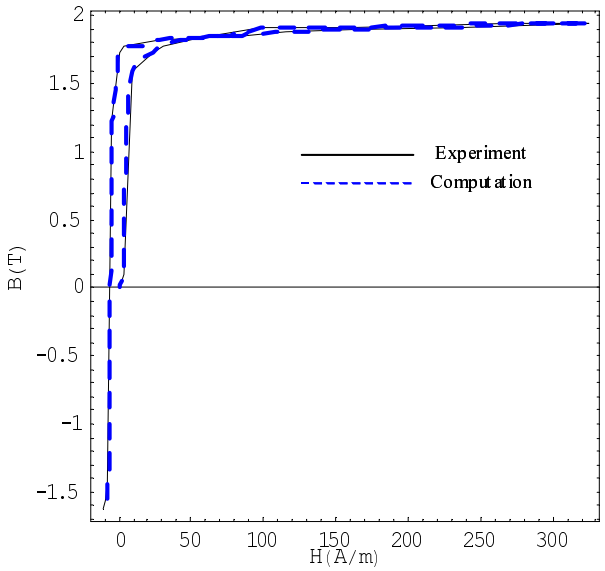

Fig. 3.19. Global magnetization curve obtained by averaged contrast of the generated domain images.

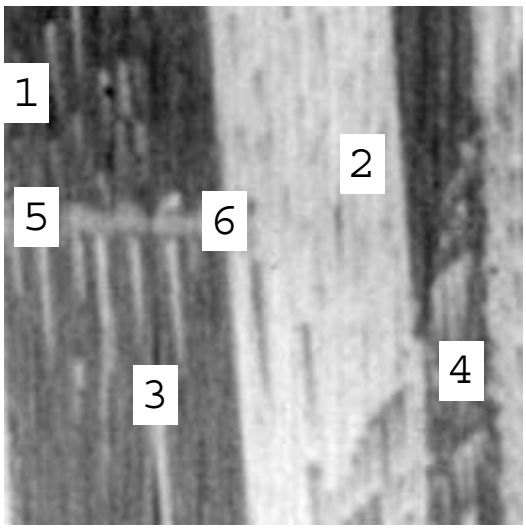

Fig. 3.20. Selected pixel positions for drawing the local magnetization curves. The background domain image is the same one as Fig.3.15(a). The positions 1 and 2 are at the 180° domains. The positions 3 and 4 are at the lancet domains. The positions 5 and 6 are at the strained parts.

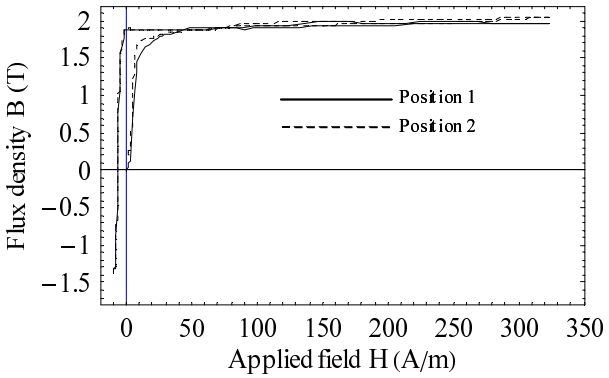

(a) At good crystallized parts

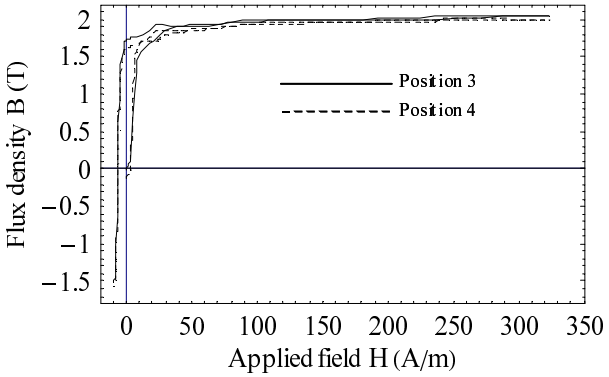

(b) At lancets

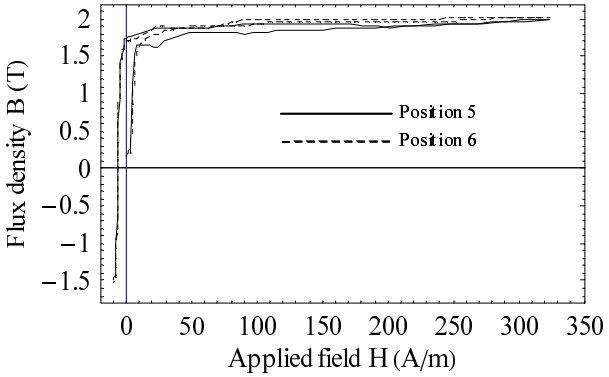

(c) At strained parts

Fig. 3.21. Local magnetization curves at various physical conditions. The curves are calculated from the pixel values of the generated SEM domain images. The drawn parts are shown in Fig.3.20.

3.3.7 Summary

This section proposes a method of iron loss visualization by means of the image Helmholtz equations. A series of distinct SEM domain images of a grain-oriented electrical steel is studied to clarify the domain dynamics and iron loss distribution.

At first, the image Helmholtz equation is applied to the SEM domain images and then the equivalent characteristic value derives the equivalent characteristic values, which corresponds to the state transition matrix, from the domain images. The evaluated state transition matrices enable to visualize any magnetization processes on the domain images. Since, the imaginary part of the state transition matrix corresponds the 90-degree phase different components to the applied field, and then iron loss generating parts have been visualized in particular. The elements in the state transition matrices show the domain dynamics such as boundary displacements, lancet domain generation and so on.

Second, the relation between the equivalent characteristic values and Preisach model is investigated. Composite model of Preisach and Chua models leads to the relation between the equivalent characteristic values and Preisach model from analytical solutions. Since Preisach function is a rate of change of permeability with respect to the applied field, then it is possible to evaluate nonlinearity of the local magnetization processes. Third, the magnetic domain images are generated as the solution of the image Helmholtz equations. Calculating averaged pixel values of generated domain images makes it possible to reproduce magnetization curve with high accuracy. Although the given SEM domain images show a small limited area, the measured magnetization curve well corresponds to the computed one.

Finally, the local magnetization curves can be obtained when the specific pixel values focused on, and they reflect on the domain physical situations. Good crystalized and physically strained parts are clearly classified by the generated local magnetization curves. The local magnetization curves show that the lancets give hysteresis loss in highly magnetization region.

Because the image Helmholtz equations is one of the systematic methodology to analyze visualized dynamics, the accuracy and limitation depend on only visualizing devices.

3.4 Fluid Dynamics

3.4.1 Visualized Animations in Fluid Dynamics

This section gives an application of the modal-wavelet transform (MWT). Three-dimensional multi-resolution analysis separates an infrared flow animation into the static and dynamic terms of animations.

Figure 3.22 shows some frames of an infrared animation observed by the weather satellite Himawari, showing the generation process of typhoon No. 9 in 2000 [60]. Applying MWT to this animation, separation of static and dynamic images is demonstrated. The animation used in this example is composed of 22 frames captured from 18:00 Aug. 10th to 15:00 Aug. 11th in 2000. Separation of the static and dynamic terms of animations is carried out by a multi-resolution analysis of MWT.

3.4.2 3D MWT and Multiresolution Analysis

In order to carry out MWT to the animation in Fig.3.22, the three-dimensional MWT is applied to red, green, and blue color components independently. Namely, applying MWT to horizontal-, vertical-, and frame- axes of each color compononent carries out an animation analysis. Let us consider one color component of the animation S_{lmn} having $m \times n$ pixels and l frames. Then, its transpose rules are defined by

$$[S_{lmn}]^T = S_{mnl}, \tag{3.12}$$
$$[S_{mnl}]^T = S_{nlm}, \tag{3.13}$$
$$[S_{nlm}]^T = S_{lmn}. \tag{3.14}$$

The three-dimensional MWT gives the modal-wavelet spectrum S'_{lmn}:

$$S'_{lmn} = \left[M_n \left[M_n \left[M_l S_{lmn} \right]^T \right]^T \right]^T, \tag{3.15}$$

where M_l, M_m and M_n are the l by l-, m by m- and n by n- MWT matrices, respectively [61]. And then, inverse MWT recovers the original animation S_{lmn}:

$$S_{lmn} = {M_l}^T \left[{M_m}^T \left[{M_n}^T \left[S'_{lmn} \right]^T \right]^T \right]^T. \tag{3.16}$$

Since a linear combination of weighted spectrum represents the original animation S_{lmn}, therefore, animation of each wavelet level can be obtained by means of Eq.(3.16).

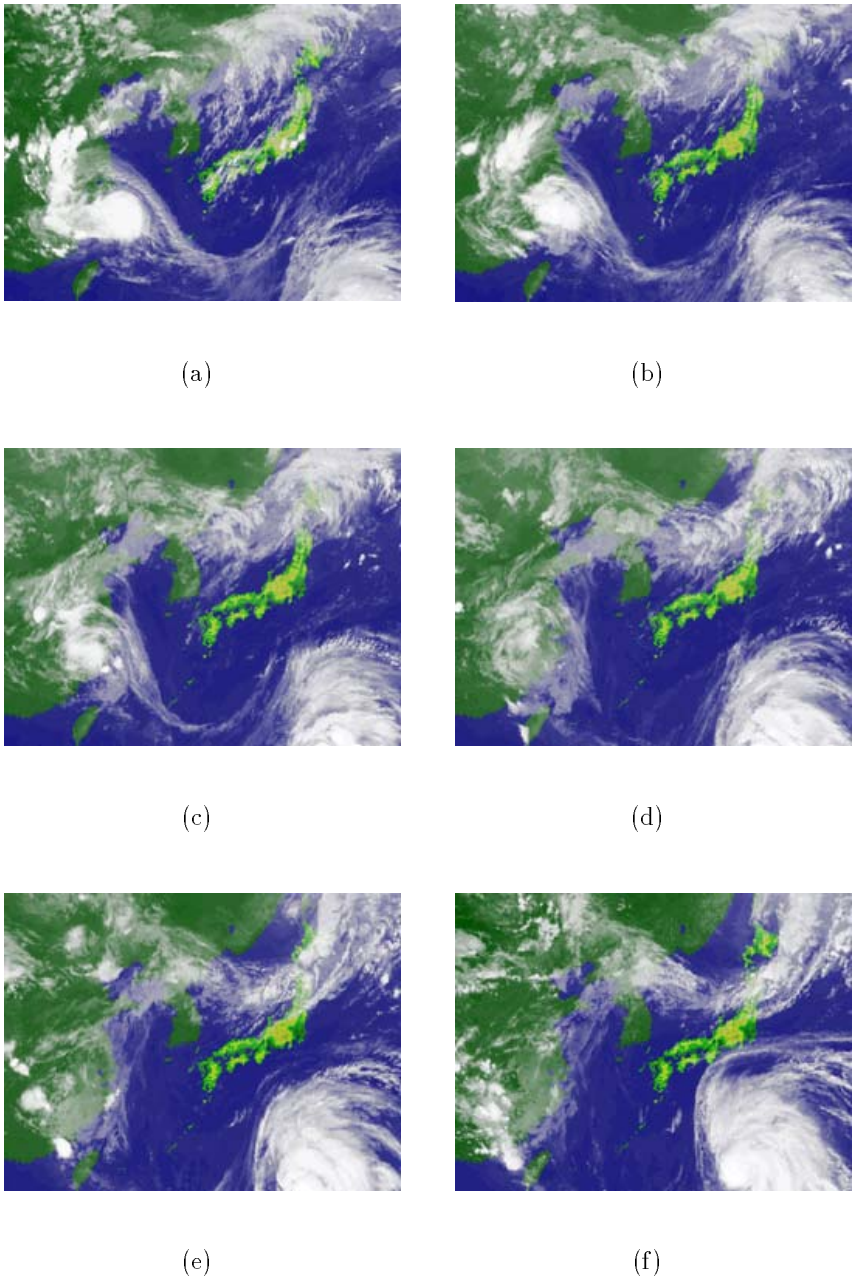

(a) (b)

(c) (d)

(e) (f)

Fig. 3.22. Frames of infrared animation by weather satellite Himawari (256×193 pixels). (a) At 18:00, Aug. 10, 2000. (b) At 22:00, Aug. 10, 2000. (c) At 2:00, Aug. 11, 2000. (d) At 6:00, Aug. 11, 2000. (e) At 10:00, Aug. 11, 2000. (f) At 14:00, Aug. 11, 2000.

In this demonstration, Eq.(3.15) and Eq.(3.16) are independently carried out to each color component. Then, the result of the modal, as well as conventional wavelet analysis can be obtained by synthesizing to be the color images.

3.4.3 Separation of Static and Dynamic Images

As described in Section 2.4 the MWT matrix derived from Neumann type boundary condition has a constant term. Utilizing the term makes it possible to extract the static terms of animation by means of multi-resolution analysis. In other words, the multi-resolution analysis to the frame axis is capable of extracting a common static image through entire frames of animation when employing the Neumann type MWT matrix. In much the same way, the dynamic frame images of animation can be extracted.

Figures 3.23 and 3.24 show the results of the multi-resolution analysis to the frame axis. Taking the lowest level of MWT into account the multi-resolution analysis of Eq.(3.16) yields the image in Fig.3.23. In this case, the generated result has some frames, but all of frames are identical to Fig.3.23. Thus, Fig.3.23 is the extracted background image suggesting static air pressure distribution. On the other hand, Fig.3.24 shows dynamic frame images of animation obtained by means of Eq.(3.16) without the lowest level of spectrum. The animation of which pixels vary can be obtained, showing that the cloud is moving.

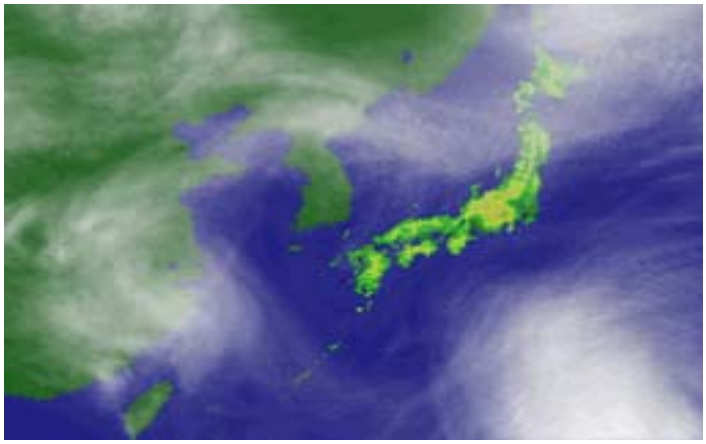

Fig. 3.23. Extracted static image (256 $\times$ 193 pixels).

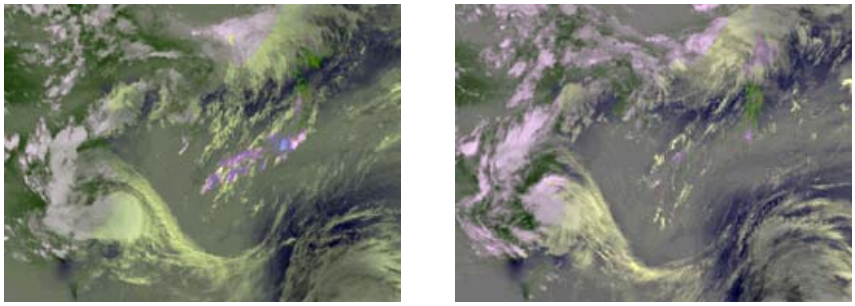

(a)

(b)

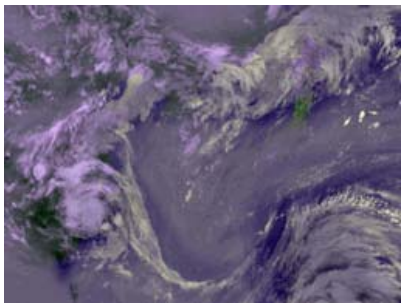

(c)

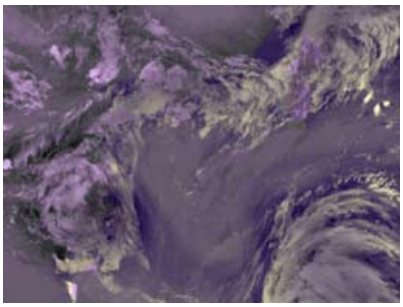

(d)

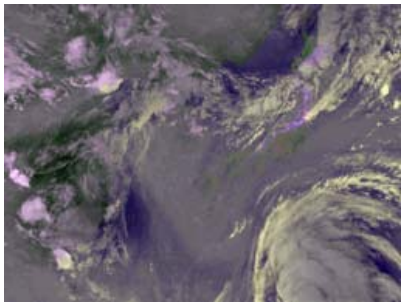

(e)

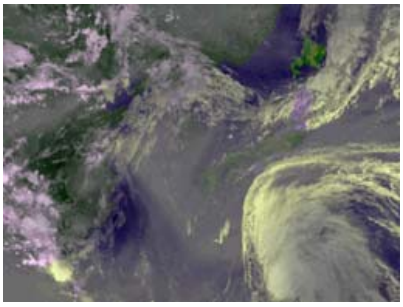

(f)

Fig. 3.24. Frames of extracted dynamic image (256 × 193 pixels). (a) At 18:00, Aug. 10, 2000. (b) At 22:00, Aug. 10, 2000. (c) At 2:00, Aug. 11, 2000. (d) At 6:00, Aug. 11, 2000. (e) At 10:00, Aug. 11, 2000. (f) At 14:00, Aug. 11, 2000.

3.4.4 Comparison with Conventional Wavelets

In the conventional discrete wavelets (DWT), the data sizes l, m, and n must be a power of 2. In this animation analysis, the animation shown in Fig.3.22 has 256 $\times$ 193 pixels and 22 frames. If the same analysis with conventional DWT is carried out, then l, m, and n described in Section 3.4.2 become 32, 256 and 256, respectively. In this case, zero-value elements must be added to the original data so that it satisfies with these l, m, and n . On the other hand, l, m, and n in MWT are 22, 256 and 193, respectively. MWT dispenses with arrangement of the original data because the dimension of transform matrix is free from the *"power of 2"* problem. It is obvious that MWT accomplishes an efficient analysis from the viewpoint of memory consumption.

3.4.5 Summary

This section gives an application of the MWT. This linear transformtion derived from the image governing equations makes it possible to carry out efficient multi-resolution analysis.

Three-dimensional multi-resolution analysis using MWT devides the visualized fluid animation observed by weather satellite into the static and dynamic terms of animation. One of the bases in MWT matrix derived from differential equation with Neumann boundary condition is constant term so that static term of animation can be extracted systematically. Inversely, extraction of dynamic terms of animation is also performed by removing the static term.

The same analysis by Daubechies 2nd order, which has also a basis of constant itself, yields the comparable results with those of MWT. The animation analysis based on the three-dimensional multi-resolution analysis shows high efficiency in terms of memory consumption compared with those of the conventional DWT. This is because the dimension of MWT matrix is free from the problem on subject data length, while length of taget data for DWT should be power of 2.

The image modeling based on the classical field theory is capable of deriving various kinds of orthonormal bases from the governing differential- as well as integral- expressions. Thus, MWT approach has versatile capability not only to information resource handling but also smart computing.

CHAPTER 4

Conclusions

This thesis has proposed an image modeling based on the classical field theory in order to realize systematic image handling methodologies for visualized images. It has been described by a couple of principal chapters. The contents and results are summarized as follows:

Chapter 2 has described the theoretical background to propose an image modeling for the visualized images. Assume pixel representing digital images to be a kind of field potentials, then the image handling methodologies and its mathematical formulation can be systemized. At first, monochrome and color images have been fomulated by scalar and vector potentials, respectively. Coulomb gauge has been assumed to derive independence of the RGB components each other. Second, the image vector operations have been introduced to derive the image governing equations and the solution strategies for them. Third, the image Poisson equation has been implemented by the finite differences, finite elements, and Green's function schemes. The demonstration has shown that the boundary condition plays important role in recovering images exactly. Morever, the image source density derived from the Laplacian has given one of the systematic representation for image processing methodologies. The image Helmholtz equation has represented animations. Modal analysis of the image Helmholtz equation has derived a general solution, showing that two frame of animation and a state transition matrix are essentially required to generate animations. The equivalent characteristic value has been proposed to determine the state transition matrix from the given three frames of animation in stead of the known state transition matrix. The frames of animation have been successfully generated continuously as the solution of the image Helmholtz equation. Finally, MWT has been derived from modal analysis of the image equations, performing orthonormal base functions having the nature of both wavelet and Fourier transforms.

Chapter 3 has demonstrated some applications in visualized images. At first, the image vector operations have been applied to the sketch-like image generation and flaw classification problems. Magnitudes, as well as directions of the image vectors have generated the monochrome as well as color sketch-like images, suggesting that one of the human-oriented tasks is worked out. Orientations, as well as magnitudes of the image vectors have also classified VT images into the line and circle types of flaws in a most efficient manner. Second, the image Poisson equation has improved the resolution of a measured magnetic vector field. Refining the imaged magnetic field has been carried out by the image Poisson equation with fine subdivision. Third, magnetic domain dynamics have been analyzed by the image Helmholtz equation. The iron loss visualization along with Preisach magnetization model has been obtained. Global and local magnetization curves have been generated from the solutions of image Helmholtz equation. Finally, MWT has been demonstrated in three-dimensional multi-resolution analysis of an infrared flow animation. The static and dynamic terms of animations have been successfully decomposed. MWT has made it possible to carry out the orthonormal transform in a quite efficient manner.

An unified approach from the partial differential equations and integral equations to the orthonormal transformation has been successfully worked out. The image modeling studied here is just corresponding to mathematical models in physical fields like electromagnetism. It is obvious that any image analysis based on this image modeling could be carried in a quite efficient manner when applying to the visualized physical systems. Whenever the GUI-based computers and visualizing devices are available, the systematic approaches to represent image data accomplish various sort of problems on visualization.

References

[1] T. Kinoshita, "Performance Trends of Computers in the Last Decade," *Journal of the Japan Society of Applied Electromagnetics and Mechanics (in Japanese)*, Vol.9, No.3, pp.295-300, 2001.

[2] http://www.spec.org

[3] H. Huang and T. Takagi, "Progress of Computers and Its Effects to Simulation of Eddy Current Testing," *Journal of the Japan Society of Applied Electromagnetics and Mechanics (in Japanese)*, Vol.9, No.3, pp.322-328, 2001.

[4] S.R.H. Hoole, *Computer-Aided Analysis and Design of Electromagnetic Devices*, Elsevier, NY, 1989.

[5] H. Freeman, *Interactive Computer Graphics*, IEEE Computer Society Press, NJ, 1980.

[6] T. Fomenko and T.L. Kunii, *Topological Modeling for Visualization*, Springer-Verlag, Tokyo, 1977.

[7] M. Morrison, *Becoming a Computer Animator*, SAMS Publishing, IN, 1994.

[8] H. Yamashita, "Visualization of Electromagnetic Phenomena," *The Journal of IEE of Japan (in Japanese)*, Vol.119, No.3, pp.169-172, 1999.

[9] P.M. Morse and H. Feshbach, *Methods of Theoretical Physics*, McGraw-Hill, NY, 1953.

[10] E.A. Hylleraas, *Mathematical and Theoretical Physics*, John Wiley & Sons, NY, 1970.

[11] J.D. Jackson, *Classical Electrodynamics 3rd Edition*, John Wiley & Sons, NY, 1998.

[12] P.P. Silvester, *Modern Electromagnetic Fields*, Prentice-Hall, NJ, 1968.

[13] P.P. Silvester and R.L. Ferrari, *Finite Elements for Electrical Engineers*, Cambridge University Press, Cambridge, 1983.

[14] H. Endo, S. Hayano, Y. Saito, and T. L. Kunii, "A Comparison Wavelets and Image Calculus Compressions," *Journal of the Visualization Society of Japan (in Japanese)*, Vol.19, Suppl.No.1, pp.79-82, 1999.

[15] R.W. Hamming, *Numerical Methods for Scientists and Engineers*, McGraw-Hill, NY, 1962.

[16] C.W. Steele, *Numerical Computation of Electric and Magnetic Fields*, Van Nostrand Reinhold Company, NY, 1987.

[17] E.A. Guillemin, *The Mathematics of Circuit Analysis*, The MIT Press, Cambrige, 1969.

[18] H. Endo, S. Hayano, Y. Saito, and T. L. Kunii, "Image Governing Equations and Its Application to Vector Fields," *Trans. IEE of Japan (in Japanese)*, Vol.120-A, No.12, pp.1089-1093, 2000.

[19] H. Endo, S. Hayano, Y. Saito, and T. L. Kunii, "Image Processing by Field Theory -Part 1 Theoretical Background," *Proceeding of the XII-th International Symposium on Electrical Apparatus and Technologies (SIELA 2001) Vol. II, Provdiv, Bulgaria*, pp.39-45, 2001.

[20] H. Togawa, *Numerical Calculations for Differential Equations (in Japanese)*, Ohm Pub., Tokyo, 1973.

[21] T. Akasaka, *Numerical Calculation (in Japanese)*, Corona Pub., Tokyo, 1968.

[22] T. Mori and T. Sakakura, *Fundamentals of Image Recognition [II] – Feature Extraction, Edge Detection and Texture Analysis – (in Japanese)*, Ohm Pub., Tokyo, 1990.

[23] M. Sakuma, K. Kubo, T. Butsusen, Y. Saito, and K. Horii, "Development of the System for Visual Inspection of Material Based on Vector Analysis Technique," *Proceeding of the 6th Symposium on Image Sensing (in Japanese)*, pp.—, 1999.

[24] H. Iwasaki, Y. Saito, C. Kato, S. Hanta, and K. Horii, "Surface Information Extraction from the Sketch Image," *Journal of the Visualization Society of Japan (in Japanese)* , Vol.19, Suppl.No.1, pp.79-82, 1999.

[25] H. Endo, S. Hayano, Y. Saito, and T. L. Kunii, "A Method of Image Processing and Its Application to Magnetodynamic Fields," *Trans. IEE of Japan (in Japanese)*, Vol.120-A, No.10, pp.913-918, 2000.

[26] Y. Saito, "Smart Visualized Information Processing –Part. 2: Image Governing Equations–," *Journal of the Japan Society of Applied Electromagnetics and Mechanics (in Japanese)*, Vol.10, No.1, pp.41-52, 2001.

[27] http://sipi.usc.edu/services/database/Database.html

[28] H. Endo, I. Marinova, S. Hayano, Y. Saito, and K. Horii, "Modal-Wavelets and Their Applications," *JSAEM Studies in Applied Electromagnetics and Mechanics 14 (Eds. S. Yamada et al.)*, pp.279-284, 2003.

[29] H. Endo, I. Marinova, S. Hayano, Y. Saito, and K. Horii, "Modal-Wavelet Transform for Smart Visualization Tool," *Proceeding of the 10th International Symposium on Flow Visualization (ISFV10), Kyoto, Japan*, F0306, 2002.

[30] I. Stakgold, *Green's Functions and Boundary Value Problems*, John Wiley & Sons, NY, 1979.

[31] G. Strang, *Linear Algebra and Its Applications*, Academic Press, NY, 1976.

[32] H. Endo and Y. Saito, "Methodologies for Electromagnetic Field Analysis Using Visualized Field Images," *Journal of Magnetic Society of Japan (in Japanese)*, Vol.28, No.1, pp.15-21, 2004.

[33] Y. Saito, Y. Nakazawa, and S. Hayano, "Non-spurious Finite Element Solution of Eddy Current Problems," *The Papers of Technical Meeting on Magnetics, IEE Japan (in Japanese)*, SA-90-20, 1990.

[34] H. Endo and Y. Saito, "Smart Visualization and Computer Vision in Electromagnetism," *Int. J. Appl. Electromagn. Mech.*, Vol.15, No.1-4, pp.337-342, 2001/2002.

[35] Y. Shigeta, S. Hayano, and Y. Saito, "Magnetic Sensor Signal Analysis," *Int. J. Appl. Electromagn. Mech.*, Vol.15, No.1-4, pp.349-352, 2001/2002.

[36] L.O. Chua and K.A. Stromsmoe, "Lumped Circuit Models for Nonlinear Inductor Exhibiting Hysteresis Loops," *IEEE Trans. Circuit Theory*, Vol.CT-17, No.4, pp.564-574, 1970.

[37] A. Ivanyi, *Hysteresis Models in Electromagnetic Computation*, Akademiai Kiado, Budapest, 1997.

[38] Y. Saito, K. Fukushima, S. Hayano, and N. Tsuya, "Application of a Chua type Model to the Loss and Skin Effect Calculation," *IEEE Trans. Magn.*, Vol.MAG-23, No.5, pp.2227-2229, 1987.

[39] S. Hayano, H. Saotome, A. Miyazaki, and Y. Saito, "A Representation of Magnetization Characteristics for Computational Magnetodynamics," *Int. J. Appl. Electromagn. Mech.*, Vol.2, No.4, pp.353-358, 1992.

[40] I. Marinova, et al., "Image Reconstruction for Electromagnetic Field Visualization by an Inverse Problem Solution," *Int. J. Appl. Electromagn. Mech.* , Vol.15, No.1-4, pp.403–408, 2001/2002.

[41] S.G. Mallat, "A Theory for Multiresolution Signal Decomposition: the Wavelet Representation," *IEEE Trans. Pattern Anal. & Mach. Intell.*, Vol.11, No.7, pp.674 -693, 1989.

[42] G. Beylkin, et al., "Fast Wavelet Transforms and Numerical Algorithms, I," *Commun. Pure and Appl. Math.*, Vol.44, pp.141–183, 1991.

[43] W.H.Press, B.P.Flannery, S.A.Teukolsky, and W.T.Vetterling, *Numerical Recipes in C*, Cambridge University Press, Cambridge, 1988.

[44] S. Hayano, H. Saotome, Y. Nakajima, and Y. Saito, "A New Type High Frequency Transformer," *IEEE Trans. Magn.*, Vol.MAG-27, No.6, pp.5205-5207, 1991.

[45] T. Ogawa, H. Saotome, S. Hayano, and Y. Saito, "Realization of a Coreless Transformer and Its Application to a DC/DC Converter," *Elektrotechn.CAS*, Vol.44, No.7, pp.238-241, 1993.

[46] S. Hayano, Y. Midorikawa, and Y. Saito, "Development of Film Transformer," *IEEE Trans. Magn.*, Vol.MAG-30, No.6, pp.4758-4760, 1994.

[47] A. Hubert and R. Schafer, *Magnetic Domains*, Springer-Verlag, Berlin, 2000.

[48] J. -P. Jamet et al., "Dynamics of the Magnetization Reversal in Au/Co/Au Micrometer-size Dot Arrays," *Phys. Rev. B*, Vol.57, No.22, pp.14320-14331, 1998.

[49] S. -B. Choe and S. -C. Shin, "Magnetization Reversal Dynamics with Submicron-scale Coercivity Variation in Ferromagnetic Films," *Phys. Rev. B*, Vol.62, No.13, pp.8646-8649, 2000.

[50] H. Endo, S. Hayano, Y. Saito, C. Kaido, and M. Fujikura, "Magnetization Curve Plotting From the Magnetic Domain Images," *IEEE Trans. Magn.*, Vol.37, No.10, pp.2727-2730, 2001.

[51] H. Endo, S. Hayano, and Y. Saito, "An Image-Based Approach for Preisach Function Calculation," *IEEE Trans. Magn.*, Vol.38, No.5, pp.2424-2426, 2002.

[52] H. Endo, Y. Saito, S. Hayano, and K. Miya, "Classical and IT Based Magnetization Dyanamics Modeling," *Int. J. Appl. Electromagn. Mech.*, Vol.16, No.3-4, pp.153-161, 2002.

[53] H. Endo, S. Hayano, H. Mogi, M. Fujikura, C. Kaido, and Y. Saito, "Estimation of Iron Loss Distribution by Image Helmholtz Equation Method," *IEEE Trans. Magn.*, Vol.39, No.3, pp.1377-1380, 2003.

[54] T. Nozawa, T. Yamamoto, Y. Matsuo, and Y. Ohya, "Effects of Scratching on Losses in 3-percent Si-Fe Single Crystals with Orientation Near (110)[001]," *IEEE Trans. Magn.*, Vol.15, No.2, pp.972-981, 1979.

[55] K. Tsuno and T. Yamamoto, "Observed Depth of Magnetic Domains and Their Walls in Scanning Electron Microscopy," *Phys. Stat. Sol. (a)*, Vol.37, No.–, pp.437-448, 1976.

[56] Y. Saito, S. Hayano, and Y. Sakaki, "A Parameter Representing Eddy Current Loss of Soft Magnetic Materials and Its Constitutive Equation," *J. Appl. Phys.*, Vol.64, No.1, pp.5684-5686, 1988.

[57] F. Preisach, "Über die magnetische nachwirkung ," *Zeitschrift für physik (in German)*, Vol.94, No.5-6, pp.277-, 1935.

[58] G. Kadar and E. Della Torre, "Hysteresis Modeling: I. Noncongruency," *IEEE Trans. Magn.*, Vol.MAG-23, No.5, pp.2820-2822, 1987.

[59] C. Kaido, et al., "A Discussion of the Magnetic Properties of Non-oriented Steel Sheets," *The Papers of Technical Meeting on Magnetics, IEE Japan (in Japanese)*, MAG-99-173, 1999.

[60] http://www.jwa.or.jp/

[61] S. Matsuyama, et al., "Development of n-th Dimensional Bi-orthogonal Wavelets Transform and Its Applications," *Journal of The Visualization Society of Japan (in Japanese)*, Vol.21, No.1, pp.347–350, 1999.

APPENDIX A

A List of the Related Works by the Author

A.1 Full Reviewed Papers

[1] H. Endo, S. Hayano, Y. Saito, and T. L. Kunii, "A Method of Image Processing and Its Application to Magnetodynamic Fields," *Trans. IEE of Japan (in Japanese)*, Vol.120-A, No.10, pp.913-918, 2000.

[2] H. Endo, S. Hayano, Y. Saito, and T. L. Kunii, "Image Governing Equations and Its Application to Vector Fields," *Trans. IEE of Japan (in Japanese)*, Vol.120-A, No.12, pp.1089-1093, 2000.

[3] H. Endo, S. Hayano, Y. Saito, C. Kaido, and M. Fujikura, "Magnetization Curve Plotting From the Magnetic Domain Images," *IEEE Trans. Magn.*, Vol.37, No.10, pp.2727-2730, 2001.

[4] H. Endo, S. Hayano, and Y. Saito, "An Image-Based Approach for Preisach Function Calculation," *IEEE Trans. Magn.*, Vol.38, No.5, pp.2424-2426, 2002.

[5] H. Endo and Y. Saito, "Smart Visualization and Computer Vision in Electromagnetism," *Int. J. Appl. Electromagn. Mech.*, Vol.15, No.1-4, pp.337-342, 2001/2002.

[6] C. Kato, H. Endo, Y. Saito, and K. Horii, "Application of the Fourier-Wavelet Transform to Moving Images in an Interview Scene," *Int. J. Appl. Electromagn. Mech.*, Vol.15, No.1-4, pp.359-364, 2001/2002.

[7] N. Morohoshi, H. Endo, Y. Saito, and K. Horii, "How to Read a Novel –Analysis Using Wavelets Transform–," *Int. J. Appl. Electromagn. Mech.*, Vol.15, No.1-4, pp.371-375, 2001/2002.

[8] T. Naruta, H. Endo, S. Hayano, and Y. Saito, "A Study of Planar Inductor," *Int. J. Appl. Electromagn. Mech.*, Vol.15, No.1-4, pp.377-382, 2001/2002.

[9] I. Marinova, H. Endo, S. Hayano, and Y. Saito, "Image Reconstruction for Electromagnetic Field Visualization by an Inverse Problem Solution," *Int. J. Appl. Electromagn. Mech.*, Vol.15, No.1-4, pp.403-408, 2001/2002.

[10] H. Endo, S. Hayano, M. Fujikura, H. Mogi, C. Kaido, and Y. Saito, "Magnetic Domain Dynamics Visualization," *Int. J. Appl. Electromagn. Mech.*, Vol.15, No.1-4, pp.409-416, 2001/2002.

[11] H. Endo, Y. Saito, S. Hayano, and K. Miya, "Classical and IT Based Magnetization Dynamics Modeling," *Int. J. Appl. Electromagn. Mech.*, Vol.16, No.3-4, pp.153-161, 2002.

[12] H. Endo, S. Hayano, H. Mogi, M. Fujikura, C. Kaido, and Y. Saito, "Estimation of Iron Loss Distribution by Image Helmholtz Equation Method," *IEEE Trans. Magn.*, Vol.39, No.3, pp.1377-1380, 2003.

[13] G. Y. Dong, H. Endo, S. Hayano, S. K. Gao, and Y. Saito, "GVSPM for Reconstruction in Electrical Impedance Tomography," *IEEE Trans. Magn.*, Vol.39, No.3, pp.1630-1633, 2003.

[14] H. Endo, I. Marinova, S. Hayano, and Y. Saito, "An Analysis of a Ferroresonant Circuit With Chaotic Behavior by Means of a Chua-Type Magnetization Model," *IEEE Trans. Magn.*, Vol.39, No.5, pp.2546-2548, 2003.

[15] H. Endo, Y. Takasuka, I. Marinova, S. Hayano, and Y. Saito, "Data Representation by Field Calculus and Leading to the Orthonormal Linear Transforms," *Int. J. Appl. Electromagn. Mech.* , —(in press).

[16] H. Endo, I. Marinova, S. Hayano, and Y. Saito, "Ferroresonance Circuit Exhibiting Chaotic Phenomenon –Rule Extraction from Nonlinear Systems–," *Int. J. Appl. Electromagn. Mech.* , —(in press).

[17] H. Endo, I. Marinova, T. Takagi, S. Hayano, and Y. Saito, "Dynamics on Ferroresonance Circuit Exhibiting Chaotic Phenomenon," *IEEE Trans. Magn.*, —(in press).

[18] I. Marinova, H. Endo, S. Hayano, and Y. Saito, "Inverse Electromagnetic Problems by Field Visualization," *IEEE Trans. Magn.*, —(in press).

[19] H. Endo, I. Marinova, S. Hayano, Y. Saito, and K. Horii, "Modal-Wavelet Transform as a Smart Visualization Tool," *Int. J. Wavelets, Multiresolution and Information Processing*, —(in press).

A.2 International Conference/Workshop Contribution

[1] M. Aoki, H. Endo, S. Hayano, and Y. Saito, "Eddy Current Testing by the Modified Rogowski Coil," *JSAEM Studies in Applied Electromagnetics and Mechanics 11 (Eds. A. Nafalski and M. Saghafifar)*, pp.29-33, 2001.

[2] Y. Senoo, H. Endo, S. Hayano, and Y. Saito, "A Study of Magnetic Tilt Sensor," *JSAEM Studies in Applied Electromagnetics and Mechanics 11 (Eds. A. Nafalski and M. Saghafifar)*, pp.35-40, 2001.

[3] H. Endo, S. Hayano, Y. Saito, T. L. Kunii, C. Kaido, and M. Fujikura, "Electromagnetic Computer Vision," *JSAEM Studies in Applied Electromagnetics and Mechanics 11 (Eds. A. Nafalski and M. Saghafifar)*, pp.99-102, 2001.

[4] H. Endo, S. Hayano, Y. Saito, T. L. Kunii, and K.Horii, "Smart Dynamic Image Analysis Based on the Field Theory," *The 3rd Pacific Symposium on Flow Visualization and Image Processing (PSFVIP-3), Maui, USA*, F3306, 2001.

[5] H.Kochi, H. Endo, S. Hayano, and Y. Saito, "Visualization of Magnetic Sensor Signal," *The 3rd Pacific Symposium on Flow Visualization and Image Processing (PSFVIP-3), Maui, USA*, F3314, 2001.

[6] T. Naruta, H. Endo, S. Hayano, and Y. Saito, "A Study of Planar Inductor," *The 3rd Pacific Symposium on Flow Visualization and Image Processing (PSFVIP-3), Maui, USA*, F3304, 2001.

[7] Y. Seno, H. Endo, S. Hayano, and Y. Saito, "Wavelet Analysis of the Magnetic Field Distributions in Magnetic Tilt Sensor," *The 3rd Pacific Symposium on Flow Visualization and Image Processing (PSFVIP-3), Maui, USA*, F3312, 2001.

[8] H. Endo, S. Hayano, and Y. Saito, "Visualization of Magnetization Dynamics," *JSAEM Studies in Applied Electromagnetics and Mechanics 12 (Eds. M.Enokizono and A.G.Mamalis)*, pp.23-27, 2002.

[9] H. Endo, S. Hayano, Y. Saito, and T. L. Kunii, "Magnetic Field Imaging by Differential Equations," *JSAEM Studies in Applied Electromagnetics and Mechanics 13 (Eds. K. Yamada et al.)*, pp.226-229, 2002.

[10] H. Endo, S. Hayano, Y. Saito, and K. Miya, "Generalized Vector Sampled Pattern Matching Method -Theory and Applications-," *Studies in Applied Electromagnetics and Mechanics 23 Electromagnetic Nondestructive Evaluation (VI) (Eds. F. Kojima et al.), IOS Press, The Netherlands*, pp.285-292, 2002.

[11] H. Endo, S. Hayano, Y. Saito, and T. L. Kunii, "Image Processing by Field Theory -Part 1 Theoretical Background," *Proceeding of the XII-th International Symposium on Electrical Apparatus and Technologies (SIELA 2001) Vol. II, Provdiv, Bulgaria*, pp.39-45, 2001.

[12] H. Endo, S. Hayano, Y. Saito, and T. L. Kunii, "Image Processing by Field Theory -Part 2 Applications," *Proceeding of the XII-th International Symposium on Electrical Apparatus and Technologies (SIELA 2001) Vol. II, Provdiv, Bulgaria*, pp.46-53, 2001.

[13] I. Marinova, H. Endo, S. Hayano, and Y. Saito, "Electromagnetic Field Visualization by Image Processing," *Proceeding of the XII-th International Symposium on Electrical Apparatus and Technologies (SIELA 2001) Vol. II, Provdiv, Bulgaria*, pp.—, 2001.

[14] T. Sato, H. Endo, S. Hayano, and Y. Saito, "Image Cognition by Means of Inverse Approach," *Proceeding of the XII-th International Symposium on Electrical Apparatus and Technologies (SIELA 2001) Vol. II, Provdiv, Bulgaria*, pp.112-119, 2001.

[15] I. Marinova, H. Endo, S. Hayano, and Y. Saito, "Field Visualization by Image Processing," *Proceeding of the 10th International Symposium on Flow Visualization (ISFV10), Kyoto, Japan*, F0018, 2002.

[16] N. Morohoshi, H. Endo, Y. Saito, H. Tsuchiya, and K. Horii, "Visualization of Author Characteristics," *Proceeding of the 10th International Symposium on Flow Visualization (ISFV10), Kyoto, Japan*, F0175, 2002.

[17] H. Endo, I. Marinova, S. Hayano, Y. Saito, and K. Horii, "Modal-Wavelet Transform for Smart Visualization Tool," *Proceeding of the 10th International Symposium on Flow Visualization (ISFV10), Kyoto, Japan*, F0306, 2002.

[18] Y. Okubo, H. Endo, I. Marinova, S. Hayano, and Y. Saito, "Continuous Visualization of Magnetic Domain Dynamics by Image Helmholtz Equation," *Proceeding of the 10th International Symposium on Flow Visualization (ISFV10), Kyoto, Japan*, F0297, 2002.

[19] H. Endo, I. Marinova, S. Hayano, Y. Saito, and K. Horii, "Modal-Wavelets and Their Applications," *JSAEM Studies in Applied Electromagnetics and Mechanics 14 (Eds. S. Yamada et al.)*, pp.279-284, 2003.

[20] H. Endo, I. Marinova, T. Takagi, S. Hayano, and Y. Saito, "A New Inspection Methodology For Silicon Steel Sheet Quality Evaluation Based on Image Helmholtz Equation," *Studies in Applied Electromagnetics and Mechanics, Vol. 25 Electromagnetic Nondestructive Evaluation (VIII) (Eds. T. Sollier et al.), IOS Press, The Netherlands*, pp.—, (in press).

[21] H. Huang, H. Endo, T. Uchimoto, T. Takagi, A. Nishimizu, M. Koike, and T. Matsui, "Eddy Current Testing and Sizing of Deep Cracks in a Thick Structure," *Proceeding of Review of Progress in Quantitative Nondestructive Evaluation (QNDE2003), Wisconsin, USA, American Institute of Physics*, pp.—, (on reviewing).

[22] H. Yang, H.Y. Tian, X.L. Li, Y. Saito, W. He, X. Xian, H. Endo, "An Application of Electrical Impedance Tomography in Nondestructive Detecting," *Proceeding of Asian Symposium on Applied Electromagnetics and Mechanics (ASAEM2003), Seoul, Korea, Korean Society of Applied Electromagnetics and Mechanics*, pp.—, (on reviewing).

[23] Y. Nagaya, H.J. Jung, L. Bartolomeo, H. Endo, T. Uchimoto, and T. Takagi, "ECT Camera System for Crack Visualization," *Proceeding of the First International Symposium on Intelligent Artifacts and Bio-Systems (INABIO), Sendai, Japan*, pp.—, (on reviewing).

A.3 Domestic Conference/Workshop Contribution

[1] H. Endo, S. Hayano, Y. Saito, and T. L. Kunii, "A Comparison Wavelets and Image Calculus Compressions," *Journal of the Visualization Society of Japan*, Vol.19, Suppl.No.1, pp.79-82, 1999.

[2] H. Endo, S. Hayano, Y. Saito, T. L. Kunii, M.Sakuma, and K.Horii, "An Analysis of Electromagnetic Field Distribution by means of Image Processing," *The Papers of Technical Meeting on Magnetics, IEE Japan*, MAG-99-141, 1999.

[3] H. Endo, S. Hayano, Y. Saito, T. L. Kunii, M.Sakuma, and K.Horii, "An Approach of Image Processing and Its Application to Electromagnetic Field Distribution Analysis," *Proceeding of the 20th Japan Simulation Society Symposium*, pp.85-88, 1999.

[4] S. Matsuyama, Y. Oguchi, H. Endo, D. Sekijima, and Y. Saito, "Three Dimensional Magnetic Fields Data Analysis by the Discrete Wavelets Transform," *Proceeding of the 20th Japan Simulation Society Symposium*, pp.195-198, 1999.

[5] H. Endo, S. Hayano, and Y. Saito, "Faster Animation Image Generation by Wavelets," *Journal of the Visualization Society of Japan*, Vol.20, Suppl.No.1, pp.141-144, 2000.

[6] H. Endo, S. Hayano, M. Fujikura, C. Kaido, and Y. Saito, "Consideration on the Dynamic Domain Images," *The Papers of Technical Meeting on Magnetics, IEE Japan*, MAG-00-257, 2000.

[7] T. Naruta, H. Endo, S. Hayano, and Y. Saito, "A Study of Planar Inductor Design," *The Papers of Technical Meeting on Magnetics, IEE Japan*, MAG-00-265, 2000.

[8] H. Kochi, H. Endo, S. Hayano, and Y. Saito, "Magnetic Sensor Analysis by Finite Elements," *The Papers of Technical Meeting on Magnetics, IEE Japan*, MAG-00-270, 2000.

[9] Y. Senoo, H. Endo, S. Hayano, and Y. Saito, "Wavelet Analysis of the Magnetic Flux Distributions in Magnetic Tilt Sensor," *The Papers of Technical Meeting on Magnetics, IEE Japan*, MAG-00-271, 2000.

[10] T. Naruta, A. Ema, H. Endo, S. Hayano, and Y. Saito, "Proposal of Representation and Evaluation for Magnetic Materials," *The Papers of Technical Meeting on Magnetics, IEE Japan*, MAG-01-62, 2001.

[11] H. Endo, S. Hayano, and Y. Saito, "Consideration on the Electromagnetic Field Visualization Methodologies," *The Papers of Technical Meeting on Magnetics, IEE Japan*, MAG-01-69, 2001.

[12] H. Endo, S. Hayano, Y. Saito, and K. Horii, "Separation of Dynamic and Static Images by Modal-Wavelets," *Journal of the Visualization Society of Japan*, Vol.21, Suppl.No.1, pp.219-222, 2001.

[13] N. Morohoshi, H. Endo, Y. Saito, and K. Horii, "Visualization of Inward Movement while Reading a Novel –Analysis by Using Wavelets–," *Journal of the Visualization Society of Japan*, Vol.21, Suppl.No.1, pp.235-238, 2001.

[14] T. Naruta, H. Endo, S. Hayano, and Y. Saito, "Magnetic Field Distribution by Wavelets," *Journal of the Visualization Society of Japan*, Vol. 21, Suppl.No.1, pp.371-374, 2001.

[15] H. Endo and Y. Saito, "Evaluation of Non-linearity from Visualized Information," *Mechanical Engineering Congress, Japan (MECJ-01)*, W12-(6), 2001.

[16] H. Endo and Y. Saito, "Dynamics Extraction by Wavelet Multi-resolution Analysis," *Mechanical Engineering Congress, Japan (MECJ-01)*, W12-(7), 2001.

[17] H. Watanabe, H. Endo, S. Hayano, and Y. Saito, "Float Type Tilt Angle Sensor Using Magnetic Fluid," *The Papers of Technical Meeting on Magnetics, IEE Japan*, MAG-01-216, 2001.

[18] T. Naruta, H. Endo, S. Hayano, and Y. Saito, "Consideration of Parameter Measurements for Chua Type Magnetization Model," *The Papers of Technical Meeting on Magnetics, IEE Japan*, MAG-01-227, 2001.

[19] H. Endo and Y. Saito, "Methods of Electromagnetic Field Analysis and Aided Technologies for Medical Treatments," *The Papers of Technical Meeting on Magnetics, IEE Japan*, MAG-01-260, 2001.

[20] K. Makino, N. Morohoshi, T. Sato, H. Endo, Y. Saito, and K. Horii, "Implicit Knowledge Visualization in Picture Books –Approach to Hyakuman-kai Ikita Neko–," *Proceeding of the 11th MAGDA Conference in Tokyo*, pp.283-287, 2002.

[21] N. Morohoshi, H. Endo, Y. Saito, and K. Horii, "Visualization of Reader-Story Fusion World in Reading –Writing-Style Peculiarity Extraction in Long and Short Stories–," *Proceeding of the 11th MAGDA Conference in Tokyo*, pp.288-293, 2002.

[22] N. Morohoshi, H. Endo, Y. Saito, and K.Horii, "Visualization to Characters' Appearance Pattern by Wavelet Analysis," *Journal of the Visualization Society of Japan*, Vol.22, Suppl.No.1, pp.69-72, 2002.

[23] M.Katsumata, H. Endo, S. Hayano, Y. Saito, and K.Horii, "Ferromagnetic Material Cognition by Smart Visualized Information Processing," *Journal of the Visualization Society of Japan*, Vol.22, Suppl.No.1, pp.77-80, 2002.

[24] Y. Okubo, H. Endo, S. Hayano, Y. Saito, and K.Horii, "Magnetization Characteristics Evaluation by Means of Dynamic Image Cognition," *Journal of the Visualization Society of Japan*, Vol.22, Suppl.No.1, pp.247-250, 2002.

[25] H. Endo, S. Hayano, and Y. Saito, "Consideration on Electric Circuit Analysis Including Saturable Inductance," *The Papers of Technical Meeting on Magnetics, IEE Japan*, MAG-02-139, 2002.

[26] H. Endo, H. Mogi, M. Fujikura. C. Kaido, S. Hayano, and Y. Saito, "Visualized Image Based Magnetization Characteristic Modeling and Its Approach," *The Paper of The 129th Technical Meeting, Magnetic Society of Japan*, pp.31-37, 2003.

[27] Y. Nagaya, H. Endo, T. Takagi, T. Uchimoto, and H. Huang, "Visualization of Multiple Cracks with ECT Imaging Identification," *Journal of the Visualization Society of Japan*, Vol.23, Suppl.No.1, pp.99-102, 2003.

[28] Y. Okubo, H. Endo, S. Hayano, Y. Saito, and K.Horii, "Visualization of Magnetic Domain Dynamics of Ferromagnetic Silicon Steel Simulated by Ball Permanent Magnets," *Journal of the Visualization Society of Japan*, Vol.23, Suppl.No.1, pp.263-266, 2003.

[29] T. Takagi, T. Uchimoto, Y. Nagaya, H. Huang, and H. Endo, "Design of Eddy Current Camera for Non-destructive Testing," *Proceeding of SICE Annual Conference 2003 (in English), Fukui, Japan*, TAII-1-4, 2003.

[30] Y. Nagaya, H. Endo, H. Huang, T. Uchimoto, T. Takagi, A. Nishimizu, M. Koike, and T. Matsui, "Research on Adaptive ECT Camera for Structures (1) –Basic Characteristics of a Multi-coil ECT Probe–," *Autumn Annual Meeting of Atomic Energy Society of Japan*, p.236, 2003.

[31] H. Huang, H. Endo, T. Uchimoto, T. Takagi, A. Nishimizu, M. Koike, and T. Matsui, "Eddy Current Nondestructive Evaluation of Deep Cracks for Thick Structures," *Autumn Annual Meeting of Atomic Energy Society of Japan*, p.237, 2003.

[32] H. Endo, T. Takagi, S. Hayano, and Y. Saito, "A Representation of Magnetic Motive Force in Terms of Magnetic Currents and Its Validity," *The Papers of Technical Meeting on Magnetics, IEE Japan*, MAG-03-122, 2003.

[33] H. Endo, H. Huang, T. Uchimoto, T. Takagi, A. Nishimizu, M. Koike, and T. Matsui, "ECT-Based Quantitative Evaluation for Deep Cracks in Thick Materials," *Autumn Annual Meeting of the Japan Society of Non-Destructive Inspection*, pp.75-77, 2003.

[34] T. Takagi, H. Endo, and T. Uchimoto, "New Applications and Developments in Non-Destructive Evaluation Methods using Eddy Currents," *Proceeding of Symposium on Diagnosis of Structural Integrity by Surface NDT Methods*, pp.1-6, 2004.

A.4 Patents

[1] Y. Saito, H. Endo, and K. Horii, Information Analysis Method, Japanese Patent No. 2001-290795.

[2] C. Kaido, M. Fujikura, Y. Saito, and H. Endo An estimation method of the magnetization characteristic distribution and an evaluation method of the material quality on magnetic materials, Japanese Patent No. 2002-156362.

[3] A. Nishimizu, T. Matsui, M. Koike, T. Takagi, T. Uchimoto, H. Huang, and H. Endo, Eddy Current Testing Probe, Japanese Patent Application No. 2003-201741.

A.5 Theses

Graduation Thesis

H. Endo, "Analysis of Magnetic Field Distribution on the Planar Type Transformers," *HOSEI University (in Japanese)*, 1999.

Master's Thesis

H. Endo, "Research on Image Analysis Methodologies for Visualized Electromagnetic Fields," *HOSEI University (in Japanese)*, 2001.

A.6 Others

Awards

[1] The best presentation award, The First Japanese-Australian Joint Seminar, Adelaide, Australia, March 2000.

[2] Prize of Rizing, "ECT-Based Quantitative Evaluation for Deep Cracks in Thick Materials," *Autumn Annual Meeting of the Japan Society of Non-Destructive Inspection (in Japanese)*, November 2003.

Feature Article and Topic

[1] H. Endo and K. Horii, "An Challenge to Fusion Academic Area Using Wavelet Transform –Literary Style and Eddy Flow Structure–," *Journal of the Visualization Society of Japan (in Japanese)*, Vol. 21, No. 1, pp. 159-163, 2001.

[2] H. Endo and Y. Saito, "Methodologies for Electromagnetic Field Analysis Using Visualized Field Images," *Journal of the Magnetic Society of Japan (in Japanese)*, Vol.28, No. 1, pp.15-21, 2004.

Technical Project Reports

[1] T. Matsui, M. Koike, A. Nishimizu, T. Takagi, T. Uchimoto, H. Huang, H. Endo, M. Hashimoto, K. Fukuoka, and F. Kojima, *Report on Practical Development of Electromagnetic Induction Nondestructive Inspection System for Structures, 2002*, The Public Subscription Project of Practical and Innovative Nuclear Power Development Sponsored by the Institute of Advanced Energy (in Japanese), 2003.

[2] T. Matsui, M. Koike, A. Nishimizu, T. Takagi, T. Uchimoto, H. Endo, M. Hashimoto, K. Fukuoka, and F. Kojima, *Report on Practical Development of Electromagnetic Induction Nondestructive Inspection System for Structures, 2003*, The Public Subscription Project of Practical and Innovative Nuclear Power Development Sponsored by the Institute of Advanced Energy (in Japanese), 2004.